Vaasan yliopisto
UNIVERSITY OF VAASA

SVETLANA MARMUTOVA

Performance of a Savonius wind turbine in urban sites using CFD analysis

ACTA WASAENSIA 349

ELECTRICAL ENGINEERING 4

Reviewers

Professor Ron Zevenhoven
Åbo Akademi
Thermal and Flow Engineering
Biskopsgatan 8
FI-20500 Åbo
Finland

Dr. Kari Alanne
Aalto University
School of Engineering
PO Box 14100
FI-00076 AALTO
Finland

Julkaisija	**Julkaisupäivämäärä**	
Vaasan yliopisto	Toukokuu 2016	
Tekijä(t) Svetlana Marmutova	**Julkaisun tyyppi** Väitöskirja	
	Julkaisusarjan nimi, osan numero Acta Wasaensia, 349	
Yhteystiedot Vaasan yliopisto Teknillinen tiedekunta Energiatekniikka PL 700 FI-65101 VAASA	**ISBN** 978-952-476-674-6 (painettu) 978-952-476-675-3 (verkkojulkaisu)	
	ISSN 0355-2667 (Acta Wasaensia 349, painettu) 2323-9123 (Acta Wasaensia 349, verkkojulkaisu) 1799-6961 (Acta Wasaensia. Sähkötekniikka 4, painettu) 2343-0532 (Acta Wasaensia. Sähkötekniikka 4, verkkoaineisto)	
	Sivumäärä 159	**Kieli** englanti

Julkaisun nimike

Savonius-tuulivoimalan suorituskyky kaupunkialueilla virtauslaskennan avulla

Tiivistelmä

Rakennettaessa tuulivoimaloita kaupunkimaiseen ympäristöön tulee huomioida useita erityisiä näkökohtia, kuten tuulen ominaisuuksien vaikutus energiantuottoon, tuulen puuskaisuus ja tuulivoimalan vaikutus tutkien toimintaan. Tässä tutkimuksessa käsitellään Savonius-tuuliturbiinia stabiileissa ja epästabiileissa tuuliolosuhteissa sekä erityisesti keinoja roottorin aerodynaamisen suorituskyvyn nostamiseksi numeerisen virtauslaskennan (CFD) avulla. Savonius-roottorin malli rakennettiin simulointiohjelmilla Ansys Fluent® 15.0 ja Comsol Multiphysics® 4.3a.

Ansys-ohjelmaan rakennetun Savonius-roottorin 2D-malli, jossa turbulenssi tehtiin k-ω SST -mallilla, varmennettiin käyttämällä aiemmin julkaistua mittausdataa. Työssä ehdotetulla uudella roottorin lavan muotoilulla saavutettiin laskennassa laajalla kärkinopeussuhteen alueella jopa 2 prosenttiyksikköä aiempaa parempi tehokerroin, mikä kuvastaa nostevoiman kasvamista.

Tutkittaessa Savonius-roottorin toimintaa Ansys-mallilla erilaisissa tuuliolosuhteissa havaittiin, että roottorin suorituskyky on herkkä pyörteisyyden taajuudelle; suuremmalla arvolla vaste oli kvasi-staattisen tilan kaltainen.

Tilastollisen menetelmän onnistunut soveltaminen riippuu kyseisestä tuulidatasta, tuulen nopeuden nopeusjakaumasta tai tuulen tehojakautumasta.

Asiasanat

Savonius tuulivoimala, CFD, tehokerroin, puuskainen tuuli

Publisher	**Date of publication**	
Vaasan yliopisto	May 2016	
Author(s) Svetlana Marmutova	**Type of publication** Doctoral thesis	
	Name and number of series Acta Wasaensia, 349	
Contact information University of Vaasa Faculty of Technology Energy Technology P.O. Box 700 FI-65101 Vaasa Finland	**ISBN** 978-952-476-674-6 (print) 978-952-476-675-3 (online)	
	ISSN 0355-2667 (Acta Wasaensia 349, print) 2323-9123 (Acta Wasaensia 349, online) 1799-6961 (Acta Wasaensia. Electrical Engineering 4, print) 2343-0532 (Acta Wasaensia. Electrical Engineering 4, online)	
	Number of pages 159	**Language** English

Title of publication
Performance of a Savonius wind turbine in urban sites using CFD analysis

Abstract
The installation of wind turbines in urban sites requires considering among other issues the following topics: wind characteristics affecting energy generation, gusty nature of the wind and the interaction of a turbine with radar. In this thesis the performance of a Savonius wind turbine under steady and unsteady wind conditions and the ways to improve its aerodynamic efficiency are studied using computational fluid dynamics (CFD) analysis. As the numerical tools Ansys Fluent®15.0 and Comsol Multiphysics®4.3a were used.
The 2D model of Savonius rotor in Ansys Fluent® with the k-ω SST turbulence model was verified and validated using published experimental data. A suggested modification of the rotor blade shape results in the improvement of the power coefficient up to a 2% in the wide range of the tip speed ratios by increasing the lift force.
The operation of the Savonius rotor under unsteady wind conditions was studied using the Ansys model. The performance of the Savonius rotor is sensitive to the level of gustiness: it was found that with the higher level of gustiness the rotor response is similar to the rotor in quasi-steady state.
The accuracy of a statistical method may depend on the wind characteristic to obtain: the wind speed probability density or the wind power density.

Keywords
Savonius wind turbine, CFD, power coefficient, gusty wind, urban site

ACKNOWLEDGEMENT

"…we don't need no thought control" Pink Floyd. Another brick in the wall.

We need education. However, with all the knowledge that we have at that point with our classic model of education students should spend few decades at school. Instead, I do believe that the educational institutions have to teach students how to learn: how to find reliable material, how to build logistic schemes of question-method-result, how to question and doubt existing approaches and how to ask questions. Only an active participation in the education process, but not a passive listening, can result in an open minded spirit ready to never stop exploring.

To big extent the work on this project reinforced my confidence in this concept. I am grateful for all colleagues and institutions which make this project possible. I would like to thank my supervisors professor Timo Vekara and Dr. Vladimir Bochko for their encouraging attitude and work in guiding this thesis. I am thankful for the Academy of Finland, Doctoral program in Energy Efficiency and Systems and University of Vaasa for academic and financial support. Professor Ron Zevenhoven from Åbo Academy and D.Sc. Kari Alanne from Aalto University being reviewers of the dissertation made me take a look on my dissertation from new angles through provided constructive critique. We have allways lively and useful discussions with my department coallegues Dr. Bernd Pape and Lic.Tech Lauri Kumpulainen.

I am lucky that my best friends are my colleagues as well: we can support and inspire each other as in our research as in life. Soon Doctors of Science: Manuel Garcia Perez, Ekaterina Sermyagina, Ekaterina Komova, you set top standards in all aspects of life for me to achieve. I am thankfull also to trance music and active sports: the only way to tune a balanced mood.

Neither I, as I am, nor this research would be possible without my family. My parents are rather different, but together they make a balanced unit. They teach me to keep fighting, to dream, to be active, to keep a fire of curiosity in my soul so that this fire can light up a dark path through life.

Vaasa. Spring 2016

Contents

Figures

Tables

Abbreviations

CFD	Computational fluid dynamics
CFL	Courant-Friedrichs-Law
CSC	Tieteen Tietotekniikan Keskus
DNS	Direct numerical simulation
EU	European Union
GCI	Grid convergence index
GPS	Global positioning system
GUI	Graphic User Interface
HAWT	Horizontal axis wind turbine
LES	Large eddy simulation
LRN	Low Reynolds number model
MM	Moment method
MMA	Approximated moment method
MMLM	Modified maximum likelihood method
PC	Personal computer
PDE	Partial differential equation
PDM	Power density method
PEC	Perfect electric conductor
PML	Perfectly matched layer
RANS	Reynolds-averaged Navier-Stokes
RCS	Radar cross section
Re	Reynolds number
RMS	Root mean square
SST	Shear stress transport model
TSR	Tip speed ratio
TUI	Text User Interface
UDF	User defined function
VAWT	Vertical axis wind turbine

Nomenclature

Greek letters

Γ	gamma function
δy	distance from the wall to the centroid of the first mesh cell (m)
ε	turbulent dissipation rate ($m^2 \cdot s^{-3}$)
η, τ	length and time scale of smallest turbulent eddies (m), (s)
θ	rotor angle of rotation (deg)
κ	von Karman constant
λ	tip speed ratio
λ	second viscosity coefficient ($kg \cdot m^{-1} \cdot s^{-1}$)
μ	dynamic viscosity ($kg \cdot m^{-1} \cdot s^{-1}$)
μ_T	turbulent viscosity ($kg \cdot m^{-1} \cdot s^{-1}$)
ν_T	kinematic viscosity ($m^2 \cdot s^{-1}$)
ρ	air density ($kg \cdot m^{-3}$)
σ	standard deviation of the wind speed (m/s)
σ_{ii}	normal stresses ($kg \cdot m^{-1} \cdot s^{-2}$) i=x,y,z
τ_{ij}	tangential stresses ($kg \cdot m^{-1} \cdot s^{-2}$) i,j=x,y,z
τ_{ii}	normal viscous stress components ($kg \cdot m^{-1} \cdot s^{-2}$) i=x,y,z
ω	rotor rotating frequency ($rad \cdot s^{-1}$)

Roman letters

A	projected frontal area of the rotor (m^2)
a_x	acceleration along x coordinate direction ($m \cdot s^{-2}$)
C_m	moment coefficient
C_p	power coefficient
C_μ	turbulent constant
c	scale parameters of Weibull function (m/s)
D	rotor diameter (m)
d	blade diameter (m)
e	overlap distance (m)
e/d	overlap ratio
F_x	force along x coordinate direction (N)
k	turbulent kinetic energy per unit mass ($m^2 \cdot s^{-2}$)
k	shape parameters of Weibull function
k_p	turbulent kinetic energy per unit mass in the cell centre ($m^2 \cdot s^{-2}$)
L,T	length and time scale of larger turbulence eddies (m), (s)
L	rotor height (m)

m	fluid mass (kg)
p	pressure (Pa)
P	wind power density ($W \cdot m^{-2}$)
q	length of the gap flow guide (m)
r	mesh refinement ratio
T	mechanical torque (N·m)
u	velocity component, x coordinate direction, (m/s)
$\overline{u}$	time averaged velocity (m/s)
u'	velocity fluctuations (m/s)
U_p	velocity in the centre of the cell adjacent to the wall (m/s)
V	free stream velocity m/s
v	velocity component, y coordinate direction (m/s)
v_i	the wind speed value central to the bin i (m/s)
w	velocity component, z coordinate direction (m/s)
$\Delta x, \Delta y, \Delta z$	increments along x,y and z coordinate directions (m)
Δx_1	cell size of the fine mesh (m)
Δx_2	cell size of the coarse mesh (m)
y^+	dimensionless wall distance
y_p	distance between the wall and the cell centre (m)

1 INTRODUCTION

This chapter contains the background and motivation of the study, followed by the research questions. The organization of the study is also described..

1.1 Wind energy utilization in urban sites using VAWTs

Rising concerns about global climate change, planet pollution and increasing use of energy have renewed the interest in developing and wider utilization of renewable energy sources. Wind, solar, hydro and bioenergy sources are in focus of attention.

Wind energy systems have continuously been developed since 1970's. A recent trend in energy system development is decentralization of power generation systems. The opportunity for individuals or organizations to generate electricity locally decreases losses and part of the electricity price caused by the long distance power transmission. The decentralized energy system is expected to secure continuous power delivery to the consumers. In addition, the distributed energy systems meet the challenges of sustainable development through flexibility, locality and networking. Various energy conversion technologies can be utilized providing scalability and flexibility to the distributed energy systems. (Alanne et al. 2006) The utilization of wind energy in urban areas in the frame of energy systems decentralization also provides a solution for these challenges.

Urban population makes up more than 70% of the total population in the European Union (EU). According to the European Commission inhabitants and industries in urban areas consume around 70% of the total produced heat and power and release 75% of the EU's greenhouse gas emissions. (Callatay et al. 2011) As urbanization is expected to increase in coming decades there is a need to proceed towards the development of more economically viable and environmentally sustainable solutions of power generation in urban areas.

A number of challenges arise for the integration of wind energy systems in urban environment. Urban wind conditions are characterized by high level of wind speed variability and decreased energy content in comparison to rural or offshore sites. The turbulence level of the wind in urban areas tends to increase due to the presence of buildings and heat. Furthermore, the direction of the flow changes from horizontal to slightly upwards on the roof of the buildings. (McIntosh 2009) A number of conditions need to be met if a wind turbine is planned to be operating in the city: as low as specified noise level, social acceptability and

aesthetic view, integration into architectural systems and efficient use of the local wind resources.

The potential sites for vertical axis wind turbine (VAWT) installations in urban areas could be

(i) Roofs of buildings,

(ii) Masts and

(iii)Wind tunnels created between buildings and in traffic tunnels.

Wind turbines can be classified by the way they extract energy from the wind flow: using purely drag, lift forces or both. The horizontal axis wind turbine (HAWT) is purely lift type. Due to the special shape of the blade the pressure distribution around the blade generates the lift force along the blade length. This type of rotor is called the propeller type. Lift-type devices offer the most efficient way to convert wind energy into electrical or mechanical energy. (Burton et al. 2002: 41–51)

The wind profile in urban areas is characterised by lower mean wind speed and larger fluctuations in both direction and magnitude in comparison to the rural areas. (McIntosh 2009) The HAWT design is not preferable for operation in urban areas, since they demand a control system installation to follow these wind speed and direction changes. Meanwhile, the VAWTs are less dependent on the changes in wind direction. Therefore, they are assumed to fit better in the built environment.

VAWTs may have straight or curved blades, their operation bases on both drag and lift forces. They can capture wind from any direction without using the yaw drive system required by the HAWTs. Figure 1 shows examples of both turbine types. The VAWTs and Savonius wind turbine in particular are agnostic to changes in wind directions as it is illustrated schematically in Figure 1.

The most common among known VAWTs are Savonius and Darrieus turbines. The installation of VAWTs on the roofs of tall buildings is expected to mitigate the low energy yields observed for urban turbines (McIntosh 2009). Studies of multiple turbines operation indicate that the blockage effect created by the turbines, similar to the wind tunnel blockage effect, can have an advantageous influence on the overall turbine performance (Sun et al. 2012).

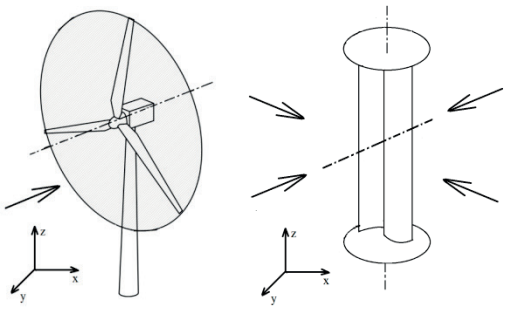

(a) (b)

Figure 1. Schematic illustration of the advantage of the VAWT design (b) over the HAWT design (a) in coping with varying wind directions.

VAWTs found their applicability in urban areas due to their ability to operate under gusty wind conditions in terms of both wind speed and direction variability. A Savonius wind turbine, being a vertical axis wind turbine, possesses a number of advantages, such as:

(i) Nearly independent of the wind direction and thus no yaw mechanisms are required,

(ii) Ability to operate with the wind speeds lower than are needed for HAWTs,

(iii) Cut-in wind speed down to 2 m/s, (Windside 2015, Brännbacka 2015)

(iv) Ability to operate in harsh environmental conditions,

(v) Simplified maintenance management because the generator is located on ground level, and

(vi) Design of the blades makes them easier to fabricate in comparison to HAWTs.

1.2 Implementation of wind turbines in urban areas

In general, the installation of any wind turbine includes a number of steps to be taken and conditions to be met. The European Wind Energy Association (EWEA) published a guidance on the development of wind energy systems. (EWEA 2015) Each project of such a system must include the three main elements:

(i) Technical and economic issues,

(ii) Environmental consideration and

(iii) Dialogue and consultation with local inhabitants and planning authorities.

In this section some of these issues are briefly discussed.

Among the technical issues are the selection of a wind turbine, the availability of infrastructure at the construction place and electrical connection. The economic feasibility contains the income from the forecasted generated power by the power plant, other valuable benefits and subsidies, if such are available, and the expenses on the construction and operation and maintenance. The initial site selection must consider a proper estimation of the wind power potential at the particular site. Data necessary for such a calculation is obtained from the actual wind speed measurements and Wind Atlas if available.

The analysis of the environmental impact of the wind turbine is known to be an essential and time-consuming process. Among the main issues are the following.

(i) The physical characteristics of the wind turbines and their land-use requirements must be described. However, in case of VAWTs, and Savonius turbines in particular, in urban areas they can be installed on the roofs of the buildings, or even in between densely located constructions in order to take advantage on the wind acceleration.

(ii) An impact of the wind turbine on local fauna and flora is to be considered. A Savonius wind turbine is a low-speed machine with the tip speed ratio, which is the ratio of the blade tip speed to the incoming flow velocity around the tip, TSR, within the range of 0.5–2. This means that any risks for birds are hardly relevant. If the turbine is installed on a roof no risks from vibration for animals in the ground are expected.

(iii) One of the important and certainly the most open to subjective judgement factors are visual and landscape assessment. This includes social acceptability and medical harm caused by the operation of the wind farm. As a rule, zones of visual influence are to be determined to indicate from where the wind farm is visible. To speak about the psychological effects of a wind turbine the blades have to be considered: in some cases the shadow of the moving blades and flicking of the warning lights may have undesirable psychological effects for people.

(iv) The noise from the operating wind turbine is included in the list of irritating effects as well. However, a Savonius turbine is practically a noiseless machine. (Windside 2015)

(v) The potential interference of the wind turbine structure in the proximity to airports or military training areas with radars needs to be considered carefully. In this work the radar cross section (RCS) of a Savonius turbine is calculated using a simulation approach.

In this research the discussion of these aspects of wind energy system in urban areas focuses on the Savonius wind turbine interference with radar, modelling of the response of Savonius wind turbine under unsteady wind conditions and obtaining of the characteristics of the wind using the measurements of 10 minutes averaged wind speed.

The unsteady wind conditions are applied in the two-dimensional numerical model by Ansys Fluent with an incoming velocity modelled as a sine function and two sets of gust reduced frequency values. The power coefficient as a function of a tip speed ratio of the Savonius wind turbine is then obtained and analysed.

It is shown how the wind speed probability density and wind power density are obtained using the wind speed measurements averaged over 10 minutes. The wind speed is characterised usually with a Weibull distribution (Celik 2003). Several numerical methods can be applied to the initial data to determine the coefficients of the Weibull function at any particular site. The obtained Weibull function allows for calculation of the wind power density and the annual wind power density. In this investigation different approaches are analysed as to how to choose a proper method to estimate each of wind speed characteristics. The wind speed frequency and wind power density are evaluated and analysed based on the data of five years of measurements at the University of Vaasa, Finland. The particular site is chosen due to the available data of measurements.

So, the **first two research questions** of particular interest arose: *How to obtain the wind speed probability density and the wind power density using the measurements of 10 minutes averaged wind speed? How to estimate the RCS of a Savonius wind turbine and how to model the response of a Savonius wind turbine under unsteady wind conditions using CFD analysis?*

1.3 Aerodynamic efficiency of wind turbines and Savonius turbine in particular

A wind turbine is a device for extracting kinetic energy from an air flow. Part of the kinetic energy of the air flow passing through the swept area of the rotor is transformed into the kinetic energy of the rotor rotation. The power coefficient of a wind turbine is the ratio of the extracted power from the air by the rotor, to the total kinetic power available in the air in the absence of the rotor. (Burton et.al. 2001)

The actuator disc theory for the estimation of the rotor aerodynamic efficiency examines schematically the flow of air through the rotor disc of a horizontal axis wind turbine. It assumes that the affected air stays separated from the air which does not pass through the rotor swept area and therefore it does not slow down. Hence, the boundary surface can be depicted which contains the affected air mass and can be developed upstream and downstream. The cross section of the designed stream-tube is expanded after the rotor disc, since the speed of the flow decreases and the air can be considered uncompressible. Four regions are distinguished: far upstream and downstream and in front and behind the rotor disc. Corresponding velocity and pressure values are defined in these regions for further calculations. (Burton et al. 2002: 41–51) This model, however, is not applicable to a Savonius wind turbine because the operating principles of the turbines differ.

Aerodynamic efficiency of a Savonius wind turbine

It is accepted that each blade of the horizontal axis wind turbine undergoes the same changes in the pressure level along the surface (in front and behind the rotor disc). They are symmetrical from the incoming flow direction and equally contribute to the total torque of the rotor. On the other hand, the blades of a Savonius turbine have an opposite contribution to the total torque: the advancing blade contributes with positive torque, while the returning blade contributes to the negative component of the total torque. Hence, it is not accurate to distinguish pressure levels only in front and behind the rotor disc, when a Savonius turbine is considered. Instead, the pressure levels for each blade must be thus considered separately. The total power extracted by the rotor is represented as the difference of torque values from the advancing and returning blades. Therefore, it is expected that the Betz limit, which states that the maximum power coefficient theoretically achievable by a horizontal axis wind turbine is 0.593, is not directly applicable to a Savonius rotor. It was argued by Savonius, that the Betz limit for the “vertical airwheel” is bounded by 0.2, while

Savonius claimed to achieve the power coefficient for an S-shaped Savonius rotor up to 0.3. (Savonius, 1931: 335)

The total pressure levels around both blades of a Savonius turbine must be known to formulate the total power. A mathematical model of the power coefficient of a Savonius rotor is discussed by Paraschivoiu (Paraschivoiu 2009). The formulation of the model takes into account motor and drag half-cycles. The total torque is formulated using the experimentally obtained pressure difference on the advancing and returning blades

(1) $$\Delta p = \Delta p_{driv} - \Delta p_{res} ,$$

Where Δp_{driv} is the pressure difference on the advancing blade and Δp_{res} is pressure difference on the returning blade.

As there is no mathematical model to be used for the pressure differences in Eq. (1), experimental data was used by Paraschivoiu. The pressure gages were installed at seven points along the blade surface. The final experimental graph provides the values of the overall pressure distribution at those seven points as a function of the blade azimuthal angle. The final power coefficient as a function of bucket TSR correlates with the experimental results. The maximum attained power coefficient in this particular model, discussed by Paraschivoiu, equals to 0.17 (Paraschivoiu 2009: 20).

By definition, the maximum achievable value of the power coefficient assumes zero losses by the rotor which is considered to be a perfect power extractor. In order to estimate the maximum theoretical value of the power coefficient of a Savonius rotor, the ratio between the driving and resistant components of the total torque must be known. It is the returning blade which causes the resistant component to the total torque. A purely theoretical model will be rather complicated because the pressure levels around the turbine vary as the rotor rotates. Furthermore, the application of empirical correlations may limit the generalization and universal applicability of the obtained maximum efficiency.

The two-dimensional model of a wind turbine assumes that the change of momentum of the air passing through the area swept by a blade element depends only on the reaction force of this particular element. In other words the interaction between the flows around adjacent elements of the whole turbine is neglected. This is common practice and it is proven to be acceptable assumption. (Burton et al. 2001: 61) The numerical model of a Savonius turbine can be two-dimensional and the total values of the calculated characteristics are obtained by integration over the rotor height. Strictly speaking not only the interaction of the

flows between elements is considered insignificant but the three dimensional nature of the turbulent flow as well. However, this assumption is also accepted. (Burton et al. 2001)

The aerodynamic efficiency of the turbine is described by the power coefficient Cp. With the use of a numerical model a moment coefficient and torque value can be obtained. The torque and moment coefficient values are integrated along the rotor surface.

(2) $$C_p = \frac{T \cdot \omega}{0.5 \cdot \rho \cdot v^3 \cdot A},$$

where T (N·m) is torque, ω (rad/s) is rotating frequency of the rotor, ρ (kg/m^3) is the air density, v (m/s) is incoming wind speed and A (m^2) is the rotor swept area.

The power coefficient of Savonius wind turbines is within the range 0.15–0.3, which is low in comparison to power coefficient values of HAWTs. (Savonius 1931) Over the last few decades researchers have studied the main principles of a Savonius wind turbine operation in order to increase the power coefficient of the turbine.

The main findings by Savonius related to this research are

(i) The Betz limit for VAWTs, which is bounded by 20 %, is claimed to be exceeded by the S-shaped Savonius rotor; (Savonius, 1931: 335)

(ii) A Savonius rotor is capable of following the changes in the speed and direction of the wind without a control system in contrary to HAWTs; (Savonius, 1931: 333–334)

(iii) A space between the blades, which allows air passing towards the returning blade, eliminates the negative pressure on the leeside of the returning blade and as a result the rotating frequency of the rotor increases; (Savonius, 1931: 334) (Savonius, 1925: 10–12)

(iv) At some rotor positions the starting torque can be lower than the moment of resistance of the generator; (Savonius, 1930: 335–336)

(v) A Savonius rotor follows changes in the wind direction quickly. The increased rotating speed is maintained for a considerable time after the wind speed decreases due to the rotor inertia. Thus, the optimum TSR in

natural wind conditions is in the range 0.92–1.0 in contrast to the optimum TSR in a wind tunnel (0.85); (Savonius, 1930: 336)

(vi) The two-bladed rotor is superior to three-bladed and four-bladed rotors, due to the blocking effect by the oncoming blade and less efficient recovery of the negative pressure on the leeside of the returning blade. (Savonius, 1925: 15–16)

In this study a literature review on the performance of Savonius turbine is presented. Also a modification of the rotor is proposed. The modification is done by adding the flow guide in the gap space between the blades.

Furthermore, the discussion reveals the **Third research question:** *How to improve the aerodynamic efficiency of a Savonius wind turbine?*

1.4 Modelling of a Savonius wind turbine

One of the ways to understand and analyse the operating principle of Savonius wind turbine is by the use of computational fluid dynamics (CFD) methods. CFD incorporates three elements: fluid dynamics, mathematics and computing science. Fluid mechanics is basically the study of fluids either at rest (static mode) or in motion (dynamic mode). One of the applications of CFD methods is the modelling of the fluid flow interactions with moving or stationary structures.

In CFD the fluid motion is described by the fundamental mathematical equations in partial differential form. These equivalencies are known as governing equations since they represent the process of interest mathematically. In order to solve these mathematical equations they must be transformed into a system of algebraic equations which are solved iteratively with the specified tolerance value. Figure 2 illustrates the interconnection of the basic approaches to solve problems in fluid dynamics. The interconnections between the fields embody the exchange of data and methods. For example, some CFD methods include model coefficients, obtained experimentally. In turn, the CFD results are taken into account when experimental conditions are defined.

Although the methodologies within the computational codes are well-developed and validated, some aspects of CFD employment have to be known. Since the CFD simulation is a modelling tool the applied assumptions and applicability for the particular physical phenomena must be taken into account. For example, the typical assumption of local equilibrium of the production and dissipation of

turbulence is not applicable under conditions of strong flow separation or adverse pressure gradient.

Each numerical solution should be verified: the discretization, tolerance values, turbulence models and solution stability are essential parameters and have to be reported. Depending on the type of the fluid flow different turbulence models can be used. For instance, the most widely used turbulent model, standard k-ε model, is often a suitable choice to model the non-bounded flows. However, its application to the wall-bounded flows may lead to considerable errors in the simulation results. A proper choice of the turbulence model, spatial and temporal discretization assures accurate results and optimum time needed to perform the simulation process.

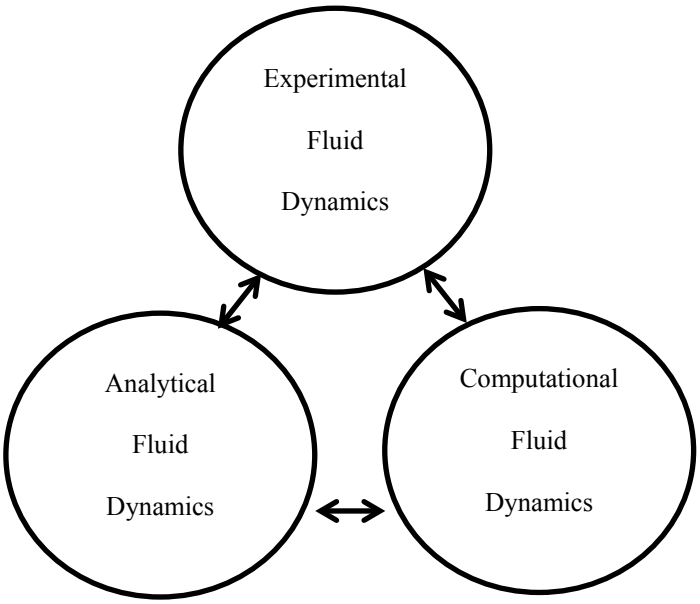

Figure 2. Three principal approaches to solve problems in fluid dynamics and heat transfer.

This leads to the **Fourth research question:** *How to build numerical models and choose their parameters to provide an accurate numerical solution and how to estimate and prevent errors of the numerical solution?*

1.5 Organization of the thesis

This thesis consists of five chapters. In this Chapter the motivation and introduction to the research questions is presented. Chapter 2 discusses the main issues of the CFD methods and numerical solution of the partial differential

equations. The turbulence models relevant to the simulation of Savonius wind turbine are discussed. The models describing a Savonius turbine are created using two commercial simulation programs: Comsol Multiphysics®4.3a and Ansys Fluent®15.0. The verification of the models is presented in the last three chapters: mesh generation and turbulence models are reported.

Chapter 3 contains a literature review of the main aspects of a Savonius rotor configuration which have an impact on the rotor performance. Previously made attempts to improve the aerodynamic efficiency of a Savonius wind turbine both experimentally or with the use of simulation techniques are analysed. Based on this analysis a modification of the turbine blade is proposed to improve the rotor aerodynamic efficiency. The simulation results are then analysed.

The analysis of Savonius wind turbine operation under unsteady wind conditions is presented in Chapter 4. The response of the model to various rates of the inlet wind unsteadiness is obtained.

Chapter 5 deepens the review of the special aspects of Savonius wind turbine installation and use in urban areas. The analysis is done on the performance evaluation of four statistical methods for calculation of the wind characteristics In addition, the wind speed frequency and wind power density are calculated based on measurements of the wind speed made in Vaasa for the five years. The RCS of a Savonius turbine is obtained using the numerical model.

The concluding chapter discusses the obtained results and summarises the answers to the research questions.

1.6 Limitations of the thesis

In this thesis the following limitations are considered:

(i) Only advantageous results are reported, since they contribute to the existing knowledge and development of Savonius turbine;

(ii) The validation and verification of the Ansys Fluent numerical model of an unmodified Savonius rotor has been carried out using the experimental data published by Sandia laboratory. The validation of the numerical model of the proposed modified rotor has not been carried out;

(iii)The created model for time-dependent simulations is two-dimensional, assuming the equal distribution of torque along the rotor height;

(iv) The Reynolds numbers of the Comsol and Ansys Fluent numerical models are 62 000 and from 160 000 to 490 000, respectively;

(v) Comprehensive comparison of a Savonius rotor with HAWTs or other types of VAWTs is not considered, due to significant differences in dimensions, operating principle or lack of the reported parameters of the models;

(vi) Only aerodynamic aspects of Savonius rotor operation are investigated, excluding mechanical issues.

2 COMPUTATIONAL FLUID DYNAMICS IN WIND POWER APPLICATIONS

The various aspects of the numerical models developed and used in the thesis are described in this chapter. The Savonius rotor is modelled using two commercial CFD tools: Comsol Multiphysics®4.3a and Ansys Fluent®15.0 (Workbench). Several differences between these models are addressed in this chapter.

The numerical models used in this study are detailed in terms of the domain size, mesh generation and temporal discretization. Finally, the overview of the uncertainties and errors of the numerical solutions are specified and discussed. The basics of fluid dynamics and governing equations describing them along with the turbulence models, near-wall region modelling and discretization schemes are outlined in the Appendix section.

2.1 Mesh generation

A well-constructed mesh is one of the key model characteristics to avoid instabilities or lack of convergence and to attain more accurate simulation results. This procedure starts with the building of the computational domain.

When a wind turbine is modelled, the computational domain has to be built in accordance with two contradictory conditions: firstly, it has to be large enough so that the domain walls have no influence on the flow field and, secondly, is should be not too large to optimally use computational resources. The wind tunnel blockage effect is usually taken into account when the tunnel experiments are carried out. In CFD model formulation the parametric study is a common way to prove the solution independence on particular parameter.

The common practice to model a Savonius rotor in turbomachinery is to distinguishing two particular sub-domains within the computational domain: a rotating and a stationary sub-domain. It is necessary to create the rotating motion of the rotor and to separate regions with different mesh requirements. In both software packages the stationary sub-domain is formed first by extracting the circle of the future rotating sub-domain from an initial rectangle. Then the rotating sub-domain is added as a separate circle. Figure 3 shows the geometry window of Ansys Fluent®15.0 model. Here the additional lines within the computational domain are created in order to specify the mesh cells distribution

at the mesh generation stage. They are created using the Projection tool and they are involved only at the mesh generation stage.

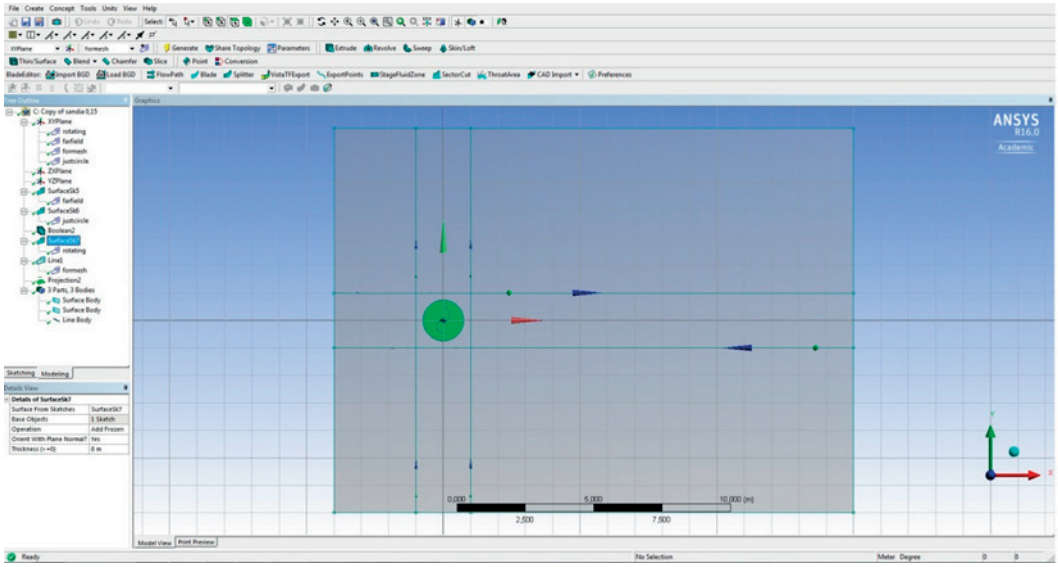

Figure 3. The separation of the stationary and rotating domains at the geometry generation stage in the model of Ansys Fluent.

However, for the flow field the whole computational domain must be united. In Comsol Multiphysics®4.3a these two sub-domains are assembled by creating so-called identity pairs. In the model of Ansys Fluent at the mesh generation stage the separated surfaces are connected with the creation of a so-called “contact region” as shown in Figure 4.

From now on the terms “domain” and “sub-domain” are used for the defined zones within the computational domain with strictly specified borders and conditions, while a “region” is an area within the computational domain without strictly defined borders, which can contain parts of neighboring domains.

The size of a mesh cell depends also on the behaviour of the function derivative in the particularly region where the mesh is to be generated. The complex geometry of a Savonius rotor results in large pressure and velocity gradients around the rotor. In order to resolve these gradients accurately the mesh within the rotating sub-domain must be finer than in the stationary domain for both modelling programs.

The curvature of the tip of the blade also has an influence on the cell size in the vicinity of the blade surface. The larger the mesh cell the sharper the blade angle tip will be. These sharp corners within the meshed domain around the embedded body can cause singularities within the model and lack of convergence, which can

lead to long computation times. The finer the mesh the smoother the surface of the blade is after the meshing is done.

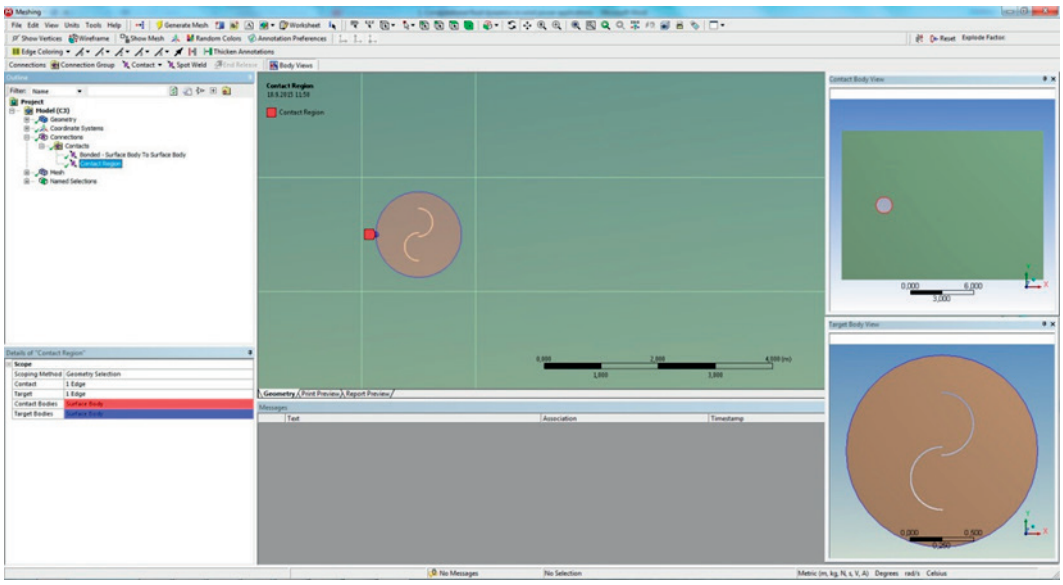

Figure 4. Connection of stationary and rotating domains at the mesh generation stage in the model of Ansys Fluent.

Thus any sharp angle within the geometry must be smoothed. In the model of Ansys Fluent, when a modification of the rotor is implemented during the geometry creation stage, the connection point is smoothed as shown in Figure 5.

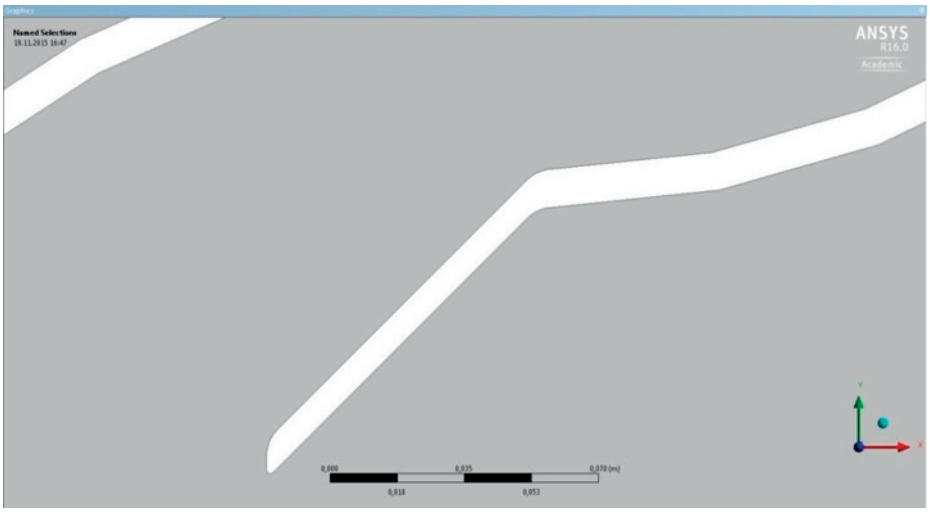

Figure 5. Illustration of the solid connection of the rotor blade and gap flow guide after smoothing.

The mesh characteristics of two models should not be directly compared, since different wall functions are used and discretization methods are applied. Comsol

Multiphysics®4.3a uses wall function and finite element method, while Ansys Fluent®15.0 uses the advantages of LRN wall function and a finite volume method.

One important issue which must be taken into account is the cell growth ratio. The mesh cells size between two neighboring domains cannot vary too drastically. Within the meshing program the mesh growth ratio can be specified, which limits the maximum ratio between the sizes of two adjacent cells. This value can be defined within a particular sub-domain. In the model of Comsol Multiphysics the cell growth ratio is 1.2. In the model of Ansys Fluent the mesh growth ratio within the rotating domain is limited to 1.1.

In Comsol Multiphysics the mesh transition between the rotating and stationary sub-domains is controlled by equating the number of cells on the boundaries of each side of two sub-domains. This means that although the mesh is coarser in the stationary domain in comparison to the rotating domain, the border region is meshed with cells of similar size. Figure 6 shows the details of the transition region between the rotating and stationary sub-domains.

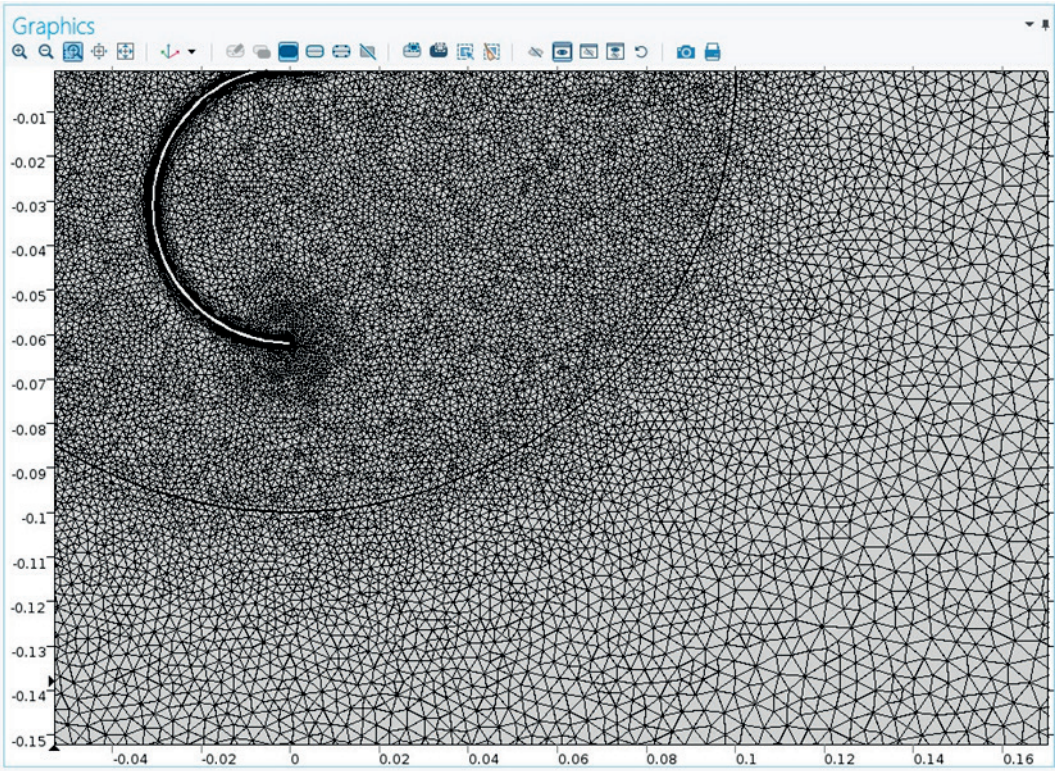

Figure 6. The mesh in the transition region between the rotating and stationary domains in the model of Comsol Multiphysics .

In the model of Ansys Fluent this problem of mesh transition was resolved by specifying the growth ratio, firstly, and secondly, by creating three sub-domains for mesh generation: a rotating sub-domain, a rectangular stationary sub-domain and a sub-domain connecting them. This is particularly helpful because of the different shapes of the rectangular stationary sub-domain and the circular rotating sub-domain. In addition, the outside border line of the rotating domain is connected to the inside border line of the connecting domain in the special edge sizing section. This way, the cell size of the cells in the boundaries of adjacent sub-domains is coherent.

Table 1 contains the details of the generated meshes for the two models. Note that the data on the fine mesh is given for the model of Comsol Multiphysics. More information on the coarse and the finest mesh of the Comsol Multiphysics model is given below in the mesh convergence section.

Table 1. Details of the generated mesh with the models of Comsol Multiphysics and Ansys Fluent.

	Maximum allowed cell size (m)		
Model	**Rectangular stationary domain**	**Stationary connecting domain**	**Rotating domain**
Ansys Fluent	0.05	0.025–0.01	0.02–0.01
Comsol Multiphysics	0.01–0.005		0.004–0.001

The rotating sub-domain in the model of Ansys Fluent is meshed with the quadrilateral elements. This may not be the best choice, because some of the cells close to the rotor turn into paved quadrilaterals – quadrilaterals with a triangular or prismatic shape as in Figure 7. Such transition could lead to additional errors due to unstructured shape of the cells. Still the domain could not be meshed with triangles, since the Mapped mesh tool in Ansys Fluent workbench is not applicable to such a complicated body as inside the rotating sub-domain.

It should be mentioned that a different way of the mesh creation in the stationary sub-domain is used in the model of Ansys Fluent. The rectangular stationary sub-domain was submapped with rectangle elements, maintaining a constant size and arrangement of the cells. The mesh here has a micro-structured topology. This kind of mesh structure is expected to improve convergence and time needed for simulation since the finite volume method is applied. Figure 8 shows a part of the meshed stationary sub-domain and the mesh in the vicinity of the rotating sub-domain.

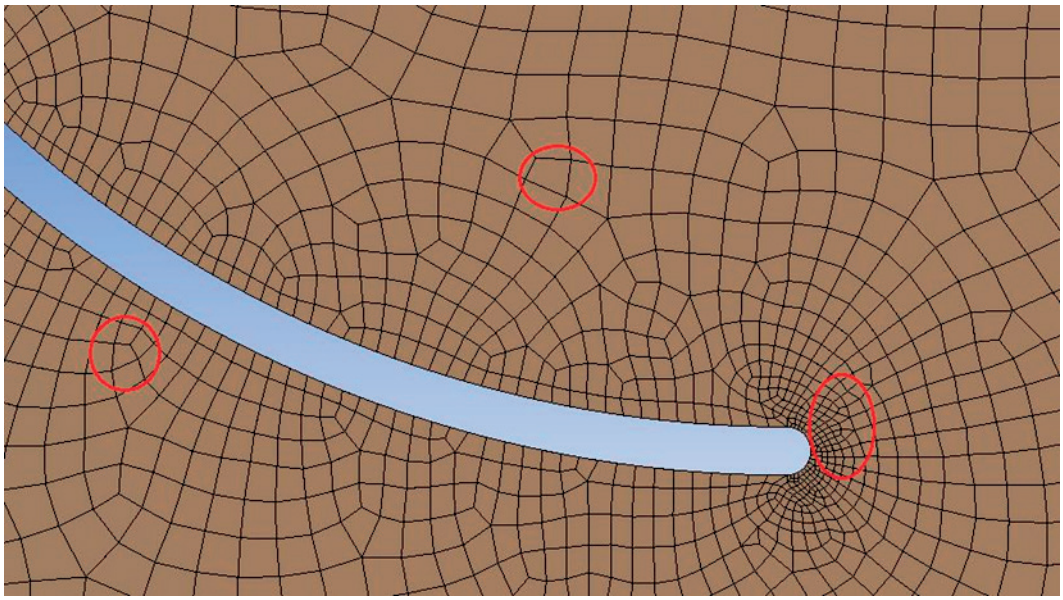

Figure 7. Mesh cells in the rotating domain in the model of Ansys Fluent. Quadrilaterals with the prismatic shape are highlighted.

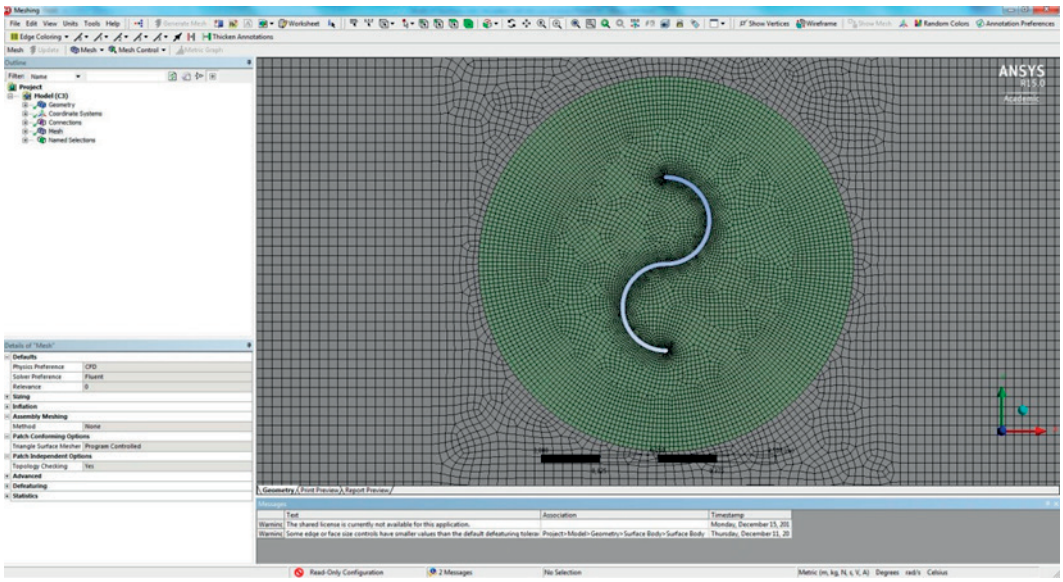

Figure 8. Illustration of the transition of the mesh from the rotating domain to the stationary domain.

2.2 Near-wall region modelling

In the Appendix 1 two main concepts of modelling of the near-wall region were discussed. Table 2 gathers the applied turbulence models and corresponding near-wall treatment models.

Table 2. Details of the turbulence and near-wall models applied at the models of Comsol Multiphysics and Ansys Fluent.

	Turbulence model	**Near-wall modelling**	**y^+**	**Last modelled boundary layer**
Comsol Multiphysics	k-ε	Standard wall function	≥11.06	Logarithmic layer
Ansys Fluent	k-ω SST	LRN	≤1	Viscous sublayer
	Reynolds stress	LRN	≤1	Viscous sublayer

Turbulence models in the Turbomachinery unit in Comsol Multiphysics®4.3a are limited to standard k-ε model with standard wall function. The wall function in Comsol Multiphysics®4.3a locates the centroid of the first mesh cell at the distance y according to the condition y^+=11.06. The dimensionless wall distance y^+ indicates in which boundary layer the cell locates.

In other words, this value of y^+ corresponds to the distance to the wall where the viscous sublayer reaches the logarithmic layer since the sublayer between them is considered negligible. If the value of y^+ is not sustained during the simulation process then the centroid of the first mesh cell locates either in the viscous layer (below 11.06) or in logarithmic layer (above 11.06). (Comsol 2012) Both of these cases conflict with the assumptions of the wall function approximation, which states, that the flow in the viscous sublayer is approximated, but not modelled.

The reported value of y^+ is achieved and controlled using the Boundary layer tool around the blade surface and side walls. This tool uses thin rectangles, which have more stretched side along the surface and more narrow side in the direction normal to the surface. Such an element shape corresponds to the larger velocity profile variations in the direction normal to the wall surface in comparison to the variations in the flow direction.

Within Ansys Fluent®15.0 the mesh could be generated using either Gambit or Workbench software with different mesh generation options and techniques. Despite these differences both programs allow modelling with full range of functions and options. For this model the Workbench is used, since it is included in the licenced program provided by the state-owned Finnish company Tieteen Tietotekniikan Keskus (Centre of Scientific Computing CSC). Within the Workbench the mesh is generated in the Mesh stage and can still be adjusted in the Setup stage.

Since the LRN is used to model the near-wall region it is necessary to make sure that the first mesh cell is located at the proper distance from the blade surface as

stated in Eq. (A1.46). This is done using the Adaption tool and setting up the corresponding Macros. The Adaption tool allows for calculating the y^+ value at each time step and change the mesh at the blade surface to meet the specified condition.

Figure 9 illustrates the way to implement the Adaption tool using the Macros function in Ansys Fluent®15.0.

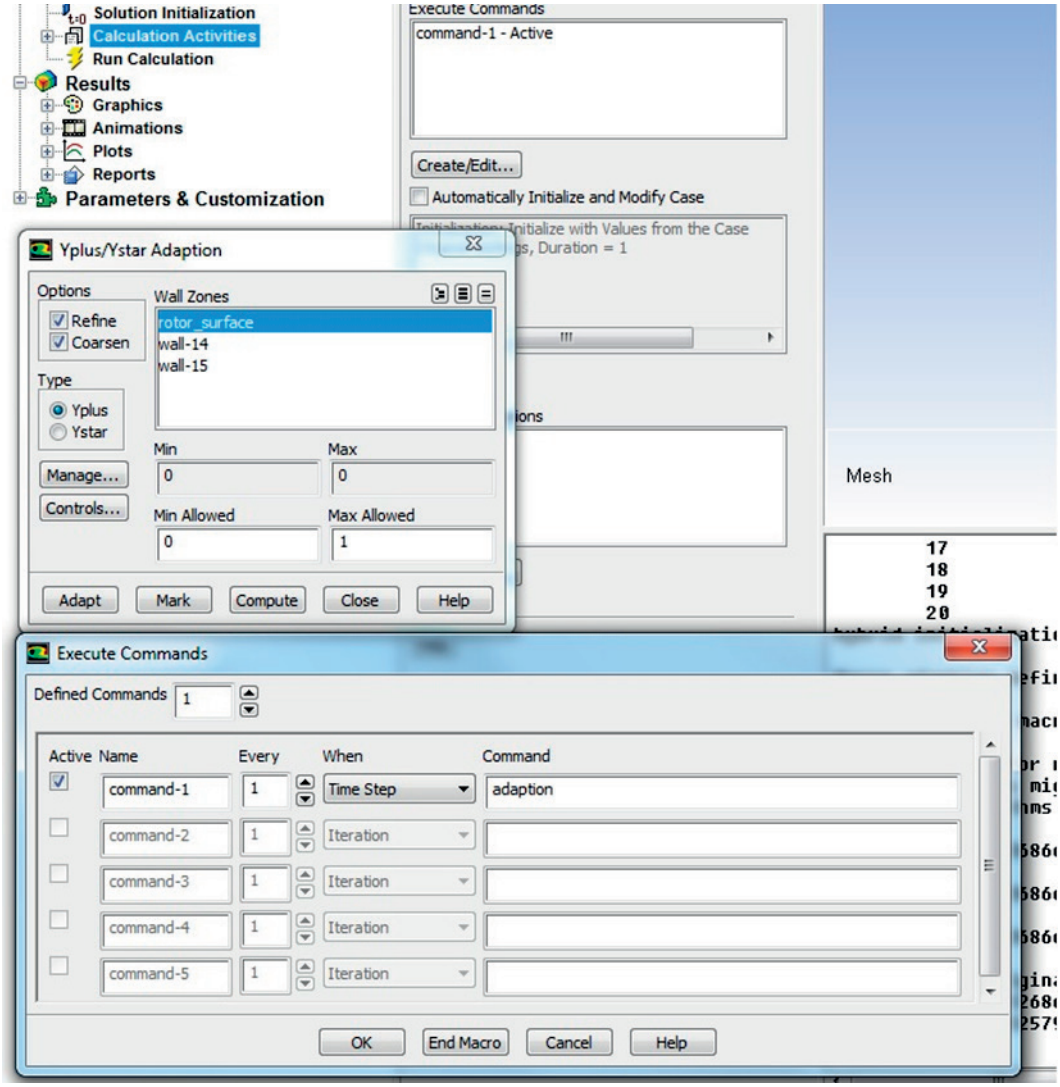

Figure 9. Setting up the mesh Adaption tool and Macros in order to sustain the $y^+ \leq 1$.

An attempt was also made to use the Adaption tool through the Text User Interface (TUI) along with the Graphic User Interface (GUI). One of the reasons was the necessity to use the Ansys Fluent software within the CSC cluster and only TUI is available for such application. However, this attempt was not

successful. It should be noted, that in order to use the Ansys Fluent numerical model in the CSC environment the working .cas file had to be uploaded first and then call this file in the .txt document to start the simulation process. Therefore, the first time steps were simulated on a regular PC until the y^+ value had become stable and no mesh cells were marked for refinement or coarsening. Then the .cas file with obtained proper mesh was saved and uploaded to the users' folders to continue the simulation. Despite of large computational resources and computational capacities, the simulations took a much longer time in comparison to the PC used previously to prepare the .cas file with the proper value. One of the reasons could possibly be the large number of users, performing simulations simultaneously at CSC's computers.

2.3 Mesh convergence

Keeping in mind that the provided CFD solution is not an exact solution but an approximated solution, the process assumes a discretization error. This error is the difference between the exact solution of the PDE and the solution of the discretization equations

(3) $$e_{dis} = C_{m(ex)} - C_{m(dis)}$$

where C_m is the moment coefficient of the rotor blade, (ex) is the exact solution and (dis) is the solution of the discretization equation.

If the discretization error is of order p then the discretization error can be represented as follows:

(4) $$e_{dis} = A(\Delta x)^p + O\left((\Delta x)^{p+1}\right),$$

where Δx is cell size, A is generally unknown constant which depends on the local properties of the solution, properties of the discretization scheme and mesh design. (Zikanov 2010, 285–286)

By this the pure discretization error is separated from the errors resulted from the local properties of the solution, such as: design of the mesh and derivatives' behaviour. So far the conclusion can be that the discretization error reduces by approximately a factor n^p when the mesh is refined with a factor of n. Thus, it is possible to estimate the discretization error by comparing solutions with systematically refined meshes. If two meshes are geometrically similar, use the

same discretization scheme and differ only by the average cell sizes Δx the resulting solutions are related to the exact solution of the PDE as

(5) $$C_{m(ex)} = C_{m(dis)1} + A(\Delta x_1)^p + O\left((\Delta x_1)^{p+1}\right)$$

and

(6) $$C_{m(ex)} = C_{m(dis)2} + A(\Delta x_2)^p + O\left((\Delta x_2)^{p+1}\right).$$

By subtracting and rearranging these two equations it is possible to estimate e_{dis} and $C_{m(dis)}$ for the solution on the first mesh:

(7) $$A = \frac{C_{m(dis)1} - C_{m(dis)2}}{(\Delta x_2)^p - (\Delta x_1)^p} + O(\Delta x_1, \Delta x2),$$

(8) $$\begin{aligned} C_{m(ex)} &= C_{m(dis)1} + \frac{C_{m(dis)1} - C_{m(dis)2}}{(\Delta x_2)^p - (\Delta x_1)^p}(\Delta x_1)^p + O\left((\Delta x_1)^{p+1}, \Delta x_1, \Delta x2\right) \\ &\approx C_{m(dis)1} + \frac{C_{m(dis)1} - C_{m(dis)2}}{(\Delta x_2)^p - (\Delta x_1)^p}(\Delta x_1)^p, \end{aligned}$$

(9) $$\begin{aligned} e_{dis} &= \frac{C_{m(dis)1} - C_{m(dis)2}}{(\Delta x_2)^p - (\Delta x_1)^p}(\Delta x_1)^p + O\left((\Delta x_1)^{p+1}, (\Delta x_2)^{p+1}\right) \\ &\approx \frac{C_{m(dis)1} - C_{m(dis)2}}{(\Delta x_2)^p - (\Delta x_1)^p}(\Delta x_1)^p. \end{aligned}$$

Eqs. (8) and (9) constitute to a method called Richardson extrapolation. This method is used as a rule when a large number of computations has to be done. (Roache 1994) Despite the simplicity of this method difficulties may arise from the necessity to conduct computations on a finer mesh. Meanwhile the first mesh has to be already fine enough to catch all essential physical processes so that the asymptotic formula in Eq. (4) is valid. The refinement ratio $\frac{\Delta x_1}{\Delta x_2}$ has to be at least 1.5, with a preferable value equal to 2 (Zikanov 2010: 286). Among the purposes of application of this method is not only to estimate the discretization error and to correct the final moment coefficient value, but also to define the level of mesh quality when the error becomes smaller than given tolerance. The Richardson extrapolation method was applied when the mesh was analysed in the model of Ansys Fluent. The fine mesh contains 250 000 elements and the coarse mesh 120 000.

In order to achieve mesh convergence a number of models with systematically refined mesh are to be simulated. Then the obtained numerical solutions are to be compared in terms of integrated properties, for example the rotor torque. The solution is grid independent when further mesh refinements do not change the observed properties considerably. That means in practice that, for instance, the rotor torque obtained with systematically refined mesh vary within the specified range.

In the model of Comsol Multiphysics the grid independence was achieved using the grid convergence index (GCI) developed by Roache. This method of mesh quality analysis has been evaluated over several hundred CFD codes. (Roache 1994) The three meshes chosen for this study were refined systematically with the use of the similar cell types.

One of the issues in numerical computations is to decrease discretization errors using still reasonable computational cost. It must be understood that, however infinitely small the mesh cell an error still exists between the achieved asymptotic value and the exact solution.

The k-ε turbulence model with standard wall function is used in the model of Comsol Multiphysics. This implies that the value of the moment coefficient is expected to be less sensitive to the mesh changes than if the LRN turbulence model was applied. However, the limitation of the k-ε model in the simulation of the flows with pressure gradient is still a fair trade-off for the amount of computational resources needed compared to other more complicated turbulence models. (Zhao et al. 2009)

Table 3 contains the parameters of the three meshes used in this model. It should be noted that the minimum value of the mesh cell size is constant for all three cases. This is done in order to avoid sharp corners when the blade curvature is resolved. The size of the representative mesh cell was calculated in the model of Comsol Multiphysics by dividing the total domain area (7.68 m^2) by the number of elements

$$\mathbf{(10)} \qquad h = \left[\frac{1}{N} \sum_{1}^{N} \Delta A_i \right]^{0.5},$$

where h is the representative cell size, ΔA_i is size of the i cell and N is a number of cells in the corresponding domain.

The parameters of the meshes were chosen so that the grid refinement factor r_{ij} is greater or equal to 1.3, as demonstrated in Table 3,

(11) $$r_{ij} = \frac{h_i}{h_j}.$$

Table 3. Details of the three studied meshes in the model of Comsol Multiphysics and the refinement factor. The grid refinement factors r_{32} and r_{21} are equal to 1.3 and 1.4 respectively.

	Mesh quality					
	Coarse		**Fine**		**Very fine**	
Mesh parameters	Rotating domain	Stationary domain	Rotating domain	Stationary domain	Rotating domain	Stationary domain
Max cell size (m)	0.0053	0.013	0.004	0.01	0.003	0.007
Min cell size (m)	0.001	0.006	0.001	0.005	0.001	0.004
Number of cells	26 696	204 432	41 094	334 752	66 766	672 912
Representative cell size (m)	0.00576		0.00452		0.00322	

From this point, the subscript 3 will be used for the coarse mesh, 2 for the fine mesh and 1 for the very fine mesh. The apparent order p of the method was calculated with the use of a set of equations:

(12) $$p = \frac{1}{\ln(r_{21})}\left|\ln\left|\frac{T_3 - T_2}{T_2 - T_1}\right| + q(p)\right|,$$

(13) $$q(p) = \ln\left(\frac{r_{21}^p - s}{r_{32}^p - s}\right)$$

and

(14) $$s = 1 \cdot \operatorname{sign}\left(\frac{T_3 - T_2}{T_2 - T_1}\right),$$

where T_i is rotor torque for i mesh type.

The approximate relative error and extrapolated error within the model are calculated as

(15) $$T_{21}^{ext} = \frac{\left(r_{21}^{p} T_1 - T_2\right)}{\left(r_{21}^{p} - 1\right)},$$

(16) $$e_a^{21} = \left|\frac{T_1 - T_2}{T_1}\right|, e_{ext}^{21} = \left|\frac{T_{ext}^{21} - T_1}{T_{ext}^{21}}\right|$$

and

(17) $$GCI_{21} = \frac{1.25 \cdot e_a^{21}}{r_{21}^{p} - 1}.$$

Results of the calculation procedure are tabulated in the Table 4.

Table 4. Data on the GCIs and the associated parameters for the three analysed meshes in the Model of Comsol Multiphysics.

	Mesh quality		
	Coarse	**Fine**	**Very fine**
h	0.00576	0.00452	0.00322
T	0.23499	0.23352	0.23467
p	0.83*		
T_{ext}^{21}	0.24		
T_{ext}^{32}	0.23		
e_a^{21}(%)	0.49		
e_a^{32}(%)	0.63		
e_{ext}^{21}	0.5		
e_{ext}^{32}	1		
GCI_{21},%	1.9*		
GCI_{32},%	3.2*		

The GCIs of two groups of meshes decreases with the mesh refined: from 3.2 % for the Coarse and the Fine meshes to 1.9 % for the Fine and the Very fine ones. Therefore the approximate numerical solution is approaching asymptotically to the exact solution as the mesh approaches the Very fine mesh.

*This part of the study was presented at the conference ECOS2014 with an error in calculations. Here are corrected values.

Time discretization

A time-dependent model involves not only spatial but also temporal discretization. The solution consists of a number of time steps $t^n=t_o+n\cdot\Delta t$. Where t_o is the initial time point, Δt is the time step and n is a number of time steps. The time step can be constant throughout the simulation, or can vary within a specified range. The second approach, so-called variable time step, was applied in both studied models. It allows for accelerating the computations by adapting the time step duration Δt at each time step t^n. The upper limits are set by requirements of accuracy and numerical stability.

Courant-Friedrichs-Law

One of the necessary, but however not sufficient, conditions which need to be met in order to achieve the stability of the numerical solution is Courant-Friedrichs-Law condition (CFL). The CFL equation establishes a relation between the mesh size and time step within the numerical model. In other words, the CFL certifies that with each next time step the simulated flow process within each mesh cell follows the physical flow process. The upper limit of the time step is related to the cell size and to the incoming wind speed (u)

(18) $$\mathrm{CFL} = u\frac{\Delta t}{\Delta x} \leq 1 .$$

In the model by Comsol Multiphysics the convergence was not achieved with the use of the averaged cell size and the minimum cell size was used further to calculate the time step and achieve the convergence. In that case the CFL condition for averaged cell size is met by default. Resulting upper limit of the time step used in the model by Comsol Multiphysics is $2.5\cdot10^{-4}$ s with the TSR equals 1, which is around 0.5 degree of the rotation with the inlet wind speed equal to 4 m/s. In the model by Comsol Multiphysics the simulations were conducted for one TSR value.

In the model by Ansys Fluent a number of simulations with different TSRs were conducted. For each value of the TSR the time equal to one degree of rotation was calculated. The final upper limit of the time step was chosen as the minimum value between this time for one degree of rotation and the time step specified by the CFL. However, the time of one degree of rotor rotation was chosen as a time step as a rule. The minimum and maximum time step change factors were 0.5 and 1 respectively. The variable time step method is handy and useful for the solver to overcome the initial lack of convergence.

2.4 Numerical solution analysis

When talking about the numerical solution errors, firstly, the terms consistency and stability should be defined. The consistency parameter certifies the transformation of the original PDE into the governing equations through the discretization process. Essentially the consistency aspect is determined by the truncation error. For any numerical method to be consistent, the truncation error must approach a zero. The stability ensures that with any adopted numerical algorithm the simulation process attains the stable condition. This aspect concerns the growth of the errors added at any step during the computations. These errors are caused by the rounding-off at every step of computations due to limited computer memory or poor initial guess. A numerical method is therefore marked as stable if it does not generate more errors with the progress of the simulation process. The stability can be achieved by specifying a proper time step as it was discussed. (Tu et al. 2013)

The imbalances of the discretized equations at the end iteration are monitored and called the residuals of the system of algebraic equations. The simulation process is terminated when the residuals reach the specified tolerance. The process of achieving iterative convergence is illustrated in Figure 10.

However, even convergence of a solution does not necessarily mean that the solution is accurate. The main sources of errors are as follow:

(i) Discretization error,

(ii) Rounding-off error,

(iii) Iteration of convergence error and

(iv) Physical modelling error.

Before these errors are further discussed the errors and uncertainties have to be distinguished. The uncertainty is a potential drawback which arises from the lack of knowledge of the physical process. The error is a recognizable deficiency due to the inaccuracy of the discretization method, approximation character of the turbulent model, computational power limits etc.

Rounding-off error

The rounding-off error is associated with the limited capacity of the particular computer to process a certain value with a finite number of significant digits. The computers with the number of significant digits equal to 7 are commonly referred

to as single-precision, while 15 significant digits are referred to as double-precision. Due to the different scale of the variables within the equation even different sequences of calculations may lead to different solutions. The rounding-off error depends on the number of calculations, the particular rounding-off method and rounding-off type. (Tu et al. 2013)

Iteration or convergence error

The iteration error is the difference between the ideally fully converged solution and a solution that has not achieved the fully converged state, neglecting the errors derived from the spatial and temporal discretization. The reason for these assumptions is that even with an infinitively fine mesh and improper time step the iterative process may not converge. It should be noted that with a large time steps the solver is unable to track the changes in the flow perfectly. If the simulation process is terminated too early an error will arise for the converged flow fields have not been reached yet. The termination can take place due to too high value of the specified tolerance of residuals. The choice of the tolerance value is again a trade-off between the accurate numerical solution and reasonable computational resources involved.

In the model of Comsol Multiphysics the tolerance values are 10^{-4} for the velocity and pressure values and 10^{-5} for the turbulent kinetic energy and dissipation rate values. In the model of Ansys Fluent the tolerance values can be seen in Figure 10, since the achievement of the tolerance value by the residuals means termination of the iterative process.

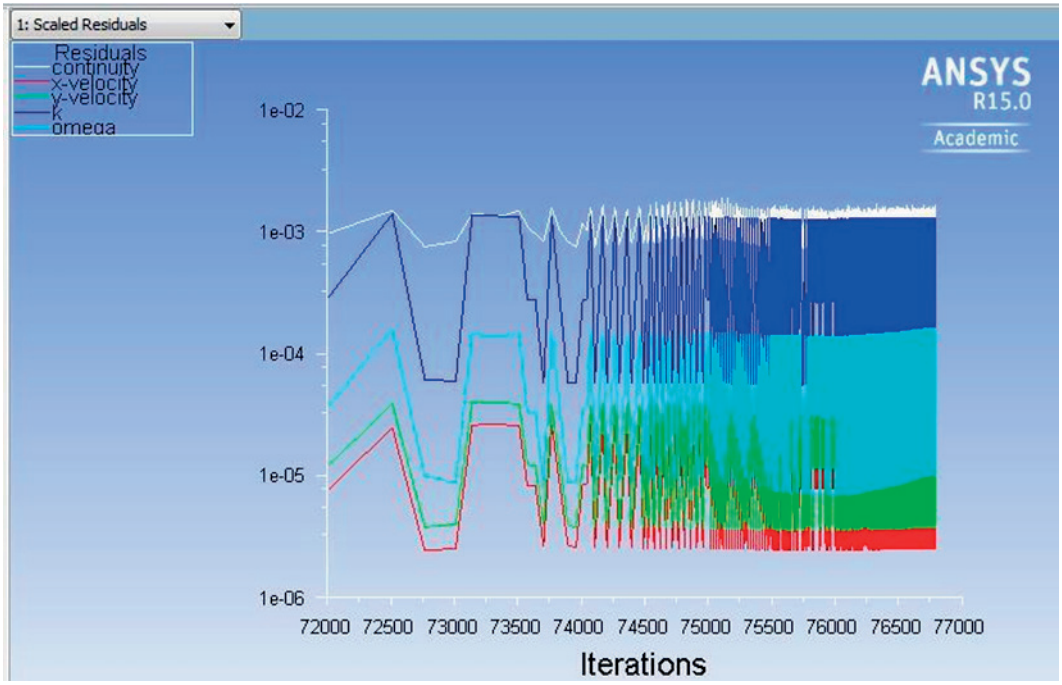

Figure 10. An example of the residual error monitoring in Ansys Fluent®15.0.

In some cases the CFD solver allows setting up the maximum number of iterations. But in that case the solver informs the user that the maximum number of iterations is achieved and the solution is not converged. Among the possible steps to proceed are to check the spatial and temporal discretization first, and to make sure the boundary conditions are realistic.

Another well-known hint to improve the solution convergence is to set the steady state solver before the time-dependent solver and to use the solution of this steady state solver as the initial condition for the time-dependent solver. In this case the time-dependent solver starts the simulation process not from the empty computational domain but from the more realistic flow field within the computational domain. In Comsol Multiphysics®4.3a, this concept is implemented through the Frozen rotor tool as shown in Figure 11. In Ansys Fluent®15.0 this step is realised through the Solution initialization.

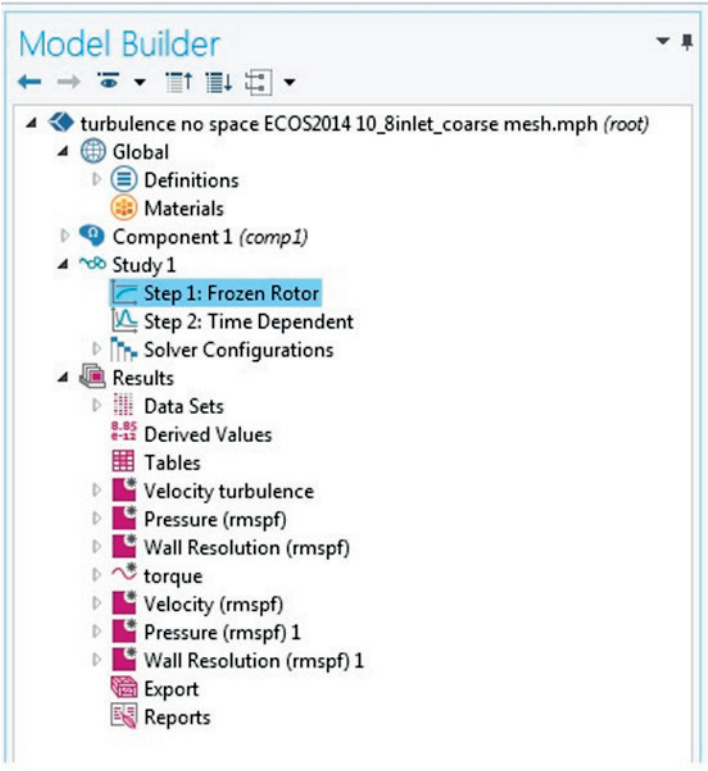

Figure 11. Illustration of the Frozen rotor tool in Comsol Multiphysics®4.3a.

Physical modelling error

The physical error is associated with the attempt to model the physical process. The uncertainty arises from the formulation of the mathematical model and approximation of the coefficients of the variables in the equations. (Tu et al. 2013) As an example, the incorporation of the Boussinesq approximation and turbulence stresses through the viscous stresses in the Navier-Stokes equation causes an uncertainty. As far as a model allows receiving results validated by experimental data, the model is considered acceptable. The main sources of the uncertainty of modelling of the physical process are as follows:

(i) The physical phenomena are not properly understood,

(ii) Empirical coefficients within the mathematical model possess some degree of uncertainty, and

(iii)Model validation is not possible or incomplete.

General comprehension of the numerical errors

The numerical errors can be represented primarily as consisting of the discretization and rounding-off errors. As it is concluded from the previous analysis the means to eliminate them are controversial. As the mesh or time step decreases the discretization error decreases but the rounding-off error increases. The reason is that more mesh cells involve more operations and hence larger total rounding-off error. When the sum of the discretization and rounding-off errors is considered, continuous mesh refinements do not necessarily entail that more accurate solutions are attained. In the contrary, too coarse mesh shrinks the total rounding-off error and magnifies the discretization error. In order to control these contradictory processes necessary steps have to be taken to secure the accuracy of the numerical solution.

The grid independence or grid convergence must be achieved. Either the GCIs are to be calculated and analysed or the Richardson extrapolation is to be applied if large number of simulations is to be performed.

The repetition of the simulations using the double-precision solvers allows for estimating the rounding-off error. If the obtained results do not change drastically then other sources of the errors are to be analysed. Otherwise, the number of operations can be decreased either by coarsening the mesh or decreasing the discretization order. The latter action should not increase the discretization error radically if the mesh or time steps are small already.

Verification and validation

With all the errors and uncertainties of the numerical modelling discussed, the question arises as to how the credibility of a CFD solution can be certified. Verification and validation procedures serve as the answer to this question. They are applied in two principally different ways.

The verification process allows for addressing the uncertainty and, if possible, the error of the simulation by means of provided input parameters of geometry, initial and boundary conditions. The sensitivity analysis of the discretization parameters, such as mesh and time steps, has to be performed.

The validation process allows for assessing the uncertainty and the error of the model using the data obtained experimentally. This procedure includes the establishing and application of the range of the physical conditions from the experimental setup and performing the comparison of the results from the CFD

model with the data obtained experimentally. The validation of the model of Ansys Fluent is described in section 3.2.

3 IMPROVEMENT OF THE AERODYNAMIC EFFICIENCY OF A SAVONIUS WIND TURBINE

In order to improve the aerodynamic efficiency of a Savonius wind turbine the operating principle of the rotor needs to be revealed. A Savonius turbine is a vertical axis wind turbine, which has in the conventional configuration two identical semi-circular straight blades symmetrically assembled around the centre of rotation of the rotor and separated in this centre. Figure 12a shows top views of the conventional Savonius rotor with the rotor diameter D, blade diameter d and overlap distance e. In this thesis the overlap distance is measured from the outer surface of the blades. The centre of rotation is at the centre of coordinate system. Figure 12b shows schematically the shape of the conventional Savonius rotor.

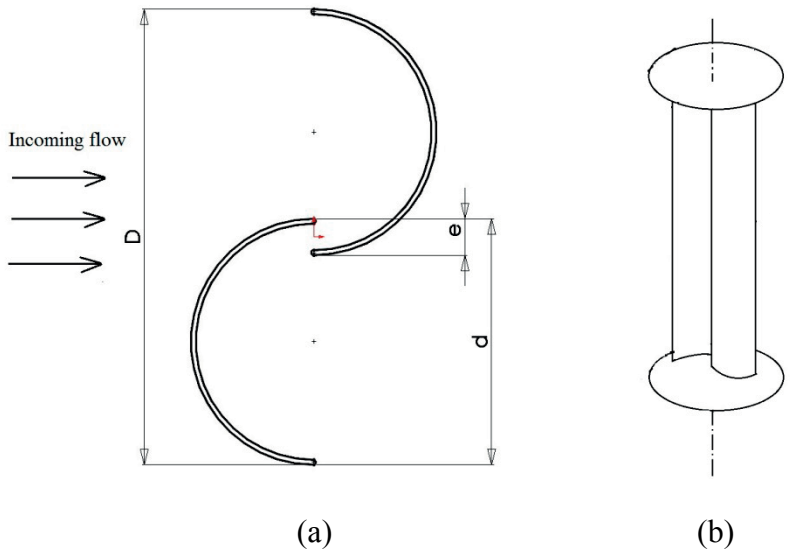

Figure 12. Configuration and geometrical parameters of the conventional Savonius rotor.

In this configuration the rotor rotates in clockwise direction, similar to a cup anemometer; the fluid flow is allowed to pass through the buckets of the rotor with overlap. The term “buckets” means the rotor blades. The principle of design and manufacturing process are simple: the basic Savonius rotor can be manufactured by cutting any cylindrical-shaped object in half and sliding them in the direction of the cutting plane.

The following aspects should be pointed out.

(i) Thereafter the blade moving in the incoming wind direction is referred as the “advancing blade” and the blade moving opposite to the wind as “returning blade”. The windward side of the advancing and the leeward side of the returning blade are referred as “concave” surfaces, hence the windward side of the returning and leeward side of the advancing blade are denoted as “convex” surfaces;

(ii) In practical designs of a turbine the central shaft may be added, however, the rigidity of a rotor can be provided also by the end plates. In this thesis the central shaft is not considered since the flow in the central part of the rotor is expected to change the rotor characteristics;

(iii) The direction of rotation of a rotor depends on the inlet flow direction and rotor blades position relatively to the centre of rotation. With the configuration shown in Figure 12a the rotor rotates in the clockwise direction;

(iv) Also, some wind turbines are equipped with the end plates as shown in Figure 12b. In this thesis the effect of the end plates is not modelled since the numerical model is two-dimensional.

Various methods have been applied by researchers for obtaining detailed information on the flow field around a Savonius rotor. The visualisation techniques, such as smoke-wire or particle image velocimetry, allows for obtaining only qualitative information on the flow variation around a rotor. (Fujisawa et al. 1992, Dobrev et al. 2011) More quantitative information on the flow around a Savonius rotor was obtained using the pressure distribution on the blade surfaces. (Dobrev et al. 2011, Zhou et al. 2013) These studies provide a better understanding of the mechanism of the power generation by Savonius turbines.

Figure 13 shows schematically the main flow patterns around buckets of a Savonius rotor. These flows have an effect on the power characteristics of the turbine. Pressure distribution along the rotor blades at this rotor position is shown on Figure A.5.5.

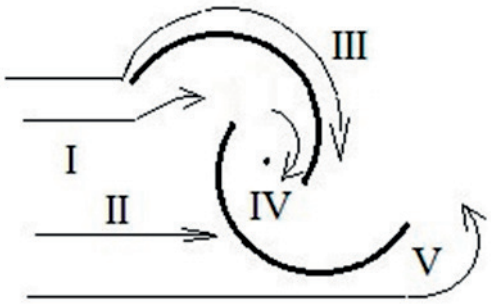

Figure 13. Schematic picture of the main flow patterns on a Savonius rotor.

The flow (I) creates the drag force on the advancing blade. The flow (II) creates the drag force on the returning blade and increases the negative torque from this blade. The flow (III) is so-called Coanda-like flow, with the turbine rotation it turns into flows which restore the pressure on the concave side of the returning blade. The Coanda-like flow is observed for rotor angles up to 45°. These flows contribute to the positive torque of the rotor. The flow in the central part of the rotor is described below in this chapter. A Savonius turbine is classified, as a rule, as a drag device. However, recent studies clearly demonstrate the contribution of the lift forces to the total torque value (Zhou et al. 2013).

A torque produced by a Savonius rotor at constant angular velocity and inlet wind conditions varies cyclically during one period of rotation. The stabilization of the torque values obtained using the numerical model is shown in Figure 14. In Comsol Multiphysics®4.3a, the total torque value is obtained by the integration of the stresses along the rotor surface as follows:

(19) $$T = \mathrm{int\,op}\left(|x|\mathrm{rmspf.T\_stressy} + |y|\mathrm{rmspf.T\_stressx}\right).$$

In Eq. 19 the integration operator “intop” is applied to the surface of the rotor, which was defined at the Definition section; the notation “rmspf” is referred to the Rotating Machinery CFD module and “stressx” and “stressy” are stresses in x and y coordinate directions.

In Ansys Fluent®15.0 a moment coefficient is recorded at each time step after the force monitor is created. The stresses are integrated along the rotor surface, specified at the geometry generation stage. The special control has to be taken when the reference values are set. In Figure 15 the Depth is the rotor height and Length is the rotor diameter, and the Area is the swept area of the rotor. A moment coefficient is defined with the use of torque by Eq. (20).

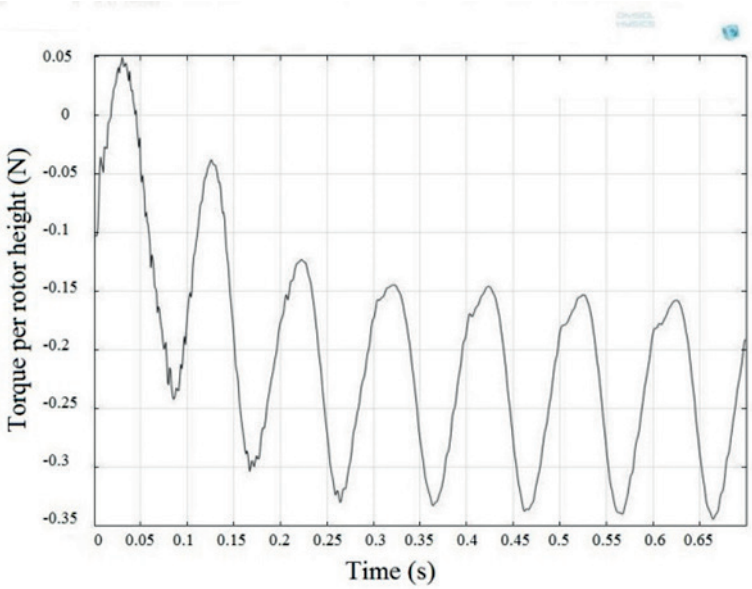

Figure 14. Torque per rotor height as a function of time in the model of Comsol Multiphysics.

(20) $$C_m = \frac{T}{\frac{1}{2}\rho \cdot u^2 \cdot A \cdot R},$$

where ρ is fluid density, u is incoming wind speed, A is the rotor swept area and R is rotor radius.

The power coefficient is obtained using the moment coefficient by Eq. (21).

(21) $$C_p = \frac{T \cdot \omega}{\frac{1}{2}\rho \cdot u^3 \cdot A} = C_m \cdot \lambda,$$

where λ is the TSR.

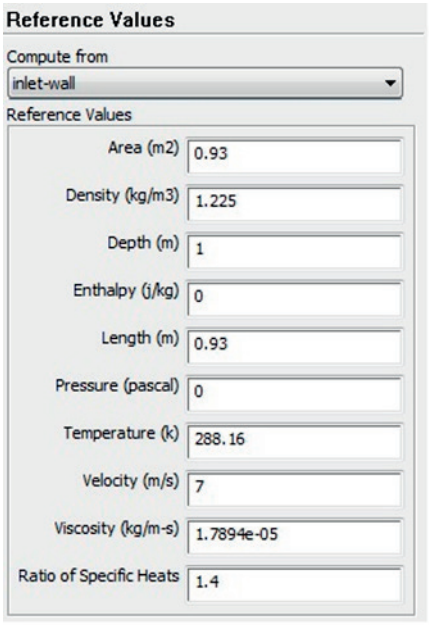

Figure 15. Specification of the reference values in Ansys Fluent®15.0.

A number of assumptions of the Savonius model have to be pointed out. The assumptions of the physical model and the assumptions of the numerical model are to be distinguished. Firstly, the physical model characteristics are selected: dimensionality, power coefficient estimation and inlet flow regime; and then each numerical model add specific assumptions of the simulation procedure. The following assumptions of the Savonius rotor model are common for both the Comsol Multiphysics and the Ansys Fluent numerical models:

(i) The rotor is studied under steady wind conditions, which is artificial to some extent because urban wind conditions are characterised by high level of wind speed variability. However, this simplifies the analysis of the rotor characteristics;

(ii) A two-dimensional model contradicts the three-dimensional nature of turbulence. Nevertheless, even a two-dimensional model allows for obtaining the torque and data on the flow field around the rotor in good accordance with validation data;

(iii) The two-dimensional model assumes the uniform distribution of the torque value along the rotor height. As a rule a three-dimensional model of Savonius rotor is created when the rotor is not symmetrical along the vertical axis. Because the assumption of uniform torque distribution along the rotor height is then not valid. The two-dimensional model is still a trade-off between the accuracy of the

numerical solution and the needed computational resources for three-dimensional models.

3.1 A review on the performance of Savonius wind turbine

Over the last few decades researchers have been studying the effect of various configurational aspects of a Savonius rotor and the flow characteristics on the overall turbine performance. Among these parameters are rotor end plates, overlap ratio, number of rotor stages, bucket shape and Re. Table 5 lists the main publications devoted to the analysis of these aspects.

It is noted that the most recent studies use numerical methods, followed by a comprehensive verification with or without validation, to study the effect of rotor configurations. This observation points out one of the aims of CFD applications and a procedure of their implementation: CFD models allow for performing a relatively affordable analysis of the most promising improvements of diverse devices or processes as the first step before a real prototype is built and tested.

Further in this chapter the most promising and interesting modifications of a Savonius rotor are presented and analysed.

Table 5. Details of the studies on the performance of different types of Savonius wind turbine.

	Study type	**Rotor profile**	**Re·10³**	**U_{inlet} (m/s)**	**Maximum C_p**
Simonds and Bodek 1964	Field experiment	Semi-circular blades	variable	not reported	0.14
Alexander and Holownia 1978	Wind tunnel	Semi-circular blades	188	6	0.15
Blackwell et al. 1977	Wind tunnel	Semi-circular blades	867	7	0.24
Fujisawa 1992	Wind tunnel	Semi-circular blades	110	6	0.17
Saha and Rajkumar 2006	Wind tunnel	Twisted buckets	119	6–12	0.14
Saha et al. 2008	Wind tunnel	Twisted buckets	61	not reported	0.32
Kamoji et al. 2009	Wind tunnel	hook-type rotor	150	not reported	0.21
Kamoji et al. 2009	Wind tunnel	Helical rotor	202	not reported	0.2
Gavalda et al. 1991	Wind tunnel	Semi-circular blades	700	8.4	0.22
Damak et al. 2013	Wind tunnel	Helical rotor	147	12.7	0.24
Zhao et al. 2009	Numerical method	Helical rotor	200	10	0.21
Mohamed et al. 2011	Numerical method	Semi-circular blades	not reported	not reported	0.3
D'Alessandro et al. 2010	Numerical method	Semi-circular blades	294	6–12	0.25

Aspect ratio and end plates

Application of end plates enhances the power extraction by the rotor. The end plates prevent the air to escape from the top and the bottom parts of the bucket to the external flow. The optimal size of the end plate has been found to be 1.1 times the rotor diameter. (Saha et al. 2008, Akwa et al. 2012 a) One of the modifications, proposed by the author for future study, could be a thin slit in the plate next to the point of the blade connection to the end plate. Figure 16 schematically illustrates this modification. This slit allows for the air shading from the convex side of the returning blade and hence decreases the pressure and negative torque from this blade. The positive effect is expected to be eliminated to some extent since the air through the slit increases the pressure on the concave side of the advancing blade and decreases the lift force.

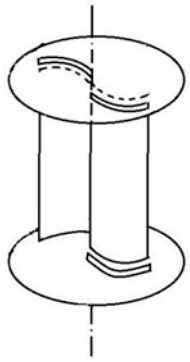

Figure 16. Modified end plates of a Savonius rotor with added thin slits on the end plates.

A relation between the rotor height and diameter is called the aspect ratio. The optimal aspect ratio is around 2.0. (Akwa et al. 2012 b) To some extent an increase in the aspect ratio with the constant rotor diameter produces the same effect as the addition of the end plates.

To the authors best knowledge, the estimation of the maximum allowed height and diameter of a Savonius turbine has not yet been done. Such an analysis includes calculation of mechanical stresses and fatigue forces along the rotor height. In addition, the wind speed profile and Re vary with the height above the ground and in order to keep each part of the rotor operating with the same TSR, the radius of the rotor has to be variable along the rotor height. If a power exponent model is taken to define the wind speed as a function of the height above the ground, the radius of the rotor section is established as follows:

(22) $$\mathrm{TSR} = \frac{\omega R_r}{U_r} = \frac{\omega R_i}{U_i} = \frac{\omega R_i}{U_r\left(\frac{z_i}{z_r}\right)^{\gamma}} \Rightarrow R_i = R_r\left(\frac{z_i}{z_r}\right)^{\gamma},$$

where ω is rotating frequency of the rotor, R is radius, U is incoming wind speed and z is height above the ground. In Eq. (22), the index r refers to the height and radius at the ground and index i refers to the rotor section under interest. The coefficient γ is a wind shear exponent that depends on the roughness of the terrain. However, more comprehensive functions could be used as well.

Number of rotor stages and buckets

A Savonius rotor can be composed of a number of twisted, relatively to each other, rotors of the same radius as it is shown in Figure 17.

Figure 17. Savonius rotor composed by three stages, which are turned along the rotor axis.

The intention behind this modification is the increase of a starting torque of a rotor. The "starting torque" is a minimum torque required to make a rotor moving from a standstill. Within a range of rotor positions and incoming wind speeds the torque of a Savonius rotor may not be high enough to overcome the starting mechanical moment of a generator. Within multiple rotor stages at least one would be in a position favourable to the inlet air flow. Furthermore, the use of multiple stages allows for reducing the torque fluctuations (Akwa et al. 2012 b). The peak values of the torque are lower, since only one stage of the rotor is at the position of maximum power extraction. However, smooth operation of a rotating device is a positive feature to achieve.

Similar results can be obtained if a number of buckets increases. The most popular modification is an addition of a third blade. The configuration of the three-bladed Savonius rotor is shown in Figure 18 along with a conventional two-bladed Savonius rotor as a reference. The rotor D is not maintained due to the relocation of the buckets, while the blade diameter d is kept the same for both rotor models.

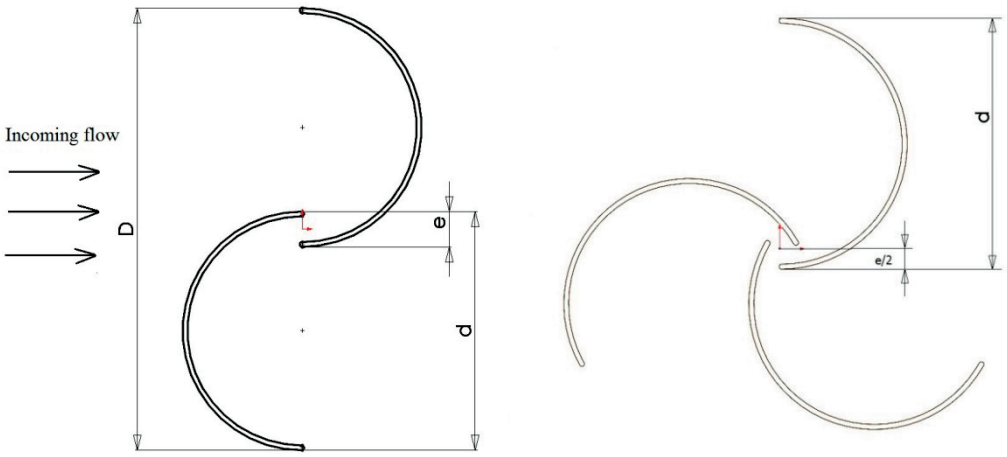

(a) (b)

Figure 18. The configuration of a Savonius rotor with two blades (a) and three blades (b).

Studies show that the dynamic torque of a Savonius rotor with three bucket varies less from the mean value, and this mean torque value is lower for the rotor with three blades. (Irabu et al. 2007, Akwa et al. 2012 b) This trend is shown in Figure 19. The graphs are obtained using the model of Ansys Fluent. The details of the numerical model are described later in this chapter, it is worth mentioning that the rotor diameter D is equal to 0.5 m and the overlap ratio e is 0.15·d for both rotor models. The mesh of the rotating domain of the three-bladed model is finer in comparison to the two-bladed model. In the three-bladed model the element size in the rotating domain is two times smaller than in the two-bladed model. The reason of this change is a more complex flow field around the three-bladed rotor. The solver with the standard mesh quality reports divergence in the pressure calculation.

A decrease in the averaged torque value is observed because the buckets of the three-bladed rotor are more closely located on the rotor and during rotation an incoming bucket receives the air flow instead of the advancing bucket. As a result, the advancing blade does not extract the power entirely from the air flow and less power is transformed into the mechanical power of the rotor. It could be argued, that the incoming blade is in turn becoming the advancing one. The moment arm of the advancing blade is longer, and this blade could have contributed more to the total torque. This effect can be observed in Figure 19 at the rotor angle 60°. At this angle, the moment coefficient of the rotor with two blades continues

increasing, and the moment coefficient of the rotor with three blades has achieved its maximum value.

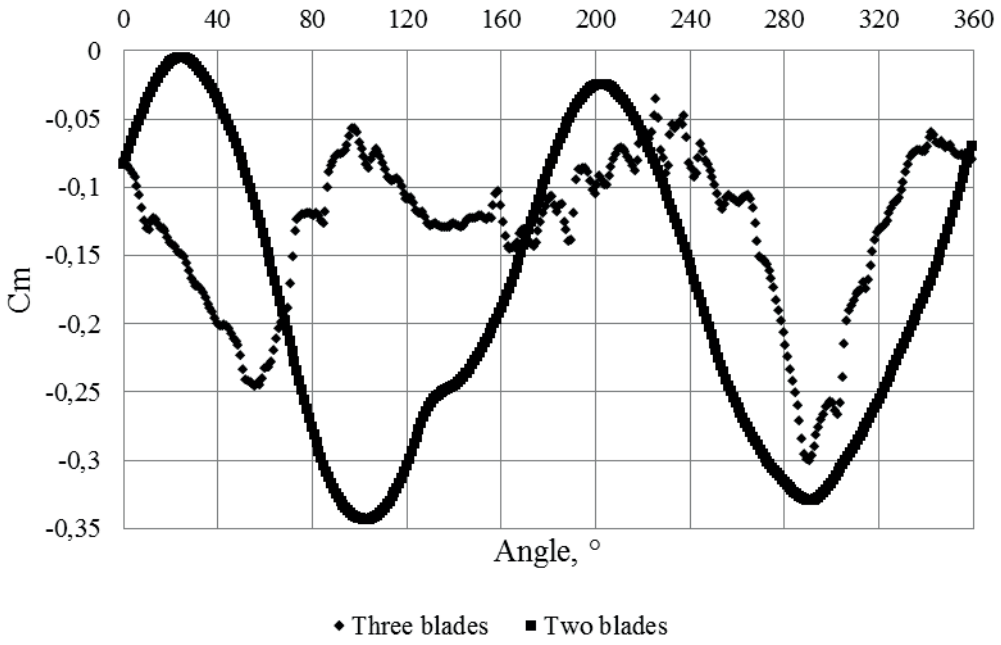

Figure 19. Moment coefficient of two-bladed and three-bladed rotor models as a function of rotor angle.

The flow guiding equipment

One of the ways to increase a total torque from a rotor is to eliminate the negative component from the rotor returning blade. Among the proposed ways to achieve this goal are a guide box with movable walls, curtains in front of the returning blade and movable blades. These methods are grouped in this section since the purpose of their application is to guide or direct the flow using external equipment.

A guide box with flexible walls aims to direct the inlet flow towards the advancing blade and to prevent shading of the air towards the returning blade. The walls are capable of turning to some range in order to track changes in the wind direction. This application is reported to increase the power coefficient of a rotor by up to 1.23 times. (Irabu et al. 2007)

The same idea is used when a curtain is placed in front of the returning blade. The curtain redirects the inlet flow from the returning blade towards the advancing blade. The rotor efficiency can be increased by up to 1.2 times. (Ogawa et al. 1989)

Both methods could be considered as a control system as well for a Savonius turbine, since they are capable of varying either the amount of air passing through the rotor or the inlet flow direction. However, it should be mentioned, that current applications of a Savonius wind turbine are of rather small power scale and do not typically need a system to control the power output. However, such a system could be used when regular gusty events are observed with the wind speeds as high as the cut-off values. Then curtains and boxes could be used to protect the turbine from extra mechanical loads.

Among the disadvantages of these applications are:

(i) The rotor is no longer independent of the inlet flow direction,

(ii) An additional automated system to control the guide box and curtain is required to follow the flow direction,

(iii) Additional equipment needs additional maintenance.

Another way to reduce the drag force on the convex side of the returning blade is to fix the blades at the tip points (points a and b in Figure 20) and make them able to rotate around the axes which are going through these points parallel to the rotor axis. In Figure 20 the dashed line shows the position of the returning blade if the movable wall concept is not applied.

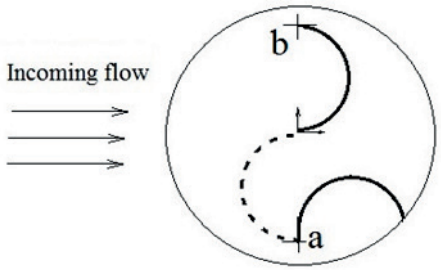

Figure 20. A schematic picture of a Savonius rotor with movable blades.

The negative torque from the returning blade decreases since this blade is now parallel to the flow. However, this air furthermore increases the pressure behind the advancing blade and decreases the positive torque from this blade. Despite the contradictory effects, the power coefficient is reported to increase up to a 7% with TSRs ranging from 0.5 to 0.6. (Aldos 1984) From maintenance management point of view a rotor with movable parts is expected to show disadvantageous performance.

Blade shape

The interaction between the air flow and rotor can be improved by applying an optimal blade shape. Among the most studied rotor shapes are the Bach-type (Zhou et al. 2013), the hooked-type (Kacprzak et al. 2013) and the so-called J-type profiles (Modi et al. 1984). They are also categorized together because all of them provide better performance of the rotor due to the air flow directed to the outer part of the bucket where the moment arm is longer.

A helical Savonius rotor is obtained combining the multistage design and transformed blade shape. It is shown by Saha et al. that starting torque of the helical rotor is less dependent on the rotor angular position in comparison to the torque of the conventional Savonius rotor (Saha et al. 2006). Kamoji et al. reported that a helical rotor with a twist angle of 90° is capable of initiating the rotation in the whole range of rotor positions (Kamoji et al. 2009). A helical rotor without an overlap and shaft attains better power coefficient. A higher twist angle of the turbine blades tends to improve the rotor performance to some extent. A helical rotor with the twist angle of 180° is considered to be made up by two helical rotors with twist of 90°, turned relative to each other. Zhao et al. reported an increase in the power coefficient from 0.15 for a conventional rotor up to 0.2 for a helical rotor (Zhao et al. 2009). However, rotors with higher twist angles of the blades have a lower aspect ratio for each section of the rotor, represented by 90° twisted helical rotors. Hence, the overall performance decays. It should be noted also that these improvements come with a price, since the manufacturing of a helical rotor is more complicated in comparison to a rotor with semi-circular blades.

Generally, it is observed, that the performance of a helical Savonius rotor follows the trends of a conventional Savonius rotor with respect to aspect ratio, end plate presence and overlap ratio.

Bucket spacing and overlap

Space between the buckets of a Savonius rotor can be added in the two coordinate directions relatively to the centre of rotation. In Figure 12a on page 33 the bucket spacing is equal to zero, but the blade overlap is not. Studies on the optimal bucket spacing have shown that absence of this space provides better performance of a Savonius rotor. The main reason being, that the leakage of air flow towards the returning blade through this bucket spacing does not let the air concentrate on the concave side of the advancing blade. (Khan 1978, Akwa et al. 2012 b)

One of the most promising and widely studied parameters of a Savonius rotor is an overlap ratio. An overlap ratio is defined as a ratio of the distance e to diameter D (see Figure 12a on page33). It is one of the key parameters determining the interaction between the flows around the rotor blades. It is shown by Fujisawa (1992), Kamoji (2009) and Akwa (2012 a, b) that an optimal operational overlap ratio is equal to 0.15. Ushiyama (1988) found that the starting torque increases with the overlap ratio between 0 and 0.2. However, due to variations in the testing conditions it is difficult to correlate the obtained results. The wind tunnel blockage factor (a rotor cross section over a wind tunnel cross section) and Re are among the major parameters affecting the test data.

The idea behind an increase in the overlap ratio is to allow the air flow to pass through the overlap, increasing the pressure behind the returning blade, decreasing thus its negative torque. However, with too large air gap the overlap flow (IV), as shown in Figure 21, redirects a considerable portion of the air away from the advancing blade. A reversed flow is observed on the concave side of the returning blade with the overlap ratios between 0.3 and 0.5 (Fujisawa 1992). A recirculation flow in the central part of the rotor is schematically shown in Figure 21. The recirculation flow raises in size with large overlaps, leading to increased rotor aerodynamic losses. Moreover, higher overlap ratios decrease the rotor diameter, reducing the rotor moment. An optimal overlap ratio provides balanced solution to the described contradictions.

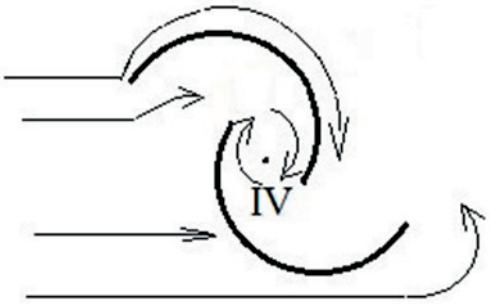

Figure 21. A recirculation flow in the central part of a Savonius rotor.

3.2 Numerical study on the performance of the Savonius wind turbine with gap flow guide

This section details the numerical analysis of the two-dimensional unsteady flow around two types of a Savonius turbine: the conventional and modified rotors. The modified rotor is realized by adding the gap flow guide to the advancing

blade of the rotor. The pressure distribution along the surfaces of both blades during one stabilized rotation was analysed in order to highlight the better performance of the modified rotor. Comparative studies of torque and power coefficient values of the two rotors were done in connection to the pressure variation analysis. The Ansys Fluent model is used for this analysis. The verification of the model is done partly in the previous chapters and is completed in the later chapters.

The selected overlap ratio of the conventional Savonius rotor is 0.15, which belongs to the reported optimum overlap range. The modified rotor repeats the configuration of the conventional rotor with the addition of the gap flow guide. The gap flow guide is a straight 0.1 m long continuation of the advancing blade which points towards the returning blade, deviated by 45° from the transversal line of the turbine as shown in Figure 22b. The diameter of the rotors is 0.93 m. It is maintained equal for the both rotors in order to provide the same swept area and Re. The blade thickness is 0.01 m.

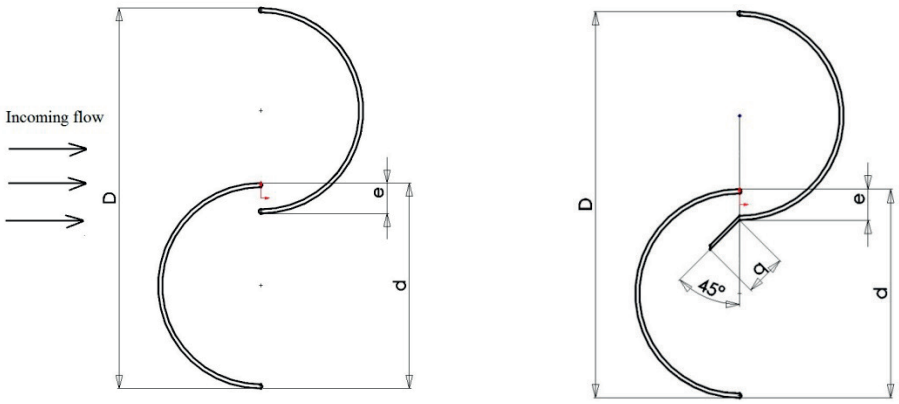

Figure 22. Configuration and geometrical parameters of the conventional rotor (a) and the modified rotor (b).

The rotor rotation is resolved with the use of the moving mesh concept within Ansys Fluent®15.0. Two sub-domains were distinguished inside the computational domain: stationary and rotating sub-domains. The computational domain is expanded on 4D to the inlet walls, 7D to the side walls and 15D to the outlet walls from the rotor centre.

The rotating sub-domain is discretized with the quadrilaterals and the stationary domain with squares. The computational domain and its discretization are shown in Figure 23.

One of the important features of a CFD model is mesh convergence. The mesh convergence means that the obtained numerical solution does not depend on the chosen grid quality. The fine mesh contains 250 000 elements and the coarse mesh contains 120 000 elements.

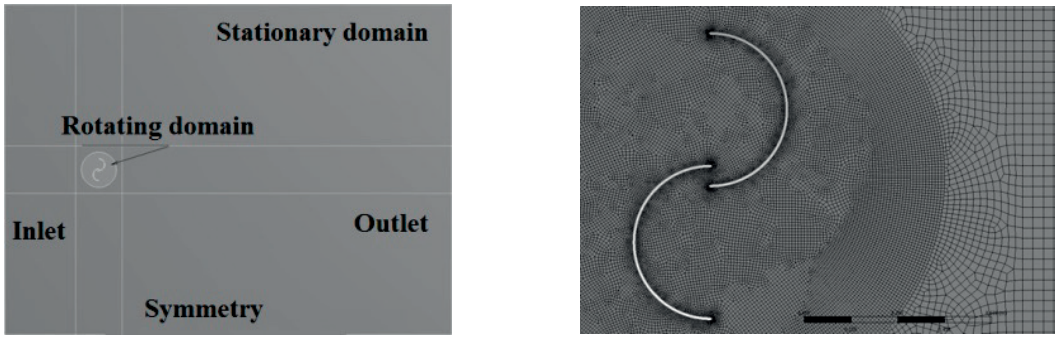

(a) (b)

Figure 23. Illustration of the computational domain (a) and the mesh (b) around the conventional Savonius rotor.

After repeating the calculations with the finer grid the estimated relative variation of the power coefficient is less than 0.5 %, thus the gird convergence is achieved. The time step for the simulation is set to match the CFL condition (see page 26), with a maximum limit equal to the time of one degree of rotor rotation. (Zhou et al. 2013, Shaheen et al. 2015)

Turbulence modelling

Due to the flow separation and time dependent nature of the flow around a Savonius rotor the modelling of the flow at the rotor boundary has to be done carefully. The unsteady RANS equations were solved with the use of the SIMPLE algorithm for the pressure-velocity coupling and the second order methods for the spatial discretization and the k-ω SST turbulence model. The k-ω SST model is suitable in modelling the flows with adverse pressure gradient and separation. A number of studies have employed this model since high accuracy of a numerical solution at the rotor boundary is needed to predict accurate aerodynamic characteristics of a Savonius rotor. (Kacprzak et al. 2013, Mohamed et al. 2011, Shaheen et al. 2015)

According to the requirements of the k-ω SST model the boundary layer around the rotor surface is resolved all the way to the wall. A distance from the rotor surface to the first mesh cell is calculated according to the Eq (A1.45).

Validation of the numerical model

The validation of the numerical model is discussed below. The validation study is performed based on the results published by the Sandia laboratory (Blackwell et al. 1977) and Loughborough University of Technology (Alexander et al. 1978). Generally, there are two ways to validate results of a simulation: to carry out an experiment in a wind tunnel or an open field experiment. However, a number of researchers have validated simulation models based on the results of the tunnel experiments, which are available in the publication databases.

Sun et al. (2012) used the results published by the Sandia laboratory on the performance of a Savonius rotor with two and three buckets as the reference values to validate the numerical model. The authors used different fluids in the numerical model after the validation is done. However, the success of the numerical model in predicting the power and torque coefficients makes this model valid. Shaheen et al. (2015) also used an existing experimental study to validate the simulation model.

This approach assumes that a numerical model is consistent and reliable if a numerical solution correlates with the experimental data. In this study the existing published results are taken as reference. The verification parameters of the numerical model repeat the reported parameters of the experiments. The geometry of the conventional Savonius rotor and the S-shaped rotor (conventional Savonius rotor without overlap) repeats the geometry of the reference rotors along with the incoming wind speed and Re. Two rotors with and without overlap were chosen in order to broad the validation of the numerical model. The sources of the divergence of the results, in addition to the errors discussed above and uncertainties of a numerical solution, are as follows:

(i) The numerical model is two-dimensional while the experimental model is three-dimensional,

(ii) The wind tunnel blockage effect is not taken into account,

(iii) The central shaft is not included in the geometry of the numerical model without overlap. However, the central part of the rotor without overlap does not affect considerably the rotor performance,

(iv) The thickness of the rotor buckets is not reported in the experiments verification, and

(v) The experimental rotors are equipped with end plates, while the two-dimensional numerical model does not take into account the effect of end plates.

All three models use the same verification parameters, such as the discretization method, mesh characteristics and time steps. The difference between the Sandia and Loughborough models is the rotor diameter and hence the size of the computational domains. Table 6 contains the verification parameters of the numerical models, which are used to model the rotors from the reference experiments. The incoming wind speed, the overlap ratio and radius and height of the rotors are obtained from the published details of the experiments. The computational domains of the numerical models are built according to the previously specified rules. The distances to the walls are given with the reference to the centre of rotation.

Table 6. Details of the parameters of the experiments set for the reference models.

Parameters of experiment	Sandia Laboratory 1	Sandia Laboratory 2	Loughborough University
R (m)	0.5	0.46	0.19
Height (m)	1	1	0.46
Incoming wind speed (m/s)	7	7	6
Overlap ratio	0	0.15	0
Domain size (m^2)	19·14	19·14	9·6
To the side walls (m)	7D	7D	7D
To the inlet wall (m)	4D	4D	4.7D
To the outlet wall (m)	15D	15D	17.9D

Good agreement is obtained between the results of the numerical models and the reference values. This is shown in Figures 24–26. These results allow considering the model of Ansys Fluent as verified and reliable for further simulation studies.

The discrepancy between the experimental and numerical results can be explained by the increase in the fraction of laminar flow at the rotor blade boundary layer with the increase of the TSR. The error becomes considerable at higher TSRs since the fully turbulent flow assumption, used by RANS turbulence models, is applied. (Kacprzak et al. 2013, Shaheen et al. 2015)

However, the major achievements in the power coefficient of the modified rotor are observed at the TSRs within the validated values (see Figure 27 on page 53).

Due to the fact that the modified rotor has the blade overlap, the rotor with the blade overlap studied in the Sandia laboratory (marked with the number 2 in

Table 6) was chosen for further analysis. It allows for further comparison of the performance of the modified Savonius rotor and the conventional Savonius rotor.

In the reference experimental model the incoming wind speed is 7 m/s. In this study the incoming wind speed is maintained constant. By varying the rotating frequency of the rotor, the variable TSRs are obtained, and, hence, the power coefficient and torque values as a function of TSR.

Simulations with different values of the incoming wind speed results into a number of curves of the power coefficient as a function of TSR. However, since the data for only a single value of the incoming wind speed is reported in the reference experiment, the numerical results for other values of the inlet wind speed are not necessarily validated. It can only be assumed that the error of the numerical solution, obtained for the incoming wind speed of 7 m/s applies for other numerical solutions with wind speeds other than 7 m/s.

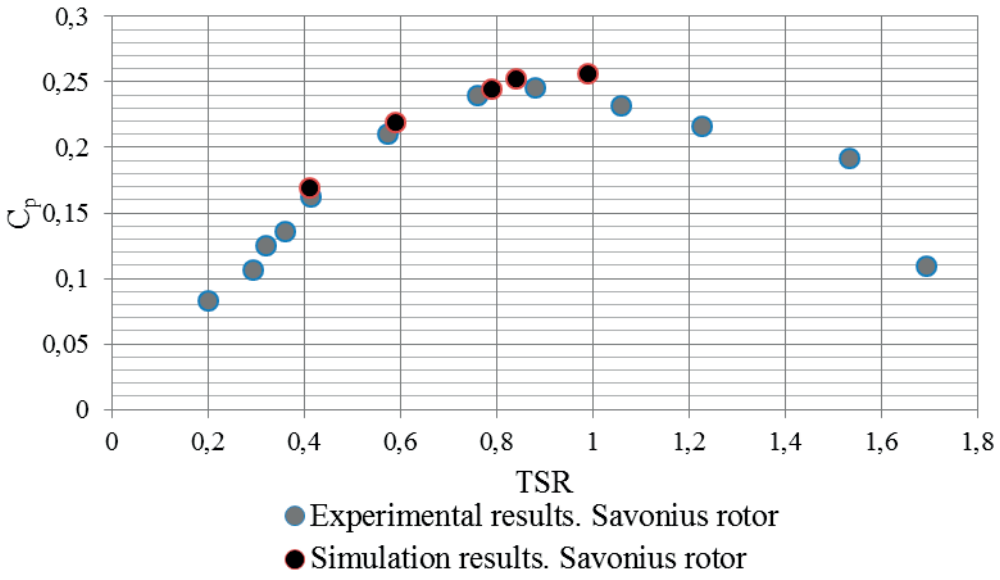

Figure 24. Power coefficient of conventional Savonius rotor at different TSRs: experimental results of Sandia laboratory 2 and simulation results. (Blackwell et al. 1977)

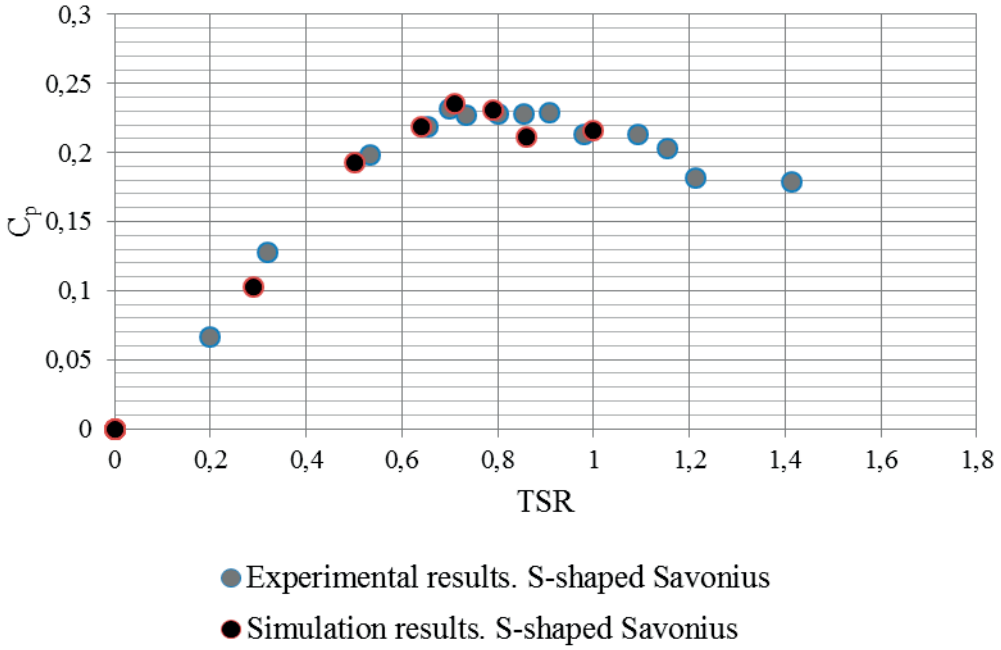

Figure 25. Power coefficient of the S-shaped Savonius rotor at different TSRs: experimental results of the Sandia laboratory 1 and simulation results. (Blackwell et al. 1977)

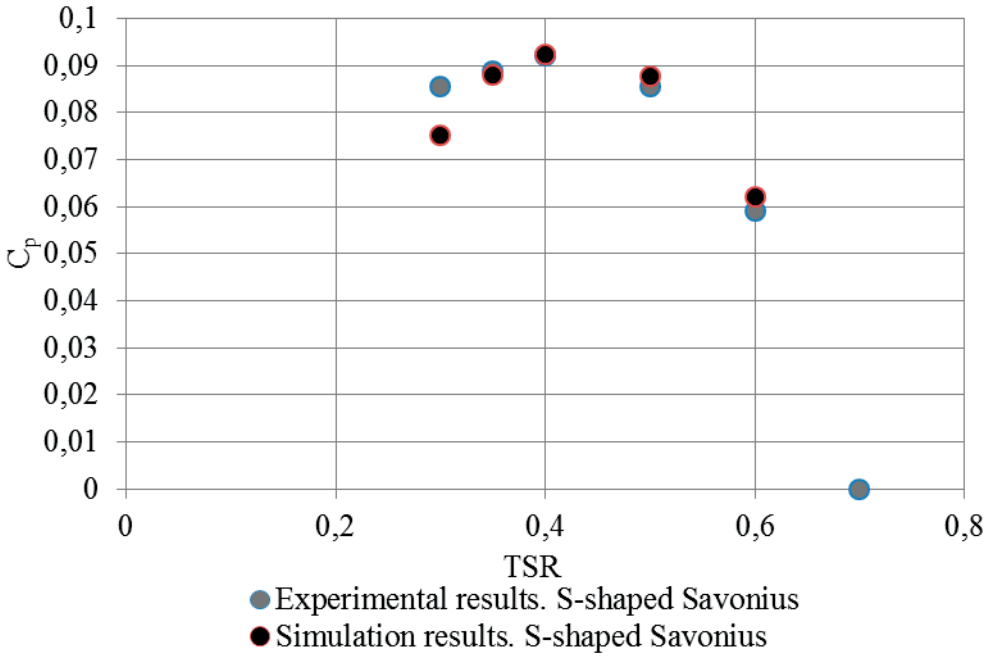

Figure 26. Power coefficient of the S-shaped Savonius rotor at different TSRs: experimental results of Loughborough university laboratory and simulation results. (Alexander et al. 1978)

Rotor modification

It was reported by many researchers that the Coanda-like flow and the overlap flow changes the pressure distribution along the blade surfaces and increases the turbine overall torque (Zhou et al. 2013, Akwa et al. 2012). Figures 24 and 25 also show an increase in the power coefficient of the Savonius turbine with overlap in comparison with the S-shaped Savonius turbine. In addition, the overlap improves the starting characteristics of a Savonius rotor, which is a crucial parameter for VAWTs.

The idea behind the current modification is to keep the overlap between the blades while eliminating its negative effect on the pressure distribution on the convex side of the advancing blade. As can be seen from Figure 22b on page 47 that the added gap flow guide is intended to direct the flow through the blade gap towards the returning blade, increasing the pressure and drag force on this blade. At the same time the gap flow guide prevents the flow through the blade gap to increase the pressure on the convex side of the advancing blade.

Results and discussion

The moment coefficients of the modified and conventional rotors as a function of time are shown in Figure 27. A numerical solution is considered to be stable when the variation of the power coefficient is less than 0.005 over at least three rotations.

The final moment coefficient is obtained by averaging the moment coefficient values over the last stabilized rotations. The power coefficient is given by Eq. (21).

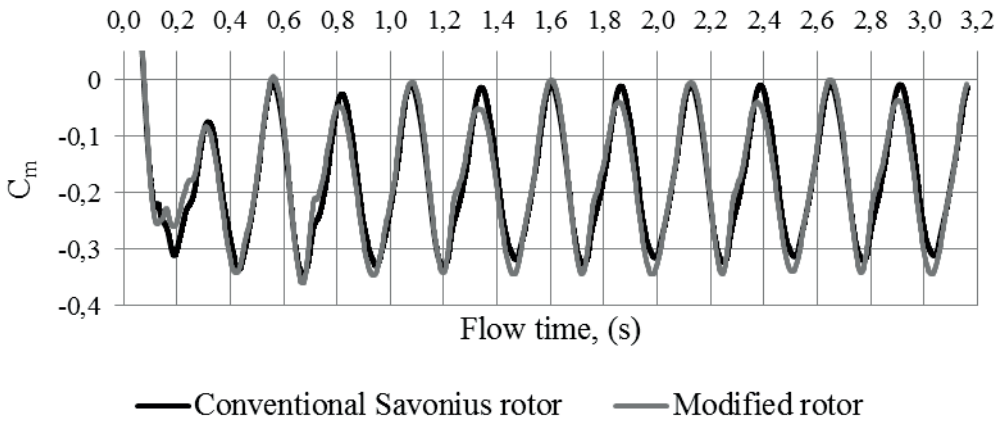

Figure 27. The moment coefficients of conventional and modified rotors as a function of flow time in the model of Ansys Fluent.

Figure 28 shows a slight increase in the power coefficient of the Savonius rotor with the gap flow guide at wide range of TSRs. It should be noted that the TSR with the maximum power coefficient for the modified rotor shifts towards slower rotation frequency. The lower the rotation frequency the more effective the gap flow guide is, because a bigger fraction of the flow is involved in the flow-structure interaction within the overlap.

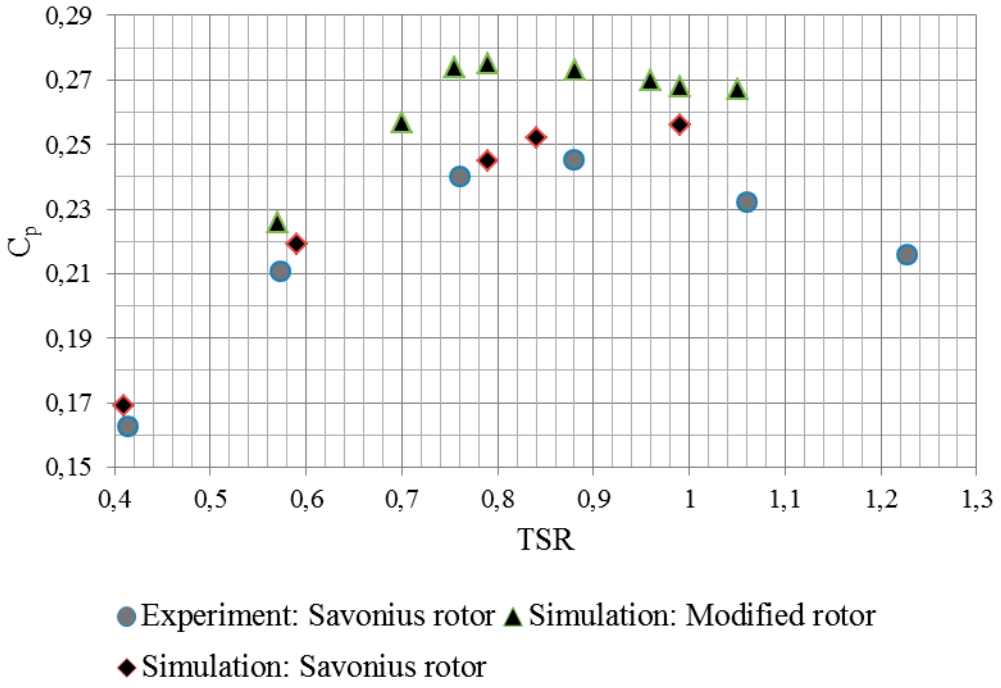

Figure 28. Power coefficient of studied rotors as a function of TSR.

The TSR is taken to be 0.8 for further analysis of the characteristics of the two rotors. This value provides the largest difference in the power coefficients of the rotors. Figure 22 shows zero degree rotation of both rotors; the rotation is clockwise according to the incoming flow direction and rotor configuration. Figure 29 shows the moment coefficient of the rotors during one stabilized rotation as a function of the rotor angular position. The moment coefficients of the modified rotor are bigger than that of the conventional Savonius rotor during almost half of one revolution time: 80°–115° and 180°–315°. However, it should be noted that the moment coefficient of the modified rotor exceeds the moment coefficient of the conventional rotor by up to 1.31 times (θ = 240°). The maximum moment coefficients of the modified rotor appear within the rotor angles of 100° and 280°. These values are 7% and 11% higher than the corresponding peak values for the conventional Savonius rotor at angles of 106° and 290° respectively.

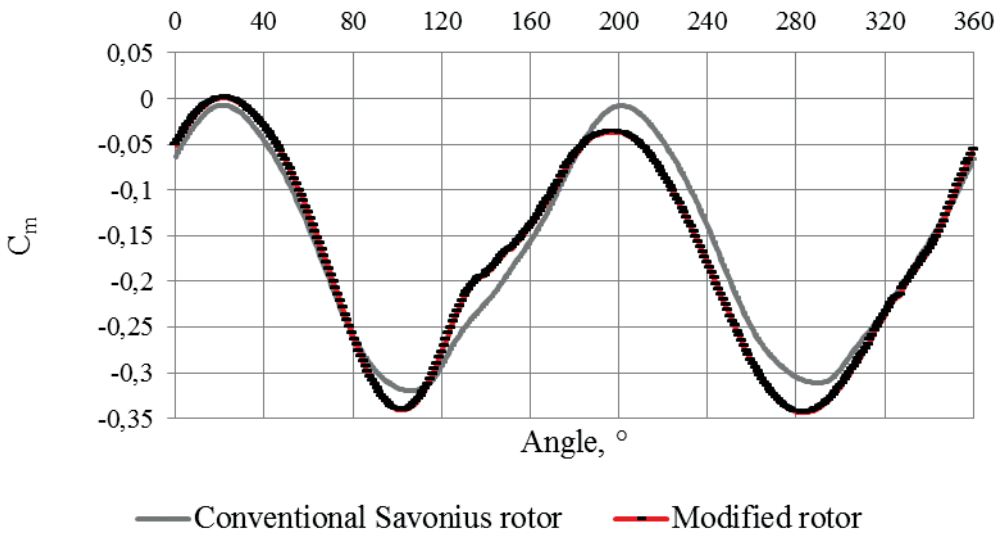

Figure 29. Moment coefficient as a function of rotor angular position for the conventional and modified Savonius rotors.

In order to investigate the effect of the gap flow guide the analysis of the static pressure distribution along the blade surfaces is done for the rotor position at 60°, 100°, 240° and 280°. The moment coefficient function reaches maximum values with the rotor angles of 100° and 280°. The large absolute difference between the moment coefficients, attained at these rotor angles, makes it worth studying. In addition, the gap flow guide changes its position relative to the advancing blade every $\Delta\theta = 180°$, because each blade becomes advancing during half of the full rotation.

The static pressure as a function of the horizontal coordinate of each point on the blade surfaces at the specified angle of rotation is shown in Figures 30, 32 and 34. In order to orient on the figures the upper right quarter is assigned as the first quarter and the move is in the clockwise direction. The lines on the graph create loops with the inner areas representing the positive torque from the advancing blade and the negative torque from the returning blade.

The pressure on the convex side of the advancing blade varies for the modified rotor from −118 Pa to −134 Pa for 100° and 280° angles respectively. In turn the pressure on the convex side of the advancing blade due to the symmetrical configuration of the conventional rotor does not change considerably with the rotor half revolution: from −115 Pa to −117 Pa as shown in Figures 30–32.

The static pressure on the convex side of the advancing blade of the modified rotor does not vary drastically compared to that of the conventional rotor for the

rotor angle of 100° as shown in Figure 30. At this rotor position the gap flow guide is hidden from the flow by the advancing blade and the gap flow guide does not cause considerable changes in the pressure distribution. For the rotor angle of 280° the gap flow guide behaves as a continuation of the advancing blade and prevents the pressure to drop when the flow expands from the convex side of the advancing blade towards the concave side of the returning blade. This effect explains the significant difference in the pressure on the convex side of the two rotors as shown in Figure 33.

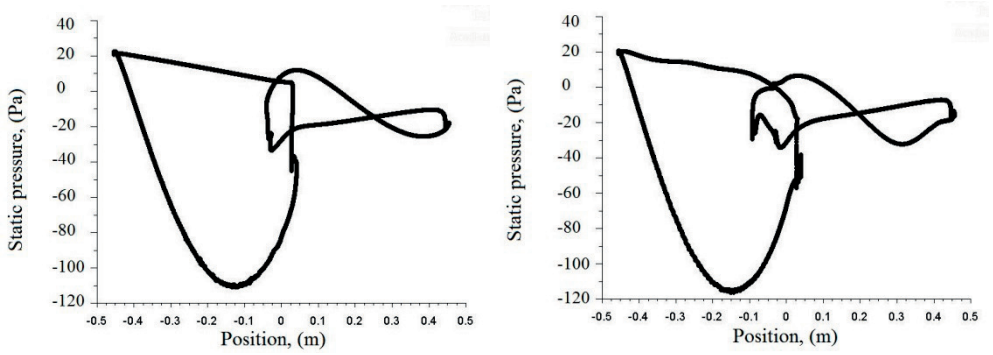

(a) (b)

Figure 30. Pressure distribution along the blade surfaces at rotor angle 100°: conventional rotor (a) and modified rotor (b).

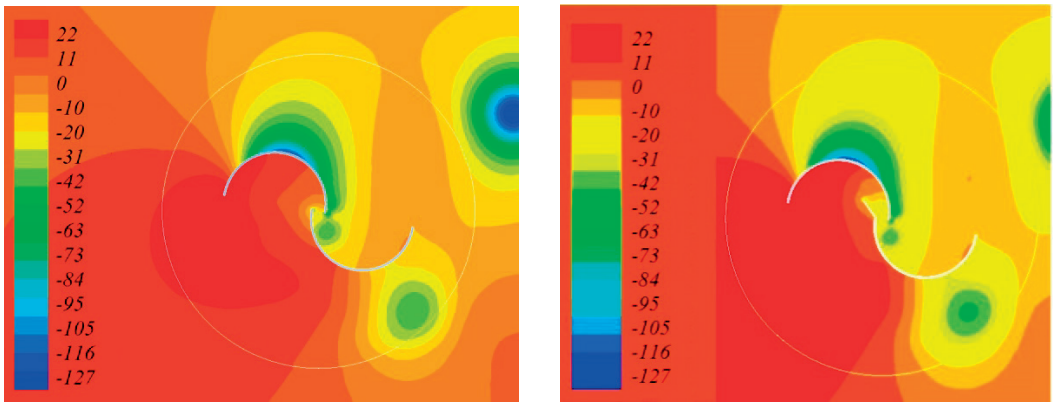

(a) (b)

Figure 31. Contour of pressure distribution along the blade surfaces at rotor angle 100°: conventional rotor (a) and modified rotor (b).

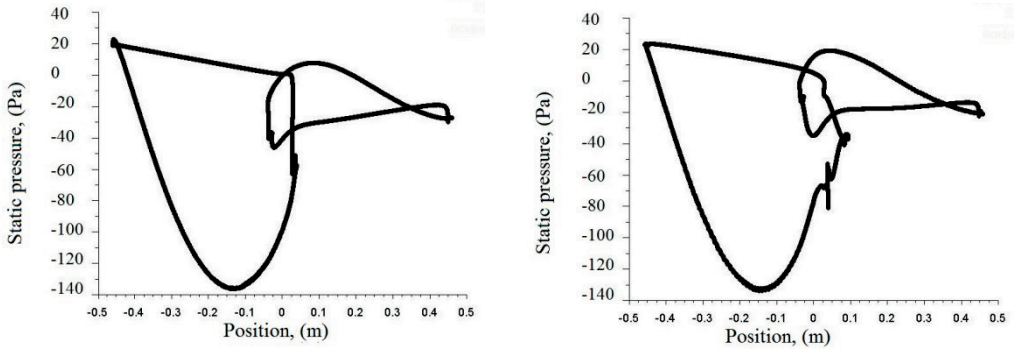

Figure 32. Pressure distribution along the blade surfaces at rotor angle 280°: conventional rotor (a) and modified rotor (b).

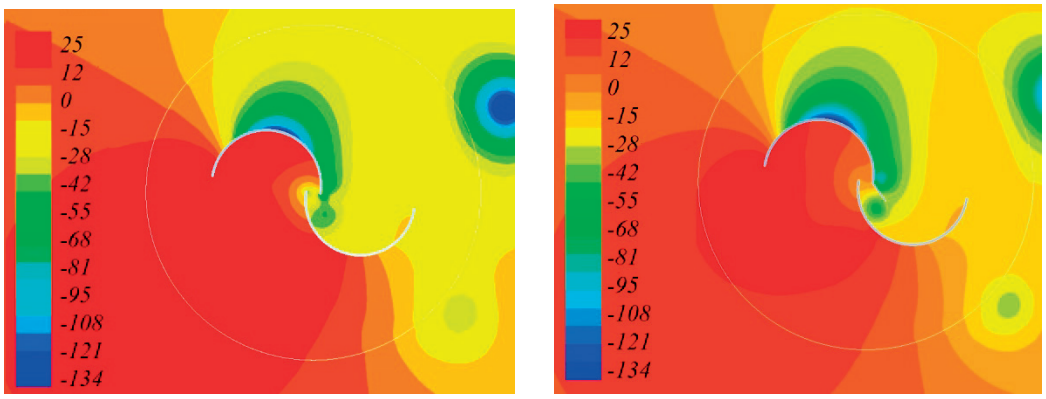

Figure 33. Contour of pressure distribution along the blade surfaces at rotor angle 280°: conventional rotor (a) and modified rotor (b).

The difference between the moment coefficients of the studied rotors is the largest for the rotor angle of 240°. The major variations in the pressure distribution along the blade surfaces occur in the root part of the advancing blade between concave and convex blade sides as shown in Figures 34–35. This pressure difference makes the biggest contribution to the torque. Figure 34b shows that the pressure on the convex side of the modified rotor blade is larger in the third quarter in comparison to the conventional rotor: –119 Pa and –105 Pa respectively. Moreover, the difference between the pressure values on the two sides of the root part of this blade is larger for the modified rotor: around 100 Pa and 77 Pa for modified and conventional rotor respectively. This pressure difference makes the biggest contribution to the higher torque of the modified rotor.

The same trend is observed in the pressure distribution at the rotor angle of 60°, except for the lower values of the pressure difference: 90 Pa and 75 Pa for modified and conventional rotor respectively.

The more developed negative pressure zone is in the turbine central part as shown in Figure 38 and Figure 39. This pressure zone creates two opposite effects: an increase in the positive torque from the gap flow guide surface and increase in the negative torque from the root part of the returning blade surface. These pressure values are shown in Figure 34b with two loops in the turbine central part. They almost cancel out each other in the total torque value. Similar, but smaller, negative pressure zone is seen in Figure 35a. However, for the conventional rotor it has almost no effect on the total torque value.

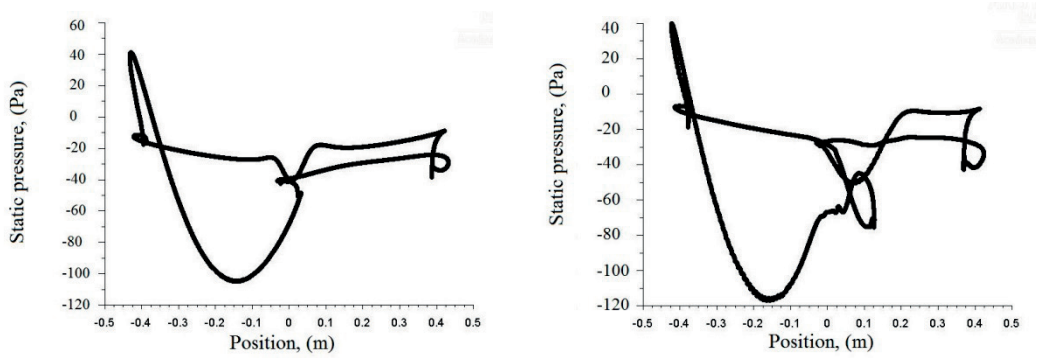

(a) (b)

Figure 34. Pressure distribution along the blade surfaces at rotor angle 240°: conventional rotor (a) and modified rotor (b).

There is an increase in the pressure on the convex side of the advancing blade of the modified rotor in comparison to the values at the corresponding rotor angles of the conventional rotor at angular positions from 180° to 310° and from 80° to 105°. As mentioned, this increase in the pressure leads to higher moment coefficients of the modified rotor at these rotor angles.

In addition, changes are observed in the pressure distribution along the convex and concave side of the returning blade. However, the biggest contribution to the increased power coefficient of the modified rotor is achieved by the increased pressure values on the convex side of the advancing blade.

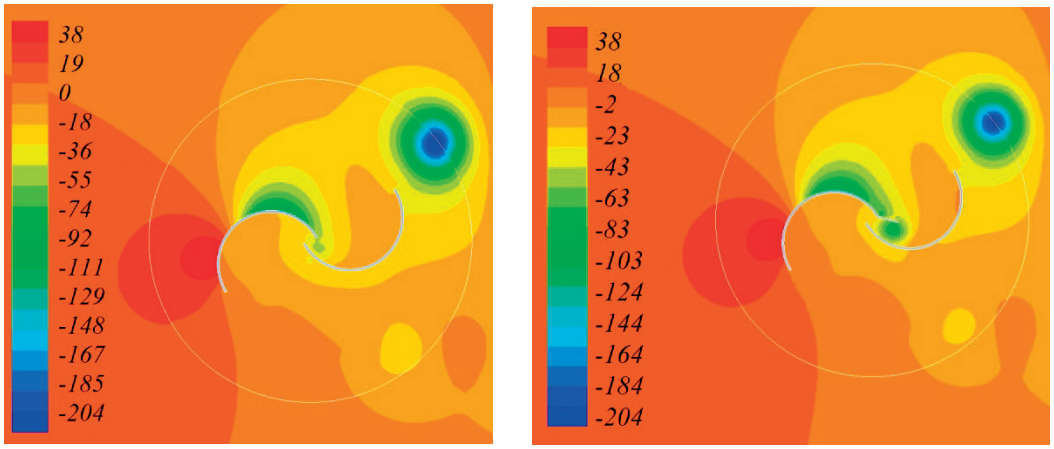

(a) (b)

Figure 35. Contour of pressure distribution along the blade surfaces at rotor angle 240°: conventional rotor (a) and modified rotor (b).

Conclusion

The aim of this study is to look for the possibilities to improve the performance of a conventional Savonius turbine in terms of the rotor power coefficient. For this to be achieved the two-dimensional flow over a conventional Savonius rotor and a modified Savonius rotor with one of the blades equipped with gap flow guide was numerically modelled. Ansys Fluent®15.0 was used to implement the simulation model. The numerical model was validated by comparing the obtained results with the experimental results by the Sandia laboratory and Loughborough University of Technology. This comparison shows reasonably good agreement in wide range of TSRs.

Based on the obtained simulation results a comparative study of the conventional Savonius rotor and the modified Savonius rotor can be carried out. The power coefficient as a function of TSR is the comparison parameter. The application of the gap flow guide was demonstrated to increase the power coefficient of the conventional Savonius rotor. The moment coefficients of the rotors during one stabilized rotation were obtained. The comparison of these values allows for distinction of the specific rotor angles where the torque of the modified Savonius rotor exceeds the torque of the conventional Savonius rotor. The pressure distribution along the blade surfaces of the rotors was examined. The most considerable changes were observed in the pressure values on the convex side of the advancing blades of the two rotors. Smaller variations in the pressure occurred on the surfaces of the returning blade. However, by the magnitude of these changes it was concluded that the major contribution to an increase in the

torque and hence in the power coefficient was attributed to the increased pressure on the convex side of the advancing blade of the modified rotor.

The implementation of the gap flow guide is considered to improve the performance of the conventional Savonius rotor while the major rotor advantages are maintained. The modified rotor operates in low wind speed region and it is independent of the wind direction. The gap flow guide is not expected to change the starting torque of the rotor significantly. Even with the gap flow guide facing the flow the gap between blades let the flow increase the pressure behind the returning blade.

The study of the effect of the variation of the gap flow guide parameters on the performance of a Savonius rotor could be the next step towards improvements of a rotor performance.

4 A SAVONIUS WIND TURBINE IN GUSTY WIND CONDITIONS

A commonly accepted procedure to analyse the characteristics of a wind turbine is the evaluation of the turbine operation under steady wind conditions. As a matter of fact, data obtained by this means give an overview of the turbine performance being artificial to some extent. The temporal and spatial unsteady nature of wind may be regarded as a source of uncertainties. Since the VAWTs are typically addressed as the most suitable type of wind turbines for wind power generation in urban areas, studies related to VAWTs should concentrate more on performance under unsteady wind conditions.

Several studies have been carried out on the performance of different types of VAWTs under unsteady wind conditions. The attention of researchers was focused on the H-type rotor (Kooiman 2010) and the Darrieus rotor (McIntosh 2009, Scheurich et al. 2013, Danao et al. 2013). In those studies the upstream flow velocity was fluctuating with time: the incoming wind speed was defined as a sine function and the rotating frequency of the rotor was kept constant. Throughout the reported studies the amplitude and the angular velocity of the sine functions were varied from 10 % to 50 % of the mean amplitude and from 1 Hz to 11 Hz respectively. Further in the present study the term “sine function” refers to the function which describes the variation in time of the modelled wind speed. Generally, the performance of studied VAWTs is shown to degrade with the increase of the amplitude of the sine function, while the frequency has minor effect. To the best of the author’s knowledge, the performance of a Savonius rotor in gusty wind conditions has not yet been widely studied.

The power coefficients of a Savonius rotor, which were discussed in the previous chapters of this study, were obtained under steady wind conditions: constant incoming wind speed, variable rotating frequency of a rotor and, as a result, different TSRs. Thus, the values of the power coefficient are dependent only on the TSR. As an example, in Figure 28 on page 54 the TSRs (0.7–1) with the corresponding highest power coefficients can be distinguished. However, with fast changes of the wind speed and in the absence of a control system (hence the ability to change the TSR) the turbine does not operate within the optimal regime during a gust period.

Along with the variable wind speeds unsteady wind conditions are characterized by the frequent changes in wind direction. It was claimed by Savonius, that the natural wind conditions cause differences to the results obtained under steady

wind conditions in wind tunnel. Wind turbines, which have to follow changes in the wind direction using pitch control or tail vane, cannot follow the changes in wind direction immediately and, hence, the inefficiencies occur. (Savonius, 1931: 333–334)

This part of the research, being focused on implementation of a Savonius turbine in urban areas, aims to investigate the performance of a Savonius rotor under unsteady wind conditions along with steady wind conditions.

4.1 VAWTs in urban wind conditions

The wind conditions within an urban environment differ from the wind conditions in typical onshore and offshore locations of wind turbines. The relatively dense presence of diverse obstacles (trees, buildings, constructions) in urban areas generates significant turbulence within the wind currents in stream wise, crosswise and vertical directions near the rooftop height and affect turbine operation.

When compared to the offshore sites urban wind conditions are characterised by reduced mean wind speeds and an increased level of gustiness up to 23% of the total available wind energy. When estimating the competitiveness of a decentralised wind power system in urban sites with an offshore counterpart, the decrease in the total wind energy resources in urban area has to be considered. In addition, short period gustiness has been shown to negatively affect the turbine performance in terms of induced vibration level. (McIntosh 2009)

Sources of wind unsteadiness

The wind velocity profile can be represented as a function of a particular planetary boundary layer. The unsteadiness within the atmospheric boundary layer is characterized by fluctuations of the instantaneous wind speed from the long term mean value (following Reynold's decomposition):

(23) $$u(t) = \bar{u} + u'(t),$$

where u(t) is the instantaneous wind speed, $\bar{u}$ is the mean wind speed and $u'(t)$ is the fluctuating wind speed.

These fluctuations can be represented in the form of power spectrum showing the average unsteady power content as a function of the wind speed frequency. The

first power spectrum as a function of the gust frequency was obtained by Van Der Hoven. (McIntosh 2009, Kooiman 2010) Based on this distribution the main subdivisions of the spectrum are the following.

(i) The macrometeorological, characterized by the diurnal solar heating and movement of large weather systems, for example, anticyclones. The time scale of such peaks is 12 hours;

(ii) The micrometeorological, described with the short time fluctuations caused by the mechanical shear and atmospheric instabilities with the time scale of 1 minute;

(iii) The mesometeorological, less relevant for the wind energy applications, characterised by a low power content. (McIntosh, 2009)

The unsteadiness of the wind can be characterized by a gust frequency, f_c, and a gust reduced frequency, K_g:

(24) $$f_c = \frac{1}{T},$$

(25) $$K_g = \frac{D}{\frac{\bar{u}}{f_c}},$$

where T is a period of the gust event, D is a rotor diameter and is mean wind speed during the gust event.

Gustiness and wind turbines

One of the main aerodynamic characteristics of a wind turbine is the maximum power coefficients and the corresponding TSR. A TSR varies by adjusting the rotating frequency of a turbine when the wind speed changes. As a result the TSRs may be kept within the optimal range. However, depending on the response time of a control system, a turbine may operate during a certain period of time without optimum TSR and hence less power would be produced. The shape of a rotor power curve does have an effect on the mentioned final losses. The more sloping the top part of the power curve the less the rotor dependency is on the variability of the wind speed over a short period of time.

One of the most important parameters of a wind turbine is the maximum power coefficient achieved by a rotor, but not the shape of the power curve. This

evaluation is valid when a rotor operates under steady wind conditions or if the control system of a turbine is fast enough to follow the changes of the wind speeds and adjust the rotation frequency. If these two conditions are not met the shape of the power curve becomes important.

4.2 Performance of a Savonius rotor under unsteady wind conditions

Based on this discussion and the numerical model of a Savonius rotor the following conditions are chosen for the analysis of a Savonius rotor performance under unsteady wind conditions.

(i) The inlet wind speed is described with a sine function with the mean value equal to 7 m/s, amplitude of 0.7 m/s and two angular velocities equal to 6 rad/s and 24 rad/s, hence the gust reduced frequencies equal to 0.24, 0.27 and 0.95, 1.08.

(ii) Under steady wind conditions the maximum power coefficient of a particular model of a Savonius turbine is obtained at the TSR of 0.8 (see Figure 28 on page 54). An analysis of the rotor performance under unsteady wind conditions with the TSR in the vicinity of 0.8 would provide the most valuable data. On the other hand, one rotation should contain an integer number of gust events in order to clarify the further analysis. The frequency of the gust events will be adjusted to this purpose since the period of one rotation is known from the TSR.

(iii) The rotating frequency of the rotor is maintained constant, thus, varying the value of the TSR at each time step. The power coefficient as a function of TSR is to be obtained.

The numerical model

The Ansys Fluent numerical model was chosen for the study of a Savonius rotor operation under unsteady wind conditions. The validation and verification of the model was reported previously in the Chapter 3 of this thesis. It should be noted, that despite unsteady wind conditions applied in this study the validation of the numerical model was done for steady wind conditions: the experimental model of the Sandia laboratory and the model of Ansys Fluent both use steady inlet wind conditions. Moreover, this validation approach was successfully applied and reported by Danao et al. (2013).

Within the numerical model the mean incoming wind speed is 7 m/s, the rotating frequency of the rotor is 12 rad/s, the rotor radius is 0.465 m, which corresponds to a TSR ratio 0.8 under steady wind conditions. The incoming wind speed profile is described by the sine function

(26) $$u(t) = 7 + 0.7 \cdot \sin(\omega \cdot t)\,,$$

where t is time (s) and ω is angular frequency (rad/s). The angular frequency ω has two values in order to attain two sets of the gust reduced frequency: 6 rad/s and 24 rad/s. According to the Figure 36 gust event corresponds to the half period of a sine function. The characteristics of gust events are calculated according to Eq. (24) and Eq. (25), and they are shown in Table 7.

Table 7. Characteristics of the studied gust events.

ω (rad/s)	Mean speed (m/s)	Gust period (s)	Gust frequency (Hz)	Gust reduced frequency
6	7.44	0.523	1.9	0.24
	6.56			0.27
24	7.44	0.131	7.63	0.95
	6.56			1.08

The angular frequency of 6 rad/s means that a rotor makes two full rotations per each sine period or one rotation per each gust period. Hence, a rotor operates in two regimes: a first full rotation when wind speed attains minimum and a second full rotation when wind speed attains maximum as shown in Figure 36.

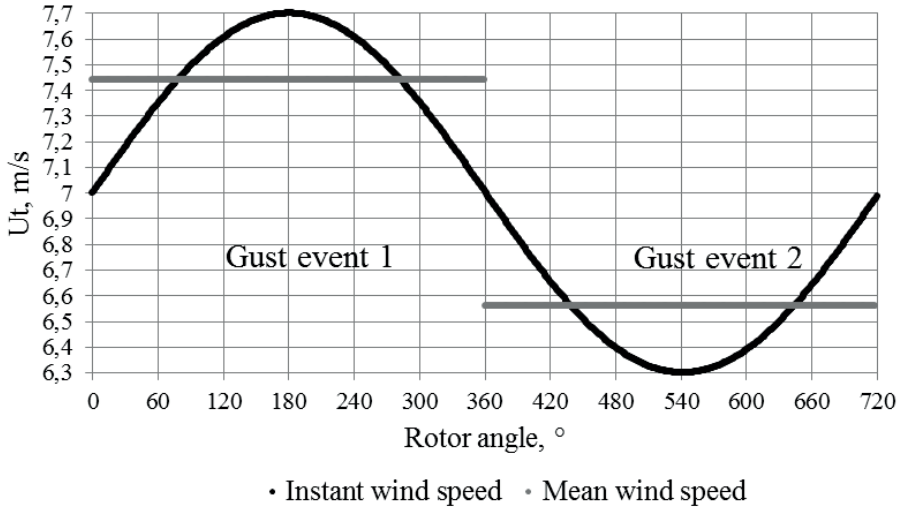

Figure 36. Incoming wind speed as a function of time with gust indication, K_g equals to 0.24 and 0.27.

The angular frequency of 24 rad/s means that a rotor makes half a rotation per each sine period and hence 0.25 rotations per each gust period. The time step of the simulation model is two times smaller than the time step for the first case, since the wind speed changes faster and hence smaller time step is needed to follow these changes.

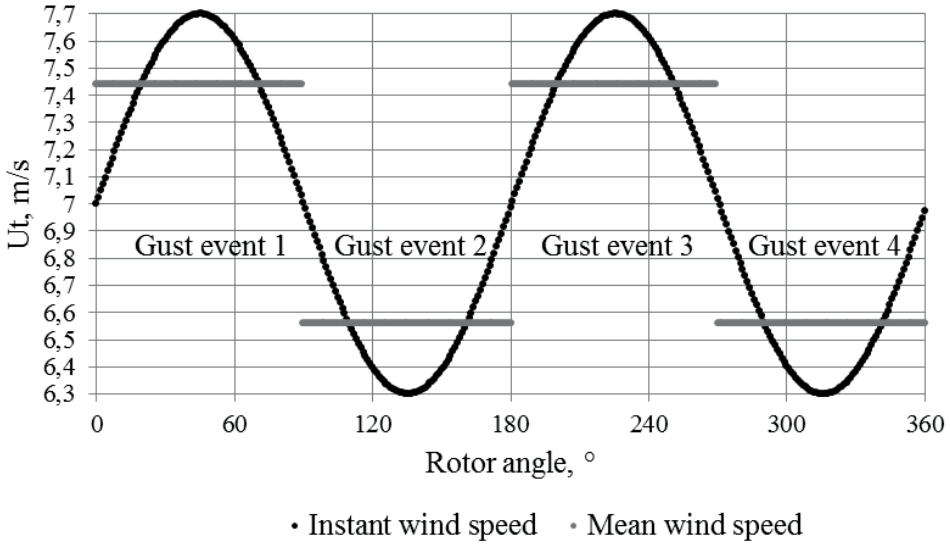

Figure 37. Incoming wind speed as a function of time with gust indication, K_g equals to 0.95 and 1.08.

The variable inlet velocity is specified using the user defined function (UDF). The .txt file with the UDF should be saved in the working directory. The UDF in Ansys Fluent®15.0 is implemented through the Define → User defined → Interpreted UDFs. Then the created .txt file is selected and uploaded. The UDF for the unsteady velocity profile with the mean wind speed of 7 m/s and the angular frequency of 6 rad/s is

```
#include "udf.h"
DEFINE_PROFILE(unsteady_velocity, thread, position)
{
face_t f;
real t = CURRENT_TIME;
real prof;
prof=7.+0.7*sin(6.*t);
begin_f_loop(f, thread)
{
F_PROFILE(f, thread, position) = prof;
}
end_f_loop(f, thread)
}
DEFINE_EXECUTE_AT_END(print_in_residuals)
{
real t = CURRENT_TIME;
real prof;
prof=7. + 0.7*sin(6*t);
printf("\nUDF_current_time=%f\nUDF_profile=%f\n",t,prof);
}
```

Here the last line allows for the monitoring the current incoming wind speed in order to make sure the UDF works properly. The inlet wall boundary condition is changed from “constant” to “unsteady_velocity”.

Turbulence models

Two turbulence models were tested under steady wind conditions. The first turbulence model is the k-ω SST model. The primary assumptions of the two-equation models are isotropy of Reynolds stresses and a local equilibrium of turbulence (production equals dissipation). The eddy viscosity approximation is used to model the Reynolds stresses, whilst this is not the most accurate model particularly for rotating or separated flows.

The Reynolds stresses can be represented through series expansions of the stress tensor (See Appendix 1 for details). The mentioned Boussinesq approximation contains only the first term from this formulation. The flow history effect is taken into account, which is important in the light of an unsteady flow under consideration. Nevertheless, the success of the Reynolds stress model is

moderate in predicting axisymmetric and unconfined recirculating flows, where it was shown to perform nor significantly better than the standard k-ε model. (Tu et al. 2013)

Within the model of Ansys Fluent the Reynolds stress turbulence model was chosen along with the k-ω SST model. The evaluation of accuracy of the Reynolds stress model was performed with the use of the numerical model under steady wind conditions. Since both models use LRN at the rotor surface all settings and parameters of the model of Ansys Fluent are maintained: computational domain, mesh generation and condition of $y^+ \leq 1$ at the rotor surface.

In spite of the higher complexity and computational cost of the Reynolds stress, the simulation with the k-ω SST turbulence model showed more accurate results for the torque and hence the power coefficient of a Savonius rotor under steady wind conditions. Figure 38 illustrates these results along with the experimental data (Blackwell 1977). For this reason the k-ω SST turbulence model is chosen for further modelling of the Savonius rotor under unsteady wind conditions.

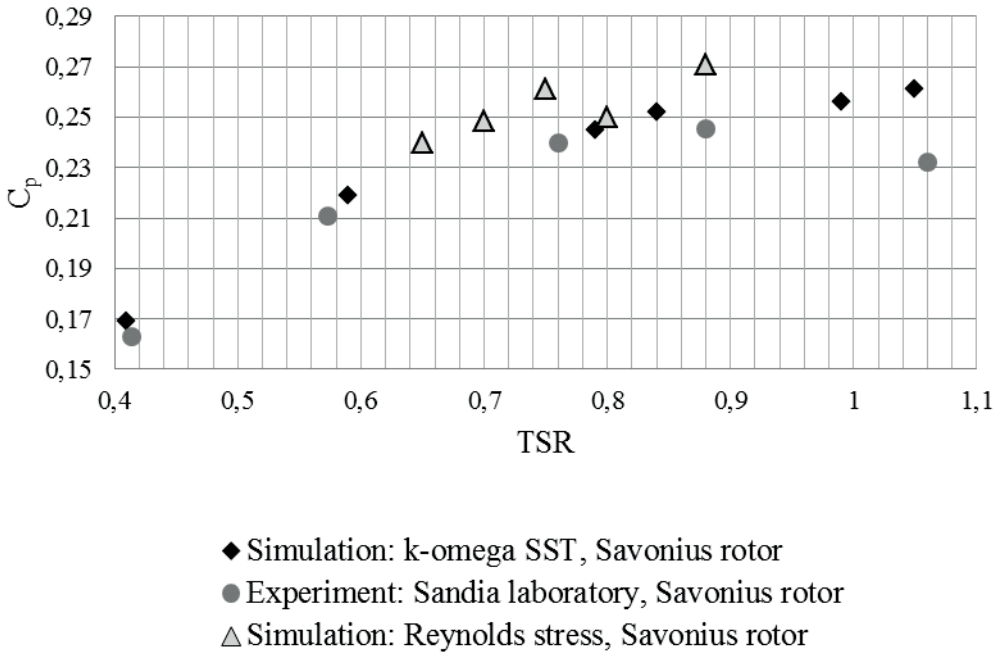

Figure 38. Power coefficient as a function of TSR obtained with the use of numerical models and experiment under steady wind conditions.

It has to be noted, that the application of the Reynolds stress turbulence model leads to a higher variability of the torque as a function of time within one rotating period under steady wind conditions. For the five calculation points presented in Figure 38 the first two (the TSR of 0.65 and 0.7) were obtained with the

stabilized torque values. Within the remaining three calculation points the torque varies in the range from 0.01 to 0.02 in terms of absolute values of torque and from 0.11 to 0.15 in terms of the absolute values of the power coefficient. One of the reasons for such overestimated results could be a more complex flow around the rotor at higher rotation frequencies.

Results and discussion

Figure 39 shows the power coefficient as a function of a TSR of the rotor under unsteady wind conditions with the gust reduced frequencies K_g of 0.24 and 0.27. In Figures 39 and 40 the power coefficients with the TSRs from 0.8 to 0.9 correspond to a mean incoming wind speed of 6.56 m/s and hence K_g equals to 0.27. The wind speed reaches the minimum value and the rotor tends to operate with TSRs which are closer to the optimum as shown by the function of the power coefficient under steady conditions. For this reason the maximum achieved power coefficients during this phase of the sine function were higher than the values achieved during the second part of the sine function with lower TSRs.

In contrast, the power coefficients with the TSR in the range from 0.7 to 0.8 correspond to the mean incoming wind speed of 7.44 m/s and hence K_g equals to 0.24. This decrease in the power coefficient illustrates the losses due to the absence of the control system. When the wind speed increases and the rotor continues to operate with the same rotation frequency, the TSR decreases, the moment from the generator behaves as a break for the rotor thus decreasing the power coefficient.

It should be noted that the power coefficient under steady wind conditions is obtained by averaging the torque over a stabilised rotation because the rotor torque is a function of time. In Figure 26 such a function is shown. It is possible to calculate the power coefficient as a function of time during one rotation under steady wind conditions too. As a result not only the averaged power coefficient may be obtained, but also the instantaneous values of the power coefficient under steady wind conditions.

The averaged power coefficient obtained by the rotor under steady wind conditions is presented as a point in the graph in Figures 39–42, and the “variation bars” denote the variation of the power coefficient over a rotor revolution. The peaks of the power coefficients of the rotor operating with the gust with Kg of 0.24 and 0.27 are almost identical to the corresponding peaks of the power coefficient under steady wind conditions, while the corresponding values of the TSR of these peaks do not coincide. This is illustrated in Figures 39 and 40.

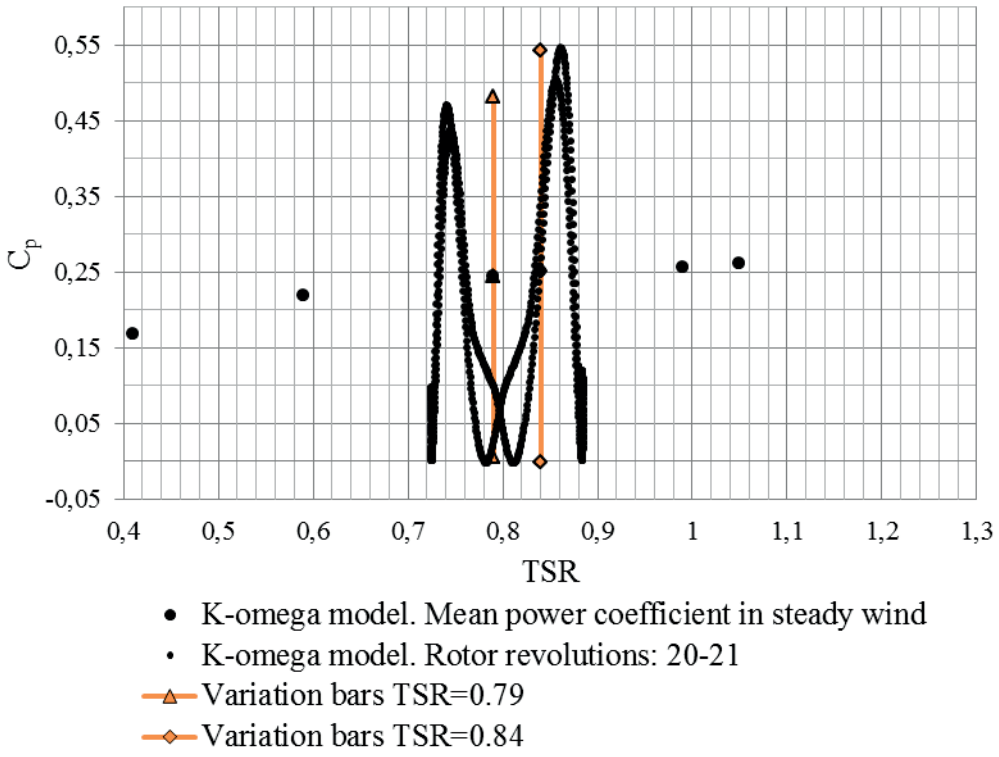

Figure 39. Power coefficients of a Savonius rotor with K_g equal to 0.24 and 0.27. Error bars denote the variation of the power coefficient during one revolution under the specified TSR under steady wind conditions.

In contrast to the observed phenomena, the range of variation of the power coefficients of the rotor operating with the gust with K_g of 0.95 and 1.08 is similar to the range of variation of the power coefficients of the rotor under steady wind conditions as show in Figures 41 and 42. When the rotor is exposed to a gust with K_g around the unity it responses in almost quasi-steady state. Due to the rigid and inertial structure of the rotor it cannot track the fast changes of the inlet velocity and, hence, the higher the gust reduced frequency the less variable the power coefficient is as a function of a TSR. As a result, the performance of the Savonius rotor is sensitive to the frequency of the gust.

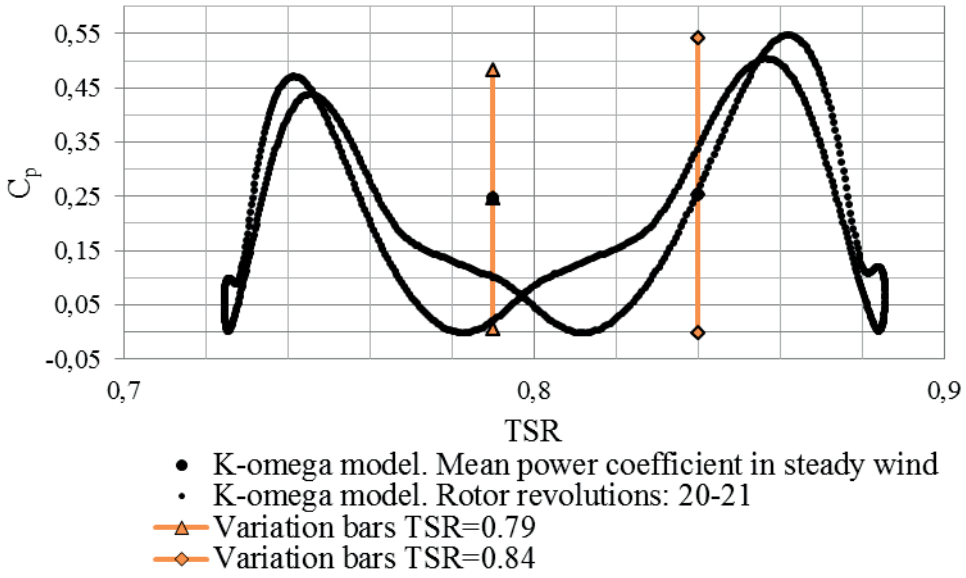

Figure 40. Power coefficients of a Savonius rotor with K_g equal to 0.24 and 0.27 and TSRs from 0.7 to 0.9. Error bars denote the variation of the power coefficient during one revolution under the specified TSR under steady wind conditions.

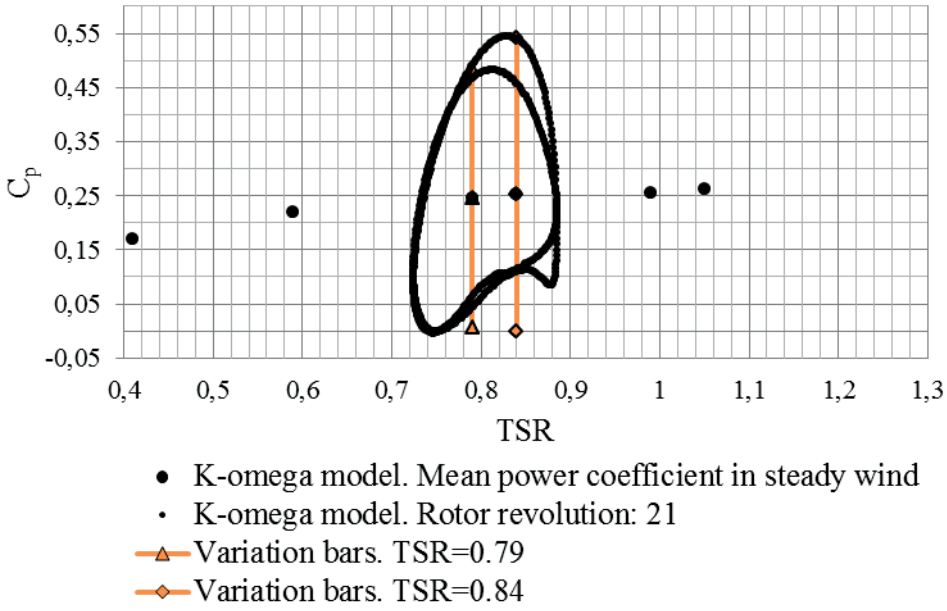

Figure 41. Power coefficients of a Savonius rotor with K_g equal to 0.95 and 1.08. Error bars denote the variation of the power coefficient during one revolution under the specified TSR under steady wind conditions.

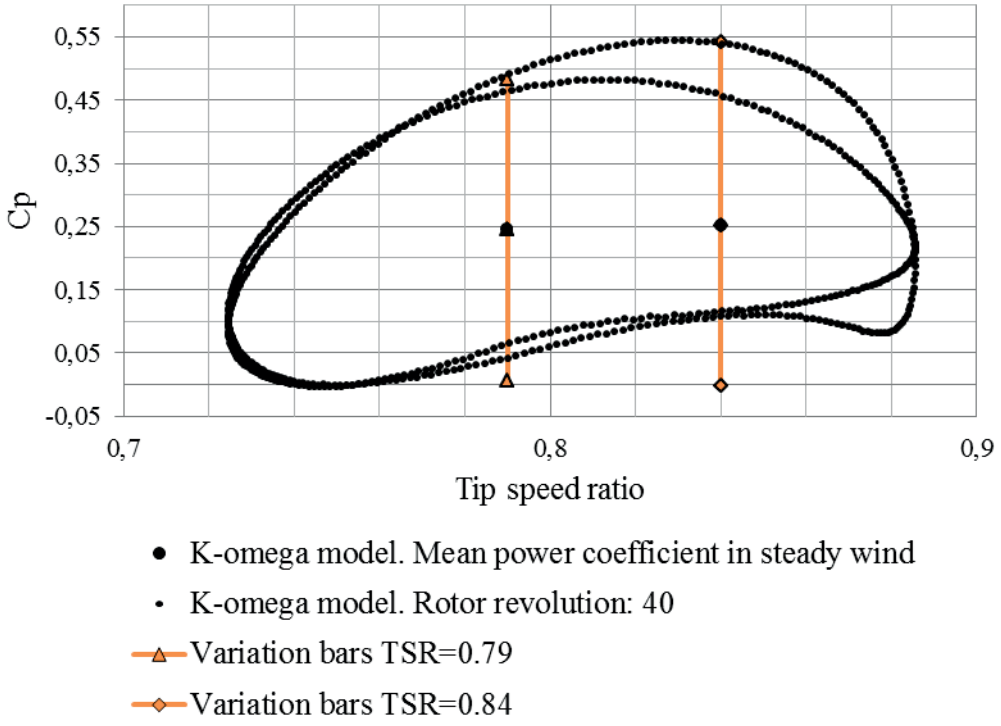

Figure 42. Power coefficients of a Savonius rotor with K_g equal to 0.95 and 1.08 and TSRs from 0.7 to 0.9. Error bars denote the variation of the power coefficient during one revolution under the specified TSR under steady wind conditions.

The averaged power coefficient under unsteady wind conditions may be calculated according to the Eq. (27):

$$C_p^{unsteady} = \overline{\sum_0^{2\pi} T_j \cdot TSR_j}, \quad (27)$$

where T_j is the rotor torque at the moment of time j and TSR_j is a tip speed ratio at the moment of time j under unsteady wind conditions.

Table 8 contains the averaged power coefficients for two sets of K_g. In Table 8 the power coefficients for steady wind conditions are obtained using numerical model (see Figure 24 on page 51). The power coefficients for steady wind conditions are considered as reference and the relative difference of the power coefficients is

$$\Delta C_p = \frac{\left| C_p^{steady} - C_p^{unsteady} \right|}{C_p^{steady}} \cdot 100\%. \quad \textbf{(28)}$$

The relative difference between the power coefficients obtained for the two angular velocities is

$$\Delta C_{p,i}^{mod} = \frac{\Delta C_p^{unsteady}}{\max_{i=1,2}\left(C_{p,i}^{unsteady} \right)}, \quad \textbf{(29)}$$

where $\Delta C_{p,i}^{mod}$ has been calculated for the two values of the ω: 6 rad/s and 24 rad/s. In Eq. (29) the subscript i addresses two sets of K_g : 0.24, 0.27 and 0.95, 1.08 (see Table 7 for more details).

Table 8. The averaged power coefficients obtained under steady and unsteady wind conditions and variability of these values.

Steady wind conditions		**Unsteady wind conditions**				
TSR	C_p^{steady}	K_g	$C_p^{unsteady}$	ΔC_p (%)	$\omega \left(\frac{rad}{sec}\right)$	ΔC_p^{mod} (%)
0.77	0.24	0.24	0.197	17.9	6	12.5
0.85	0.243	0.27	0.225	7.4		
0.77	0.24	0.95	0.219	8.8	24	0.45
0.85	0.243	1.08	0.22	9.8		

The data in Table 8 illustrate that with higher gust reduced frequencies the power coefficient approaches the values it takes under steady wind conditions for the rotor does not response quickly enough to the gust fluctuations.

Generally, these observations are common for VAWTs. (Scheurich et al. 2013) The configuration and type of a rotor has an influence on the scale of such a variation. In this study, only the influence of the gust reduced frequency is studied, while the sensitivity of a rotor to the amplitude of the sine function could also be studied.

Conclusions of a Savonius rotor modelling under unsteady wind conditions

A Savonius turbine under unsteady wind conditions has been analysed with the use of the model of Ansys Fluent. The k-ω SST turbulence model was chosen over the Reynolds stress turbulence model because at the validation stage it provided more accurate results under steady wind conditions. The experimental data by the Sandia laboratory was used as reference for the validation purposes. (Blackwell et al. 1977) The inlet velocity was defined as a sine function with 10% amplitude from the mean value and two values of the angular velocity: 6 rad/s and 24 rad/s.

As a result, the values of the power coefficients as a function of TSR were obtained. It was found, that similar to steady wind conditions, when the rotor operates with a TSR close to the optimal value the power coefficient tends to increase. The relative difference between the power coefficients under steady and unsteady wind conditions can be up to 17% (see Table 8 for details).

With increased K_g the Savonius rotor responded in a similar way as in quasi-steady state: the changes in the wind speed are quicker than the rotor response, and hence the power coefficient depends less in TSR. As a result, the performance of the Savonius rotor is sensitive to the frequency of a gust.

5 SPECIAL ASPECTS OF SAVONIUS WIND TURBINE IN URBAN AREAS

In this Chapter two particular issues are discussed, namely the RCS (Radar Cross Section) of a Savonius wind turbine and methods to improve wind data analysis.

The variable nature of wind resources makes the forecasting of the wind speed necessary. Generally, the forecasts of short and long time scales are distinguishable. The long-term forecasts over periods of a few hours or days can be used to plan the deployment and operating regime of other power components on the network, for example storage units and consumer power supply. Characteristics of the wind speed distribution densitu in particular, are important factors in both the design and siting of a wind turbine. The turbulence of the wind also affects the structural fatigue of the turbine components. The assessment of the wind energy potential, which represents the energy content of the wind, along with the storage capacity, decreases the dependence of the system from the variable character of generated wind energy. For these reasons the accuracy of forecasting the characteristics of the wind is of particular importance.

An initial site selection includes the wind power potential estimation at the particular site based on data over at least one year of wind speed measurements. Data can be taken from the Wind Atlases, for example European Wind Atlas published by Riso National Laboratory, if actual wind speed measurements are not available (Troen et al. 1989). The wind speed regime is characterised usually with the Weibull distribution, which represents the wind speed probability density. A number of numerical methods can be applied to the initial data to determine the coefficients of a Weibull function at a particular site. The present study investigates different approaches on how to choose the proper method to estimate various wind characteristics. The measurements of averaged wind speed over 10 minutes taken University of Vaasa are used to support and illustrate this investigation. In this study the wind power density in Vaasa is estimated and analysed.

Another important issue is the disturbance of radar operation caused by a wind turbine. The interference of a wind turbine structure in the proximity to airfields or military training areas with radar signals needs to be considered carefully. In this study the RCS of a Savonius turbine is calculated using a numerical model. The stationary three-dimensional model of a Savonius rotor is disposed under a radar signal with varying angles of attack.

5.1 Calculation of a wind speed probability density and a wind power density

The wind speed variation at a specified location is commonly described by a Weibull distribution. This function provides characteristics of the wind regime for wind energy evaluation and can be obtained with the use of various methods applied to the wind speed data. Furthermore, the observed values are used to validate the obtained Weibull functions.

The commonly used parameters for such comparison are the accuracy of calculation of a wind speed probability density and a total wind power output. However, Celik et al. (2003) estimated also the accuracy of the obtained distributions of a wind speed probability density and a wind power density in order to give a complete assessment of applied methods. However, these functions are unable to take into account the type of the discrepancy such as overestimation or underestimation. It is shown in this study, that a number of serial overestimating or underestimating values can cause errors in the total value.

An annual wind power density is one of the characteristics of a wind power potential at a certain location. Seguro et al. (2000) used a power curve of a particular wind turbine along with the obtained Weibull distribution to calculate the expected wind energy output. However, this approach is expected to limit the generalization of the study. The energy output depends on the choice of a particular wind turbine. It is for this reason that in this study a wind power density distribution is chosen as one of the criteria.

In this study the parameters of the Weibull distribution function are obtained by the use of four statistical methods. These parameters are then used to calculate a number of characteristics of wind resources and wind speed regime. In order to determine the suitability of each studied method, the following three parameters were used: the root mean square (RMS) error of the wind speed probability density, the RMS error of the wind power density and the error in the total wind power density. These three parameters are expected to contain the comprehensive statistical information about the wind power potential and wind speed regime at a particular site.

The current study shows that a number of various criteria must be considered in order to choose the best method to model the wind regime at a particular site. The lowest error of the wind speed probability density calculation does not relate necessarily to the lowest error in the wind power density modelling. In turn, a

good correlation between the modelled and reference wind power densities does not principally mean the same correlation of the annual wind power density.

One of the goals of this part of the research is to show that the accuracy of the applied methods depends on the data which is to be predicted. Another aim of this study is to estimate the wind power potential in a particular region with the use of various statistical methods. With these two objectives, the estimation of the wind power potential is done by means of the annual wind power density modelling. Hence, the final judgment about the ability of each method to predict the wind power potential is done based on the accuracy of the annual wind power density calculation.

Analysis of the wind data

The measurements of 10 minutes averaged wind speed have been conducted during the following five years (2007–2010, 2013) at the University of Vaasa. A 3-cup anemometer was mounted on the roof of the Tritonia library building at a height of 30 meters above the ground level. The building is located on the sea shore. The 10 minutes averaged data of the one second measurements were collected for each month except July of 2013.

The mean yearly averaged wind speeds vary from 3.42 m/s to 4.25 m/s within five years, with 2.40 m/s and 5.55 m/s as minimum and maximum monthly averaged values. The general trends are windy winter and autumn seasons with high standard deviations from the mean wind speed. Such values of wind speed are good since the weather station is located in an urban area.

Mathematical models

The Weibull distribution is commonly used in ingeneering to study the wind characteristics. It has been claimed that the Weibull two-parameter model is suitable for a wide collection of wind speed data (Weisser 2003, Justus et al. 1977). However, the Weibull distribution function may not fit the observed data with wind speed values close to 0 m/s as shown by Ignatiev (Ignatiev 2013).

The probability density function is expressed mathematically as

(30) $$f(v) = \frac{k}{c}\left(\frac{v}{c}\right)^{k-1} \exp\left[-\left(\frac{v}{c}\right)^{k}\right],$$

where f(v) is the wind speed probability density, v (m/s) is wind speed, k and c (m/s) are the scale and shape parameters, respectively. (Emeis 2013)

The shape and scale parameters are determined based on the observed wind speed data and with the use of four methods in this study. The histogram of the wind speed probability density obtained using the observed data can be represented as a continuous function f(v) obtained using the shape and scale parameters.

The moment method and approximated moment method

The mean wind speed and standard deviation of the wind speed are related with the Weibull distribution parameters as follows:

(31) $$\overline{v} = c \cdot \Gamma\left(1+\frac{1}{k}\right)$$

(32) $$\left(\frac{\sigma}{\overline{v}}\right)^2 = \frac{\Gamma\left(1+\frac{2}{k}\right)}{\Gamma^2\left(1+\frac{1}{k}\right)} - 1,$$

where σ is the standard deviation of the wind speed and Γ is the Gamma function. (Emeis 2013)

The moment method (MM) uses an iterative process to solve Eq. (32) and to calculate the shape parameter k. The approximated moment method (MMA) uses an approximated coefficient instead of applying the iterative process. (Emeis 2013)

(33) $$k = \left(\frac{\sigma}{\overline{v}}\right)^{-1.086}.$$

Despite the simplicity of Eq. (33) the approximated method shows good results. The scale parameter c is calculated from Eq. (31).

The modified maximum likelihood method

Another iterative method is the modified maximum likelihood method (MMLM). The scale and shape parameters of the Weibull distribution are determined by the use of the Eq. 34 and 35. (Seguro et al. 2000)

$$\mathbf{(34)} \qquad k = \left[\frac{\sum_{i=1}^{n} v_i^k \cdot \ln(v_i) \cdot P(v_i)}{\sum_{i=1}^{n} v_i^k \cdot P(v_i)} - \frac{\sum_{i=1}^{n} \ln(v_i) \cdot P(v_i)}{P(v>0)} \right]^{-1}$$

$$\mathbf{(35)} \qquad c = \left[\frac{\sum_{i=1}^{n} v_i^k \cdot P(v_i)}{P(v>0)} \right]^{\frac{1}{k}}$$

In Eq. (34) and Eq. (35) $P(v_i)$ is the probability that the wind speed values appear within the bin i and $P(v>0)$ is the probability of non-zero wind speeds. It should be noted, that the argument of the logarithmic functions, namely $(v_i)\cdot P(v_i)$, in Eq. (34) cannot become zero since the minimum average wind speed of the first bin is far from 0^+ value.

The power density method

Recently, a new method of calculation of the Weibull function parameters was proposed by Akdag and Dinler (Akdag et al. 2009). It is called the energy pattern method or the power density method (PDM). This method uses mean wind speed and power density, if they are available. If the data is represented in the time series format it can be transformed into the energy pattern factor E_{pf} as follows:

$$\mathbf{(36)} \qquad \frac{\overline{v^3}}{(\overline{v})^3} = \frac{\Gamma\left(1+\frac{3}{k}\right)}{\Gamma\left(1+\frac{1}{k}\right)^3} = E_{pf},$$

where $\overline{v^3}$ is the averaged cube of the wind speed and $(\overline{v})^3$ is the mean wind speed to the power of three. In this study Eq. (36) is solved iteratively, while the scale parameter can be found from Eq. (37).

$$\mathbf{(37)} \qquad k = 1 + \frac{3.69}{E_{pf}^2}.$$

The advantage of the power density method is the simplicity of calculation of the particular characteristics. It does not require binning the wind speed data. However, the modelled wind speed probability density cannot be compared with

the observed distribution because this method does not require such data analysis. Hence, the observed wind speed probability density should be obtained additionally for comparison purposes. Nonetheless, it is less computationally demanding to build the observed wind speed probability density in order to validate the obtained model than to use this distribution to determine the model parameters.

This distribution is available already for this research, which was necessary for the rest of the methods. Hence, it is possible to include the results of the PDM in the final table and perform the comparison of the methods.

Table 9 contains the shape and scale parameters of the Weibull function calculated for year 2008 as an example of the wind speed distribution. It should be noted, that the shape and scale parameters for all four methods do not vary drastically within a month.

Based on the shape and scale parameters obtained by each method, the Weibull distribution functions are determined by the use of Eq. (30) along with a number of wind speed characteristics. As long as one of the aims of this work is to estimate the wind power potential the most interesting among these characteristics is the wind power density.

The wind power density shows the theoretically available wind power per square meter of the rotor swept area with the particular wind speed distribution. This characteristic is essential for the wind power potential estimation. Hence, it is important that the applied methods are able to predict the wind power density correctly.

The wind power density can be described with the use of wind speed probability density function or Weibull function parameters

(38) $$P = \frac{1}{2} \cdot \rho \sum_{i=1}^{n} v_i^3 \cdot f(v_i)$$

and

(39) $$P = \frac{1}{2} c^3 \cdot \rho \cdot \Gamma\left(1 + \frac{3}{k}\right).$$

It should be noted that Eq. (39) allows for calculating the average wind power density for the selected period of time, but not the contribution of each wind

speed bin to the total value. For this reason Eq. (38) is applied to the wind speed frequencies obtained by the methods under investigation.

Table 9. The Weibull distribution parameters calculated by various methods based on the measurements of year 2008.

Month	Observed data		MMA		MM		MMLM		PDM	
	$\bar{v}(m/s)$	σ	k	c (m/s)	k	c (m/s)	k	c (m/s)	k	c (m/s)
January	4.91	2.22	2.37	5.54	2.35	5.54	2.35	5.62	2.36	5.54
February	4.42	3.02	1.51	4.90	1.49	4.89	1.56	5.09	1.52	4.90
March	3.9	1.15	3.75	4.31	3.77	4.31	3.87	4.34	3.31	4.34
April	2.66	1.55	1.80	2.99	1.78	2.99	1.81	3.19	1.80	2.99
May	3.56	2.02	1.85	4.01	1.83	4.01	1.85	4.11	1.84	4.01
June	3.25	2.06	1.64	3.63	1.62	3.63	1.65	3.81	1.65	3.63
July	3.7	2.01	1.94	4.17	1.92	4.17	2.01	4.32	1.96	4.17
August	3.39	2.07	1.71	3.80	1.68	3.80	1.79	4.00	1.68	3.80
September	3.31	2.76	1.22	3.54	1.21	3.53	1.31	3.86	1.23	3.55
October	5.55	3.2	1.82	6.24	1.79	6.24	1.85	6.48	1.84	6.24
November	4.85	2.93	1.73	5.45	1.71	5.44	1.76	5.62	1.74	5.45
December	4.31	2.8	1.60	4.81	1.58	4.81	1.67	5.09	1.59	4.81

Results

In order to choose the best method to model the real wind speed regime, the various modelled characteristics have to be compared with the empirically obtained. The observed values are called the reference values. The annual wind power density and distributions of wind speed probability density and wind power density were chosen for this comparison. The RMS error calculated with the Eq. (40) is used to estimate the discrepancy between the modelled and the reference wind speed frequencies and power densities. In other words the RMS error shows the deviation between modelled and reference data

$$\textbf{(40)} \qquad \text{RMS error} = \sqrt{\frac{\sum_{i=1}^{n} \left(f(v_i)_{mod} - f(v_i)_{data}\right)^2}{n}}\,,$$

where $f(v_i)_{mod}$ and $f(v_i)_{data}$ are modelled and reference wind speed distribution densities, and n is the number of the wind speed bins. The same approach is used when the RMS error of the power densities is determined.

Wind speed probability density and power density

Tables 10 and 11 show the RMS errors of the wind speed distribution densities and the wind power densities, respectively, for year 2008. Within each month the RMS errors of the various applied methods are of the same order of magnitude. The lowest RMS error of the wind speed probability density and hence the best correlation with the reference data was obtained with the MMLM. However, analysis of the RMS error of the power density in Table 11 reveals that data obtained with the use of the MM are more closely correlated with the reference values.

The reason for this is that the multiplication by the cube of the wind speed (see Eq. (38)) amplifies the error of wind speed distribution densities with high wind speed values and high distribution densities. The previously calculated RMS error of the wind speed probability density applies equal weight to the error from each wind speed bin. A smaller error in probability density of wind of high speed and probability density has a more remarked influence on the final power density error than a bigger error in low speed and probability density winds. In other words, the higher the wind speed and probability density the more weight is added to the wind power density error from the wind speed bin.

This phenomenon is observed in June of 2007: the RMS error of the power density is the biggest for the MMLM (40.12 W/m²), while for the PDM this value is 40.07 W/m². However, the RMS error of the wind speed probability density is lower for the MMLM compared to the PDM (0.2705 and 0.2723 respectively).

In Figure 43 it is shown that the error in the wind speed probability density of the PDM is largely due to the first peak of about 1.5 m/s. However, this wind speed bin does not contribute to the final power density as much as other wind speed bins. This explains why the error in the power density for June of 2007 is less than it could be expected based on the wind speed probability density error.

Table 10. The RMS error of the wind speed probability density obtained with the use of various methods based on the measurements of year 2008.

Month	RMS error of the wind speed probability density			
2008	**MMA**	**MM**	**MMLM**	**PDM**
January	0.0209	0.0210	0.0209	0.0209
February	0.0186	0.0184	0.0194	0.0187
March	0.0492	0.0487	0.0456	0.0607
April	0.0469	0.0465	0.0431	0.0468
May	0.0248	0.0248	0.0236	0.0248
June	0.0298	0.0294	0.0282	0.0301
July	0.0299	0.0300	0.0282	0.0299
August	0.0316	0.0317	0.0304	0.0305
September	0.0189	0.0193	0.0185	0.0185
October	0.0190	0.0190	0.0189	0.0191
November	0.0255	0.0256	0.0251	0.0255
December	0.0302	0.0301	0.0299	0.0302
Total	0.3453	0.3444	0.3319	0.3557

Table 11. The RMS error of the wind power density of each month based on the measurements of year 2008.

Month	**RMS error of the power density(W/m^2)**			
2008	**MMA**	**MM**	**MMLM**	**PDM**
January	3.54	3.55	3.57	3.54
February	3.71	3.74	3.51	3.71
March	2.52	2.47	2.39	4.43
April	0.92	0.96	1.33	0.93
May	0.88	0.93	1.09	0.89
June	1.50	1.52	1.60	1.43
July	1.21	1.24	1.26	1.21
August	1.64	1.63	1.89	1.63
September	2.92	2.87	2.95	2.97
October	4.38	4.35	4.19	4.41
November	2.77	2.71	2.68	2.79
December	3.52	3.53	3.77	3.53
Total	29.51	29.49	30.23	31.47

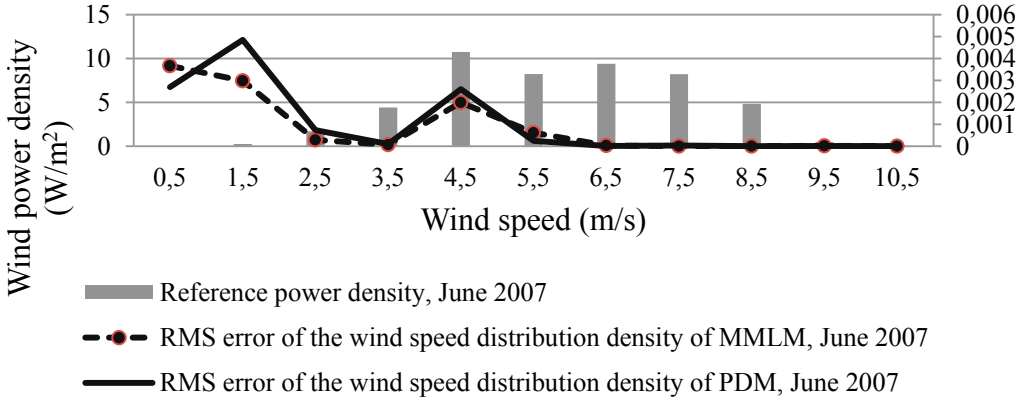

Figure 43. Distributions of the observed wind power density values and errors of the wind speed probability density by the MMLM and PDM.

RMS error of power density and total power density

The RMS error does not take into account the direction of the discrepancy. Whether the values are overestimated or underestimated might have an effect on the total values of the modeled data.

In this connection it is interesting to compare the obtained results based on the RMS errors of the wind power density and the annual power density. In addition, from the wind energy implementation view point the more important data is the annual power density. For this reason the choice of a proper statistical method is based on the error of the annual power density obtained from Eq. (41).

$$\mathbf{(41)} \qquad P_{error} = \frac{\left|P_{ref} - P_{mod}\right|}{P_{ref}} 100\% ,$$

where P_{ref} and P_{mod} are annual reference and modelled power density values respectively.

Despite the good correlation with the reference values, an aggregated errors to the same side (the value underestimation or overestimation) could lead to the significant errors in the overall values. If the data generated by the method contain points above and below the reference values these errors could compensate each other. This is illustrated by the results of year 2008 in the Table 11.

The values of the wind power density obtained for year 2008 by the MMLM are closely correlated with the reference: the RMS error of the wind power density is

30.23 W/m² for the MMLM and 31.47 W/m² for the PDM. However, during eleven months the wind power density values were oversetimated by the MMLM which leads to an oversetimated annual wind power density. In contrast, the data from the PDM, which showed higher deviation from the observed wind power densities, exceeded the reference values only during four months. Finally it caused a lower error in the total wind power density: 2.99% for PDM and 4.9% for MMLM (see Table 11). The same phenomenon is observed for year 2013.

It should be noted that the RMS error is still a very important criterion. With the low deviation even long-term overestimations or underestimations could yield better results than combined overestimations and underestimations with high deviations. For instance, the MM applied to the data of year 2007 shows the best correlation with the reference power density. Due to the close correlation the total wind power density is the closest to the reference value despite the fact that during the eleven months the values were underestimated (see Table 13).

The same analysis was done for the measurements taken during other years. Table 12 contains the best methods to fulfill various judgment criteria.

Table 12. The statistical methods with the lowest errors based on various comparison parameters.

Year	RMS error wind speed probability density	RMS error Power density	Error Total power density
2007	MM	MM	MM
2008	MMLM	MM	MM
2009	MMLM	MM	MM
2010	MM	MM	MM
2013	MMLM	MMLM	MM

Table 13. The wind power density and the RMS error of the power density of each month based on the measurements of year 2007.

Month	**Power density (W/m^2)**					**RMS error of the power density (W/m^2)**			
2008	Observed	MMA	MM	MMLM	PDM	MMA	MM	MMLM	PDM
January	167.5	159.0	160.6	175.4	158.8	4.12	4.07	4.00	4.13
February	65.9	63.3	64.0	74.3	62.6	1.60	1.61	1.76	1.60
March	63.3	60.8	61.9	72.3	60.4	1.59	1.58	1.83	2.41
April	222.5	216.2	218.4	227.7	217.8	3.17	3.10	3.07	3.12
May	212.2	199.7	202.0	207.6	204.8	5.20	5.12	5.24	5.04
June	48.3	47.7	48.0	52.9	47.4	1.19	1.21	1.34	1.18
July	72.2	55.5	56.3	56.4	50.6	6.26	6.29	6.21	6.17
August	94.5	88.9	90.1	99.4	89.2	1.38	1.30	1.49	1.36
September	132.3	132.7	134.4	140.9	132.7	3.77	3.80	3.78	3.77
October	115.2	112.6	114.1	124.7	112.1	2.70	2.68	2.72	2.72
November	100.3	98.6	100.0	108.2	99.5	2.36	2.39	2.58	2.38
December	171.5	163.7	165.2	209.9	153.1	5.45	5.41	6.10	6.20
Total	1465.5	1398.8	1415.2	1549.7	1389.0	38.81	38.57	40.12	40.07
P_{error} (%)		4.55	3.43	5.75	5.22				

Discussion and conclusions of wind power potential estimation

A statistical analysis was performed on the wind speed data measured at the University of Vaasa. The Weibull distribution parameters were calculated with four different methods. In order to evaluate the ability of the applied methods to model the wind regime, three magnitudes were considered: the RMS error of the wind speed probability density, the RMS error of the wind power density and error of the annual wind power density. The observed data of four years were used as a reference to evaluate the accuracy of each method in determining the Weibull function.

It was shown that in order to evaluate the performance of applied methods it is necessary to estimate the discrepancy of the wind speed parameters from the reference ones along with the accuracy of the integrated values. The low RMS error of wind power density does not necessarily mean a low error of annual wind power density, due to a possibly occurred number of serial underestimation or overestimation of the reference values.

It has been stated that the RMS errors of the wind speed probability density does not necessarily imply good results in wind power density modelling. The calculation of the power density involves the cube of the wind speed which leads

to the rearranging of its error. In other words, the higher the wind speed and probability density the more weight is added to the wind power density error from this particular wind speed bin.

The wind power potential in Vaasa was calculated by means of the wind power density. Based on the annual wind power density the best results are obtained by the Moment Method for all five years of measurements.

It is worth mentioning, that despite the fact that the modern Power Density Method does not provide the most accurate data in comparison to other considered methods, it could still be applied. The errors of this method are generally in the same range of errors as in other methods and do not differ drastically. The simplicity of the method in some particular cases can overcome the listed errors.

Table 14 contains the wind power density values calculated based on the observed data averaged over 10 minutes and the statistical method with the best correlation with the reference values.

Table 14. The wind power density (W/m^2) of each month based on the measurements of all years and MM.

	Year									
	2007		2008		2009		2010		2013	
Month	**Ref.**	**MM**	**Ref.**	**MM**	**Ref.**	**MM**	**Ref.**	**MM**	**Ref.**	**MM**
January	167.5	160.6	116.0	118.0	112.1	102.3	58.2	58.2	67.2	65.5
February	65.9	64.0	137.0	132.4	64.7	61.9	37.3	35.3	95.1	94.2
March	63.3	61.9	44.5	45.1	72.5	71.7	91.2	81.4	54.7	56.1
April	222.5	218.4	23.9	24.3	57.3	56.5	45.5	45.0	136.6	134.0
May	212.2	202.0	56.3	57.2	116.4	112.8	51.3	49.9	69.1	66.9
June	48.3	48.0	48.3	47.7	63.5	61.8	74.2	74.9	82.2	82.2
July	72.2	56.3	59.0	59.3	42.4	42.5	100.3	93.4	-	-
August	94.5	90.1	54.1	53.8	54.2	53.9	46.8	44.3	57.6	58.8
September	132.3	134.4	86.6	78.7	177.6	180.4	48.3	48.0	50.3	52.1
October	115.2	114.1	214.4	206.8	48.3	47.4	112.1	113.9	143.5	145.4
November	100.3	100.0	152.4	147.8	86.8	87.6	53.9	51.2	244.2	230.5
December	171.5	165.2	120.4	119.5	50.1	49.4	43.8	40.6	159.8	158.9
Total	1465.5	1415.2	1112.9	1090.6	945.9	928.1	762.8	736.1	1160.3	1144.5

5.2 Estimation of RCS of Savonius wind turbine

With the development of wind energy technology onshore sites becomes more attractive for wind turbine installation. Often turbines are located at close proximity of transmission and reception facilities such as radar, radio, television,

installations of global positioning systems (GPS) and wireless networks. Particularly this issue arises in the urban areas where the concentration of such connections is higher than in the open fields of rural areas. Wind farms and even individual small-scale wind turbines can have a considerable effect on the received signals by the mentioned facilities. As wind energy technology continues to develop, the physical size of the turbines increases, causing more intensive interferences to radars. Wind turbines have a considerable potential to reduce visibility of targets for radars within the vicinity of a wind farm, such as marine, defence and air traffic radars.

Several studies have been done on the interaction between HAWTs and different types of radar, based on both experimental data (Kent et al. 2008) and simulations (Lok et al. 2011, Ohs et al. 2010, Pinto et al. 2010, Jenn et al. 2012). It has been shown that the level of interaction between a wind turbine and radar depends on the shape and dimensions of a wind turbine and the radar's signal characteristics. A rotating frequency of the moving parts of a turbine contributes to the total radar interference as well. To the best of the authors' knowledge, there are no similar studies related to a Savonius wind turbine.

In this study the interaction between radar and an S-shaped Savonius wind turbine is analysed. The three-dimensional numerical model of the Savonius rotor is built using Comsol Multiphysics®4.3a. An interaction between the S-shaped Savonius rotor and the radar is evaluated using the RCS value.

The RCS

The radar's operational principle is based on the analysis of the emitted and received electromagnetic waves. Two factors are considered when estimating the influence of the target on a radar system performance: the RCS and the Doppler shift effect.

The RCS is defined as the limit of the ratio of the dissipated signal by the target in a given direction to the incident signal, when the distance from the scatterer to the point of measurement of the scattered power approaches infinity (Knott et al. 2004). The RCS is a measure of the target's ability to reflect radar signals back to the receiver. Radars are referred to as monostatic and bistatic, depending on a relative position of a transmitter and a receiver. A monostatic radar transmits and receives the signal whereas a bistatic radar uses one radar to transmit the signal and a second radar to receive the signal. The monostatic radar is considered in this research, since the majority of current operating systems are monostatic.

Radar interactions with HAWTs has been more frequently reported in the literature since this type of wind turbine is much more widely used than VAWTs, such as a Savonius wind turbine. Some aspects of HAWTs interaction with radar are reported in Appendix 2.

Interaction of a Savonius turbine with radar

Typically the height and diameter of a Savonius rotor vary from 0.5 m to 4 m and from 0.3 m to 1 m respectively. In this study an S-shaped Savonius rotor with a height of 4 m and an outside diameter of 1 m is considered. The largest values of a rotor diameter and height have been chosen in order to obtain the largest values of RCS. An S-shaped Savonius turbine without base or tower is studied. If it is mounted onto a tower, the tower should also be considered when determining the turbine RCS. The maximum rated power output of the Savonius turbine with twisted blades of height 4 m and diameter 1 m is 1.6 kW. (Windside, 2015)

Verification of the numerical model of the Savonius rotor

The three-dimensional numerical model of the S-shaped Savonius rotor in a steady state is created using Comsol Multiphysics®4.3a. The stationary three-dimensional model of the Savonius turbine is exposed under the radar signal with varying angles of attack. This approach is artificial to some extent, since it is the radar which is stationary the turbine which rotates. Nontheless, this simplification does not change the physical principle of interaction of an object with a signal. The interaction between the model of the S-shaped Savonius turbine and the monostatic radar is evaluated in terms of the RCS. The top view of the 2D model of the studied S-shaped Savonius rotor is shown in Figure 43. The material chosen for the rotor model is aluminium. The blade material can be fiber glass as well. (Windside 2015) A choice of a rotor material is expected to affect a RCS by the reflective characteristics of a particular material.

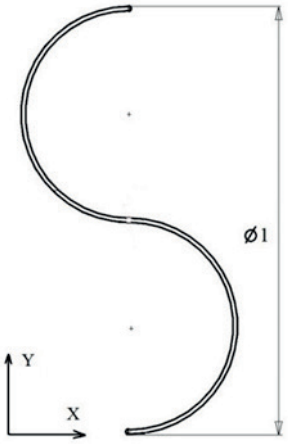

Figure 44. Top view of the S-shaped Savonius rotor. Dimensions are in meters.

The computational domain consists of three parts: the rotor itself, a spherical far-field domain with the radius of 3 m and an outer spherical layer. The electric field is calculated in the far-field domain. The outer layer has a thickness of 1 m and is referred to as a perfectly matched layer (PML). The PML covers the far-field domain around the model to minimize unphysical reflections of scattered waves when they leave the far-field domain. A perfect electric conductor (PEC) boundary condition was applied to the turbine surface. PEC acts as a perfect reflector and so does not allow any transmission through the material.

The majority of aviation and marine radars are considered to operate over two frequency values: 3 GHz and 10 GHz. As the frequency increases, the RCS of a turbine tends to increase as well. High signal frequencies are computationally demanding for simulation because finer must be the mesh would be required: at least five mesh elements per wavelength should be built (Comsol 2012). The signal frequency of 100 MHz is chosen in order to satisfy the condition of a maximum mesh element size. The mesh consists of 41 000 elements.

It is assumed that the targeted turbine is located far enough from the radar to consider the radar wave planar. In practice, this approximation can be accepted (Pinto et al. 2010).

An angular coordinate α is used to denote the direction of the radar signal in such a way that signals coming from the positive x coordinate and propagating in the negative x coordinate correspond to the $\alpha=0^{o}$ angle of incidence. The angle of incidence between the radar wave and the rotor model is shown in Figure 45. In this study the angle of incidence varied in the range from 0^{o} to 360^{o} with the step size of 1^{o}.

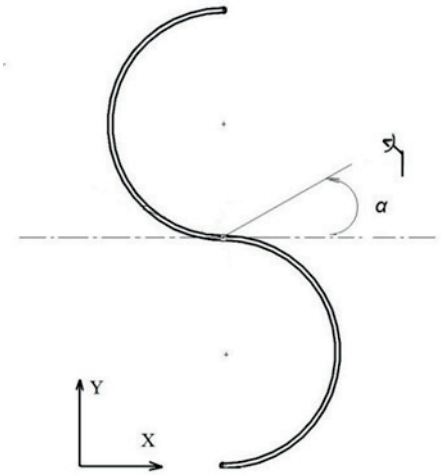

Figure 45. The angle of incidence between the rotor model and the radar waves.

The interaction between the turbine and radar is defined in terms of the relative electric field. This relative electric field illustrates the changes in the initial field, caused by the turbine presence and the RCS is measured at the angle of incidence of the incoming wave as follows:

(42) $$\sigma\left(m^2\right)=\lim_{R\to\infty} 4\pi R^2 \frac{\left|E_{rel}^2\right|}{\left|E_b^2\right|}$$

and

(43) $$\sigma(\mathrm{dBsm})=10\log_{10}\left[\sigma\left(m^2\right)\right],$$

where R is the radius of the sphere bounding the computational domain, E_{rel} is the relative field and E_b is the background field. (Comsol 2012) The abbreviation dBsm denotes dB per square meter.

Results and discussion

The RCSs of the S-shaped Savonius wind turbine were obtained for an angle of incidence from 0° to 360°. The values of RCS vary from 9.3 dBsm to 15.5 dBsm. The symmetrical shape of the rotor results into the symmetrical RCS graph, as shown in Figure 46. In Figure 46 angles of incidence correspond to the rotor location according to Figure 45.

The analysed in previous chapters addition of the gap flow guide is not expected to affect the obtained values of a RCS. The reason is that the gap flow guide does not change the outer shape of a rotor and it does not create gaps to let a signal pass.

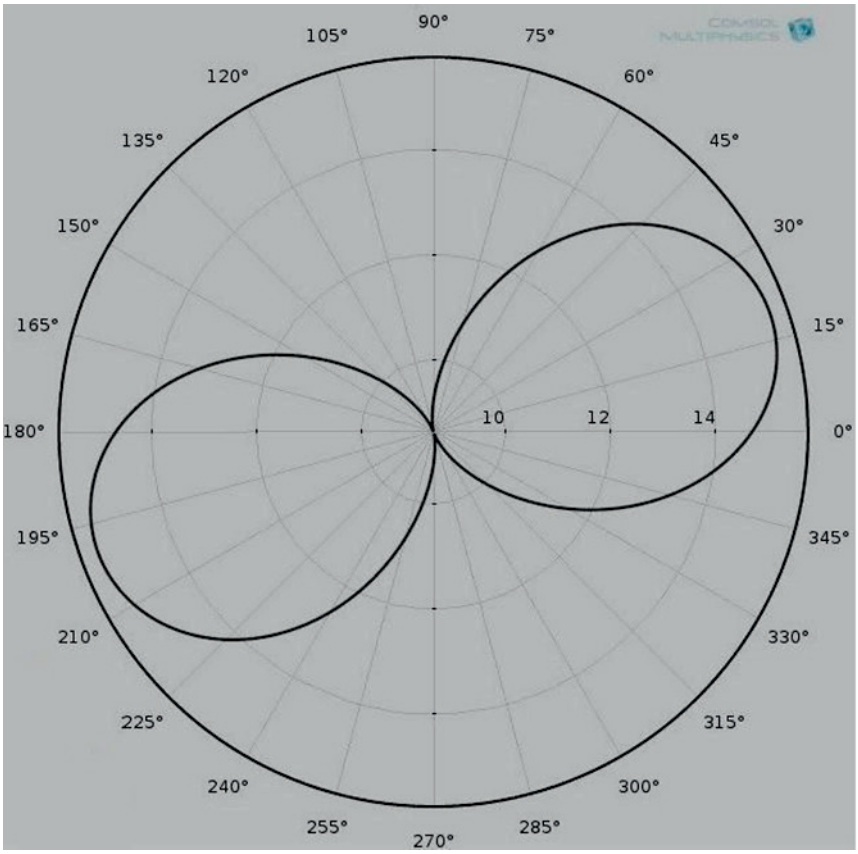

Figure 46. The values of RCS of the S-shaped Savonius rotor as a function of the angle of incidence of the radar wave.

The RCS reaches maximum values at the angle of incidence of 20° and 200°. At these angles the largest surface of the blades is perpendicular to the signal. Hence, a larger share of the waves is reflected back to the radar. Meanwhile, for angles of 90° and 270° the reflecting surface of the turbine blades is the lowest.

The disturbance of a radar operation by a wind turbine is to be considered when the wind turbine installation is planned in urban areas. In this part of the research, the interaction between the S-shaped Savonius turbine and the radar is studied. In short, the following aspects of wind turbine and radar interaction are found to be of particular importance.

(i) Static parts of the turbine.

HAWT: the turbine tower typically causes the biggest share of the total RCS with the averaged value of about 75%. (Pinto et al. 2009)

Savonius turbine: two separate cases should be considered: whether the turbine is installed on an existing building or the turbine under project needs to have its own tower. In the first case the RCS of the building is already known. In the second case the RCS of the base of the Savonius turbine is to be evaluated. The chosen base can have a strong influence on radar interference. However, in comparison to the towers of large-scale HAWTs, the towers of the Savonius turbines have smaller dimensions as at present.

(ii) Moving parts of the turbine.

HAWT. The blades cause a minor contribution to the total RCS (up to 15%) and a major contribution to the value of the Doppler frequency. The turbine nacelle (which contains the mechanical and electrical equipment for power generation) has the least impact on the total RCS compared to the tower and blades.

Savonius turbine. The Doppler frequency of a Savonius rotor must be studied additionally.

(iii) The variability of the turbine shape due to the blades rotation.

HAWT. The RCS fluctuates from an average value when the direction of propagation of the radar signal is in parallel with the nacelle long axis. The Doppler frequency reaches the maximum value when the blades rotate towards and away from the direction of propagation of the radar signal and one of the blades is perpendicular to this direction.

Savonius turbine. Because of the geometry of the turbine, the radar interference varies depending on the angle of incidence of the signal. The RCS attains the maximum value when the direction of propagation of the radar signal is perpendicular to the flat plane of the turbine (zy plane in Figures 45 and 46) and the minimum value when it is parallel to this plane.

Conclusion of the RCS study

In this study the interactions between the S-shaped Savonius wind turbine and the radar of signal frequency 10 MHz was modelled using Comsol Multiphysics®4.3a. The RCS of the Savonius wind turbine was calculated. It was shown that a Savonius rotor can cause considerable influence on the ability of the radar to detect targets in the vicinity of the wind turbine. Hence, these interactions should be carefully considered when a Savonius turbine is installed.

An accurate calculation of the Doppler frequency caused by a Savonius wind turbine could be considered for any future studies. In addition, an influence of a rotor configuration and types of tower on radar interference could be studied.

6 SUMMARY

This chapter presents the conclusions and answers to the research questions. The main results of the thesis are presented it Section 6.1. Section 6.2 contains the contributions of the thesis. Proposals for future studies are discussed in Section 6.3.

6.1 Main findings of the thesis

Utilization of wind energy in urban areas has become a hot topic recently in the frame of exploitation of renewable energy. The wind turbines, installed in the urban areas have to be, among other requirements, compact, environmentally friendly, able to deal with gusty winds and the noise of the turbine must be as low as specified in the technical standards. A Savonius wind turbine meets these requirements.

The answers to the research questions posed in the introduction of the thesis are discussed below.

The first two research questions. *How to obtain the wind speed probability density and wind power density using measurements of 10 minutes averaged wind speed? How to estimate the RCS of Savonius wind turbine and how to model the response of a Savonius wind turbine under unsteady wind conditions using CFD analysis?*

The thesis details the analysis of a Savonius wind turbine operation under unsteady wind conditions, the interaction of a Savonius rotor with radar and estimation of wind speed frequency and wind power density using measurements of 10 minutes averaged wind speed.

The unsteady inlet wind conditions were applied in the model of Ansys Fluent with the incoming wind speed defined as a sine function and two sets of gust reduced frequency values: 0.24, 0.27; and 0.95, 1.08. It was found that, similarly to steady wind conditions, when the rotor operates with TSRs close to the optimal, the power coefficient tends to increase. The relative difference between the power coefficients under steady and unsteady wind conditions can be up to 17% (see Table 8 for details).

With the increased values of the gust reduced frequency the Savonius rotor responded in the same way as the rotor in quasi-steady state. Due to the rigid

structure and inertia of a rotor it cannot response quickly to fast changes of the incoming wind speed. Thus the higher the gust reduced frequency the less the power coefficient depends on the TSR. The operation of the Savonius rotor is sensitive to the frequency of the gust.

It was found that a Savonius rotor can have a considerable influence on the radar ability to detect objects in the vicinity of the wind turbine. The RCS of the S-shaped Savonius rotor of diameter 1 m and height 4 m, interacting with a 100 MHz radar signal varies from 9.3 dBsm to 15.5 dBsm.

In this study the statistical analysis of the measured wind speed data collected at the University of Vaasa was carried out. The Weibull distribution parameters were calculated with the use of four methods. It was found that in order to evaluate the performance of the applied methods it is necessary to estimate the discrepancy of the wind speed parameters from the reference ones along with the accuracy of the integrated values.

The wind power potential in Vaasa was calculated by the use of the wind power density. Based on the annual wind power density the best results were yielded by the Moment Method for all five years of measurements.

It is worth mentioning, that despite the fact that the modern Power Density Method did not provide the most accurate data in comparison to other considered methods, it could still be used. The errors of this method are generally of the same order of magnitude as other methods and do not differ drastically. The simplicity of the method in some particular cases can overcome the listed errors.

The third research question. *How to improve the aerodynamic efficiency of a Savonius wind turbine?*

A modification of a Savonius turbine, as a lift device, allows increasing the lift force of the blades, shown by the analysis of the pressure distribution along the blade surfaces. The numerical model of the Savonius rotor with the radius of 0.93 m and the overlap ratio of 0.15 was simulated with the incoming wind speed of 7 m/s using Ansys Fluent®15.0. The numerical model was validated by comparing the obtained results with the experimental results. This comparison showed reasonably good agreement in wide range of TSRs.

As a result of the proposed gap flow guide application the aerodynamic efficiency of the rotor improves up to 2% for a wide range of the TSRs. In addition, this

modification does not eliminate or reduce the major advantages of a Savonius turbine.

The fourth research question. *How to build numerical models and choose their parameters to provide an accurate numerical solution and how to estimate and prevent errors of the numerical solution?*

Two models were verified during this study. The Savonius models with the rotor diameter values equal to 0.24 m and 1 m are studied with the Re from 62 000 to 490 000 using Comsol Multiphysics®4.3a and Ansys Fluent®15.0. The k-ω SST turbulence model is shown to be preferable over Reynolds stress turbulence model. The model of Ansys Fluent was validated by comparing the simulation results with the experimental results provided by the Sandia laboratory and Loughborough University.

The errors of the numerical solution can be minimized by choosing the appropriate turbulence model and combination of a near-wall layer model and generated mesh characteristics. For simulations characterised with flow separation regions or high pressure gradient the k-ω SST turbulence model with LRN wall function is expected to give accurate numerical solution.

Sensitivity analysis of the spatial and temporal discretization must be carried out in order to obtain a reliable solution independent on the discretization parameters. The mesh convergence can be demonstrated using two approaches: GCI and Richardson extrapolation. Both methods use numerical solutions obtained with systematically refined meshes. The CFL number establishes the ratio between the model spatial and temporal discretization and the fluid flow velocity.

6.2 Contributions of the thesis

The most important contribution of the thesis is the modification of the rotor blade by the introduction of the gap flow guide. This modification results in increase in the power coefficient of the rotor in a wide range of TSR values. In addition, it does not eliminate or reduce the main advantages of a Savonius rotor. The analysis of the pressure distribution, induced by the gap flow guide, contributes to the understanding of the main principle of a Savonius turbine operation and the importance of lift forces for this type of wind turbine.

Another useful contribution is the developed numerical model which was validated. The verification of the model might contribute to the available knowledge on CFD analysis.

This thesis contains information on the wind power potential in Vaasa. New sites with exact data on wind speed characteristics contribute to the accuracy of the wind power resources. In addition, the detailed analysis of the statistical methods and the approaches of their comparison can be useful for the future application in other statistical studies as well.

6.3 Suggestions for future work

For the future work a sensitivity analysis of the proposed rotor modification could be carried out. The length and the angle of the proposed gap flow guide relative to the blade can be varied and the resulting power coefficient values compared. In addition, the starting characteristics can be obtained.

In this thesis the power coefficient as a function of TSR is calculated for one value of the wind speed of 7 m/s. In order to obtain the turbine power as a function of the incoming wind speed more wind speed values have to be studied. Based on the available curves of the power coefficient as a function of TSR a generator can be chosen and a power curve obtained. The power curve of the turbine is useful characteristic from the system analysis view point since it allows for estimating the power generation and, hence, balancing the demand and supply within the energy system.

The accuracy of a two-dimensional model over a three-dimensional model can be studied. In the course of this thesis the validation of the two-dimensional model shows acceptable results. However, the validation of the three-dimensional numerical model might give better results.

In the frame of wind turbine installation in urban areas the wind speed as a function of a height above the roof surface can be taken into account. The rotor radius can be varied according to the wind speed variation with the distance from the roof surface.

References

a) Akwa, J.V., Alves da Silva Júnior, G. & Petry, A.P. (2012). Discussion on the verification of the overlap ratio influence on performance coefficients of a Savonius wind rotor using computational fluid dynamics. *Renewable Energy Volume 38, Issue 1*. 141–149.

b) Akwa, J.V., Vielmo, H.A. & Petry, A.P. (2012). A review on the performance of Savonius wind turbines. *Renewable and Sustainable Energy Reviews Volume 16, Issue 5*. 3054–3064.

Akdağ, S.A. & Dinler, A. (2009). A new method to estimate Weibull parameters for wind energy applications. *Energy Conversion and Management Volume 50, Issue 7*. 1761–1766.

Aldoss, T.K. & Najjar, Y. (1985). Further development of the swinging–blade Savonius rotor. *Wind engineering Volume9, Issue 3*. 165–170.

Aldos, T.K. (1984). Savonius rotor using swinging blades as an augmentation system. *Wind engineering Volume 8, Issue 4*. 214–220.

Alexander A.J. & Holownia B.P. (1978). Wind tunnel tests on a Savonius rotor. *Journal of Industrial Aerodynamics Volume 3*. 343–351.

Altan, B.D. & Atılgan, M. (2008). An experimental and numerical study on the improvement of the performance of Savonius wind rotor. *Energy Conversion and Management Volume 49, Issue 12*. 3425–3432.

Alanne, K. & Saari, A. (2006). Distributed energy generation and sustainable development. *Renewable and sustainable energy reviews Volume 10*. 539–558.

Balanis, C.A. (1989). *Advanced engineering electromagnetics*. John Wiley & sons, LTD. 602–645.

Bergeles, G. & Athanassiadis N. (1982) On the flow field around a Savonius rotor. *Wind engineering Volume 6, Issue 3*. 140–148.

Blackwell, B.F., Sheldahl, R.E. & Feltz, L.V. (1977). Wind Tunnel Performance Data for Two- and Three-bucket Savonius Rotors. *Sandia Laboratories, USA*.

Brännbacka, B. (2015). *Technical improvements of Windside wind turbine systems*. Vaasa: Tritonia library. Acta Wasaensia, 328. 16–17. Available at (last accessible at 3.12.2015):
http://www.uva.fi/materiaali/pdf/isbn_978-952-476-635-7.pdf

Buresti, G. (2012). *Elements of Fluid Dynamics*. Imperial college press. 99-105.

Burton, T., Sharpe, D., Jenkins, N. & Bossanyi, E. (2001). *Wind energy handbook*. John Wiley & Sons, Ltd. 41–51.

Bin, Y.O., Tawi, K.B. & Suprayogi Sunanto, D.T. (2010). Computer simulation studies on the effect of overlap ratio for Savonius type vertical axis marine current turbine. *IJE Transactions A: Basics Volume 23, Issue 1*. 79–88.

Callatay, C.H., Svanfeldt, C., Piskorz, W. & Rivas, S.G. (2011). Cities of tomorrow Challenges, visions, ways forward. [Cited 10.03.2011] European Commission, Directorate General for Regional Policy. Available at (last accessible at 3.12.2015):

http://ec.europa.eu/regional_policy/sv/information/publications/reports/2011/cities-of-tomorrow-challenges-visions-ways-forward

Celik, A.N. (2003). Assessing the suitability of wind speed probability distribution functions based on wind power density. *Renewable Energy Volume 28, Issue 10*. 1563–1574.

Lectures Notes by Celik, I. B. Introductory Turbulence Modeling. [Cited December 1999] West Virginia University Mechanical & Aerospace Engineering Dept. Available at (last accessible at 3.12.2015):

http://www.fem.unicamp.br/~im450/palestras%26artigos/ASME_Tubulence/cds13workbook.pdf

Chauvin, A. & Benghrib, D. (1989). Drag and lift coefficients evolution of a Savonius rotor. *Experiments in Fluids Volume 8*. 118–120.

Chang, T.P. (2011). Performance comparison of six numerical methods in estimating Weibull parameters for wind energy application. *Applied Energy Volume 88*. 272–282.

Comsol Multiphysics®4.3a User's Guide. (2012). [Cited November 2012]. Available at (last accessible at 3.12.2015):

http://nf.nci.org.au/facilities/software/COMSOL/4.3a/doc/pdf/mph/COMSOLMultiphysicsUsersGuide.pdf

Damak, A., Driss, Z. & Abid, M.S. (2013). Experimental investigation of helical Savonius rotor with a twist of 180°. *Renewable Energy Volume 52, Issue 0*. 136–142.

Dobrev, I. & Massouh, F. (2011). CFD and PIV investigation of unsteady flow through Savonius wind turbine. *Energy Procedia Volume 6, Issue 0*. 711–720.

D'Alessandro, V., Montelpare, S., Ricci, R. & Secchiaroli, A. (2010). Unsteady aerodynamics of a Savonius wind rotor: a new computational approach for the simulation of energy performance. *Energy Volume 35, Issue 8*. 3349–3363.

Danao, L., Edwards, J., Eboibi, O. & Howell, R. (2013). The performance of a vertical axis wind turbine in fluctuating wind – a numerical study. *Proceedings of the World congress on Engineering. London, UK*. 3–5 July, 2013.

Emeis, S. (2013). *Wind energy meteorology*. Springer. 167– 171.

Etayo, I., Satrustegui, A., Yabar, M., Falcone, F. & Lopez, A. (2010). Analysis of the frequency and time variation of radio signals scattered by a Wind Turbine. *Proceedings of the Fourth European Conference on Antennas and Propagation (EuCAP). Barcelona, Spain*. 12–16 April, 2010.

European Wind Energy Association. 2015 Available at (last accessible at 3.12.2015): http://www.ewea.org/publications/position-papers/

Fujisawa, N. (1996). Velocity measurements and numerical calculations of flow fields in and around Savonius rotors. *Journal of Wind Engineering and Industrial Aerodynamics Volume 59, Issue 1*. 39–50.

Fujisawa, N. (1992). On the torque mechanism of Savonius rotors. *Journal of Wind Engineering and Industrial Aerodynamics Volume 40, Issue 3*. 277–292.

Fujisawa, N. & Gotoh F. (1992). Visualization study of the flow in and around a Savonius rotor. *Experiments in Fluids Volume 12*. 407–412.

Gavalda, J., Massons, J. & Giaz, F. (1991). Drag and lift coefficient of the Savonius wind machine. *Wind engineering Volume 15, Issue 5*. 240–246.

Gauthier, E., Kinsey, T. & Dumas, G. (2013). RANS versus Scale-Adaptive Turbulence Modelling for Engineering Prediction of Oscillating-Foils Turbines. *Conference proceeding: 21th Annual Conference of the CFD Society of Canada, Sherbrooke, Canada*. 6–9 May, 2013.

Irabu, K. & Roy, J.N. (2007). Characteristics of wind power on Savonius rotor using a guide-box tunnel. *Experimental Thermal and Fluid Science Volume 32, Issue 2*. 580–586.

Ignatiev, S.G. (2013). Analysis of current methodology for determining energy characteristics of wind. *Alternative energy and ecology Volume 12*. 15–25.

Izumi, U. & Hiroshi, N. (1988). Optimum design configurations and performance of Savonius rotors. *Wind engineering volume 12, Issue 1*. 59–75.

Jaohindy, P., McTavish, S., Garde, F. & Bastide, A. (2013). An analysis of the transient forces acting on Savonius rotors with different aspect ratios. *Renewable Energy Volume 55, Issue 0*. 286–295.

Jenn, D. & Ton, C. (2012). Wind Turbine Radar Cross Section. *International Journal of Antennas and Propagation Volume 2012*. 1–14.

Justus, C.G., Hargraves, W. R., Amir, M. & Graber D. (1977). Methods for estimating wind speed frequency distributions. *Journal of Applied meteorology Volume 17*. 350–353.

Kamoji, M.A., Kedare, S.B. & Prabhu, S.V. (2008). Experimental investigations on single stage, two stage and three stage conventional Savonius rotor. *International Journal of Energy Research Volume 32, Issue 10*. 877–895.

Kamoji, M.A., Kedare, S.B. & Prabhu, S.V. (2009). Experimental investigations on single stage modified Savonius rotor. *Applied Energy Volume 86,Issue 7–8*. 1064–1073.

Kamoji, M.A., Kedare, S.B. & Prabhu, S.V. (2009). Performance tests on helical Savonius rotors. *Renewable Energy Volume 34, Issue 3*. 521–529.

Kang, C., Feng, Z. & Xuejun, M. (2010). Comparison Study of a Vertical-Axis Spiral Rotor and a Conventional Savonius Rotor. Power and Energy Engineering Conference (APPEEC), 2010 Asia–Pacific. Chengdu, China. 28–31 March, 2010.

Kacprzak, K., Liskiewicz, G. & Sobczak, K. (2013). Numerical investigation of conventional and modified Savonius wind turbines. *Renewable Energy Volume 60, Issue 0*. 578–585.

Khan, H.M. (1978). Model and prototype performance characteristics of Savonius rotor windmill. *Wind engineering Volume 2, Issue 2*. 75–85.

Knott, E.F., Shaeffer, J.F., Michael T. & Tuley. (2004). *Radar Cross Section, second edition*. SciTech Publishing. 64–78, 547–558.

Kent, B.M., Hill, K.C., Buterbaugh, A., Zelinski, G., Hawley, R., Cravens, L., Tri-Van, Vogel, C. & Coveyou, T. (2008). Dynamic Radar Cross Section and Radar Doppler Measurements of Commercial General Electric

Windmill Power Turbines Part 1: Predicted and Measured Radar Signatures. *Antennas and Propagation Magazine, IEEE, Volume 50, Issue 2*. 211–219.

Kooiman, S.J. & Tullis, S. (2010). Response of a vertical axis wind turbine to time varying conditions found within the urban environment. *Wind engineering Volume 34, Issue 4*. 389–401.

Lok, Y.F., Palevsky, A. & Wang, J. (2011). Simulation of radar signal on wind turbine. *Aerospace and Electronic Systems Magazine, IEEE, Volume 26, Issue 8*. 39–42.

Lun, I.Y.F. & Lam, J.C. (2000). A study of Weibull parameters using long-term wind observations. *Renewable Energy Volume 20, Issue 2*. 145–153.

Marmutova, S. & Vekara, T. (2015). Numerical study of the performance of Savonius rotor with gap flow guide. *Conference proceeding: ECOS2015, Pau, France*. 30 June–3 July, 2015.

Marmutova, S. & Vekara, T. (2014). Grid convergence study of a Savonius wind turbine model. *Conference proceeding: ECOS2014, Turku, Finland. 15–19 of June, 2014*.

McWilliams, M. & Johnson, D.A. (2008). Velocity Measurement of Flow Around Model Vertical Axis Wind Turbines. *International Journal of Green Energy Volume 5, Issue 1–2*. 55–68.

McIntosh S. (2009). *Wind energy for built environment*. University of Cambridge, UK.

Menet, J.-L. (2004). A double-step Savonius rotor for local production of electricity: a design study. *Renewable Energy Volume 29, Issue 11*. 1843–1862.

Modi, V.J., Roth, N.J. & Fernando, M.S.U.K. (1984). Optimum-configuration studies and prototype design of a wind-energy-operated irrigation system. *Journal of Wind Engineering and Industrial Aerodynamics Volume 16*. 85–96.

Modi, V.J., Fernando, M.S.U.K. & Roth, N.J. (1990). Aerodynamics of The Savonius Rotor: Experiments And Analysis. *Proceedings of the 25th Intersociety Energy Conversion Engineering Conference: IECEC-90*. Reno, USA. 12–17 August, 1990.

Mohamed, M.H., Janiga, G., Pap, E. & Thévenin, D. (2011). Optimal blade shape of a modified Savonius turbine using an obstacle shielding the returning blade**.** *Energy Conversion and Management Volume 52, Issue 1*. 236–242.

Nakajima, M., Lio S. & Ikeda, T. (2008). Performance of double-step Savonius rotor for environmentally friendly hydraulic turbine. *Journal of Fluid Science and Technology Volume 3, Issue 3*. 410–419.

Ogawa, T., Toshida, H. & Yokota, Y. (1989). Development of rotational speed control systems for a Savonius-type wind turbine. *Journal of Fluids Engineering Volume 111*. 53–58.

Ohs, R.R., Skidmore, G.J. & Bedrosian, G. (2010). Modelling the effects of wind turbines on radar returns. *Proceeding of the Military communication conference MILCOM*, San Jose, USA. 31 October–3 November, 2010. 272–276.

Paraschivoiu, I. (2009). *Wind turbine design: with emphasis on Darrieus concept*. Presses Internationales Polytechnique. 15–28.

Pinto, J., Matthews, J.C.G. & Sarno, G.C. (2010). Stealth technology for wind turbines. *IET Radar, Sonar & Navigation Volume 4, Issue 1*. 126–133.

Pinto, J., Matthews, J.C.G. & Sarno, C. (2009). Radar signature reduction of wind turbines through the application of stealth technology. *Proceedings of the Third European Conference on Antennas and Propagation (EuCAP), Berlin, Germany*. 23–27 March, 2009. 3886–3890.

Roache, P.J. (1994). Perspective: A method for uniform reporting of grid refinement studies. *Journal of fluids engineering Volume 116*. 405–413.

Savonius, S. J. (1931). The S-rotor and its applications. *Mechanical Engineering Volume 53, Issue 5*. 333–338.

Savonius, S.J. (1925). *The wing-rotor in theory and practice*. Helsingfors: Savonius.

Saha, U.K. & Rajkumar, M.J. (2006). On the performance analysis of Savonius rotor with twisted blades. *Renewable Energy Volume 31, Issue 11*. 1776–1788.

Saha, U.K., Thotla, S. & Maity, D. (2008). Optimum design configuration of Savonius rotor through wind tunnel experiments. *Journal of Wind Engineering and Industrial Aerodynamics Volume 96, Issue 8–9*. 1359–1375.

Seguro, J.V. & Lambert, T.W. (2000). Modern estimation of the parameters of the Weibull wind speed distribution for wind energy analysis. *Journal of Wind Engineering and Industrial Aerodynamics Volume 85, Issue 1*. 75–84.

Simonds, M.H. & Bodek, A. (1964). *Performance test of a Savonius rotor*. Brace research Institute, McGill University, Quebec, Canada. Technical report No. T10.

Spera, D.A. (2009). *Wind turbine technology: Fundamental concepts of wind turbine engineering*. 2nd ed. ASME Press; cop. 2009, New York. 281–287.

Scheurich, F. & Brown, R.E. (2013). Modelling the aerodynamics of vertical-axis wind turbines in unsteady wind conditions. *Wind Energy Volume 16, Issue 1*. 91–107.

Shaheen, M., El-Sayed, M. & Abdallah, S. (2015). Numerical study of two-bucket Savonius wind turbine cluster. *Journal of Wind Engineering and Industrial Aerodynamics Volume 137, Issue 0*. 78–89.

Sharpe, L. (2008). Hopes for solution to wind-farm radar obstacle, *Engineering and Technology Magazine E&T, [Online],Volume 3, Issue 19*. 4–11.

Sieros, G., Chaviaropoulos, P., Sørensen, J. D., Bulder, B. H. & Jamieson, P. (2012). Upscaling wind turbines: theoretical and practical aspects and their impact on the cost of energy. *Wind energy Volume 15, Issue 1*. 3–17.

Sun, X., Luo, D., Huang, D. & Wu, G. (2012). Numerical study on coupling effects among multiple Savonius turbines. *Journal of Renewable Sustainable Energy Volume 4*.

Troen, I. & Lundtand Petersen, E. (1989). European Wind Atlas. Riso National Laboratory, Roskilde.

Tu, J., Yeoh, G.H. & Liu, C. (cop. 2013). *Computational fluid dynamics: a practical approach, 2nd ed*. Elsevier/Butterworth-Heinemann, Waltham, MA.

U.S. Department of Defence. (2006). *Report on effects of windmill farms on military readiness*.

Weisser, D. (2003). A wind energy analysis of Grenada: an estimation using the 'Weibull' density function. *Renewable Energy Volume 28, Issue 11*. 1803–1812.

Wilcox D.C. (1994). *Turbulence modelling for CFD*. DCW Industries, Inc., USA.

Windside. 2015 Available at (last accessible at 19.01.2016): http://www.windside.com/

WIPO. World intellectual property organization. Available at (last accessible at 3.12.2015):
http://www.wipo.int/patentscope/en/

Young, H.D., Freedman, R.A., Ford, A.L. & Sears, F.W. (2003). Sears and Zemansky's University Physics: With modern physics. 11th ed. San Francisco: Pearson Addison-Wesley; cop. 2003. 362–364.

Zhao, Z., Zheng, Y., Xu, X., Liu, W. & Hu, G. (2009). Research on the improvement of the performance of Savonius rotor based on numerical study. *Sustainable Power Generation and Supply, 2009. SUPERGEN '09, Nanjing, China*. 6–7 April, 2009. 1–24.

Zhou, T. & Rempfer, D. (2013). Numerical study of detailed flow field and performance of Savonius wind turbines. *Renewable Energy Volume 51, Issue 0*. 373–381.

Zikanov, O. (2010). *Essential computational fluid dynamics*. Wiley. 230–250.

Appendices

Appendix 1. Fundamentals of numerical analysis.

The governing equations of fluid dynamics are the fundamental base of CFD. Essentially the governing equations denote mathematical statement of the conservation laws of physics:

(i) Conservation of mass for fluid,

(ii) The rate of change of momentum equals the sum of forces acting on fluid.

The third fundamental equation, namely the energy conservation equation, is derived from the consideration of the first law of thermodynamics. It is not detailed in this section since the flow in the model is treated with a constant fluid density and no temperature effect.

The continuity equation

The law of conservation of mass states that matter may be neither created nor destroyed. Let a certain volume of fluid move in space. This volume is represented as a cube, for simplification, in Figure A.1.1.

The control volume $\Delta x \Delta y \Delta z$ is fixed in space with the flow field with velocity vector (u, v, w) around and through it. According to the conservation law the rate of change of mass within the control volume is equal to the net rate at which mass enters and leaves the control volume:

(A1.1) $$\frac{dm}{dt} = \sum_{inlet} \frac{dm}{dt} - \sum_{outlet} \frac{dm}{dt}.$$

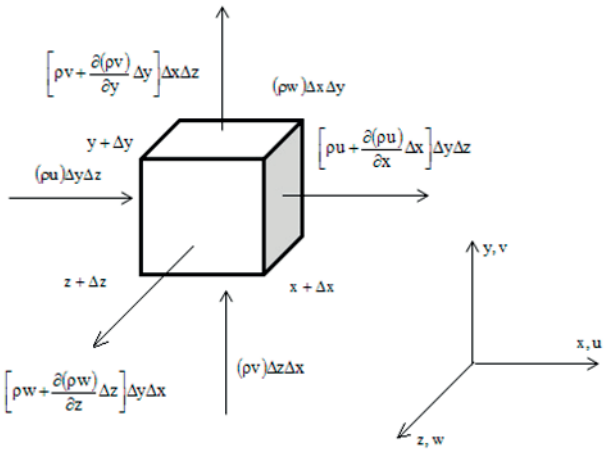

Figure A1.1. Illustration of conservation of mass in an infinitively small control volume of a fluid. (Tu et al. 2013)

The rate at which mass enters perpendicularly through each surface can be expressed as

(A1.2) x: $(\rho u)\Delta y\Delta z$,

(A1.3) y: $(\rho v)\Delta z\Delta x$,

(A1.4) z: $(\rho w)\Delta x\Delta y$,

where ρ is density of the fluid and $\Delta x\Delta y\Delta z$ are surfaces of the control volume.

Similarly the rate at which the mass leaves the surfaces can be expressed by the Taylor expansion:

(A1.5) $x+\Delta x:\left[\rho u+\frac{\partial(\rho u)}{\partial x}\Delta x\right]\Delta y\Delta z+O(\Delta x,\Delta x\Delta y\Delta z)$,

(A1.6) $y+\Delta y:\left[\rho v+\frac{\partial(\rho v)}{\partial y}\Delta y\right]\Delta x\Delta z+O(\Delta y,\Delta x\Delta y\Delta z)$,

(A1.7) $z+\Delta z:\left[\rho w+\frac{\partial(\rho w)}{\partial z}\Delta z\right]\Delta y\Delta x+O(\Delta z,\Delta x\Delta y\Delta z)$.

A Taylor expansion is applicable since the rate of change of mass is continuous and differentiable and the control volume is infinitively small.

Furthermore, since the mass of the control volume is given by $\rho\Delta x\Delta y\Delta z$, Eq. (**A1.1**) becomes

$$\textbf{(A1.8)}\quad \frac{\partial(\rho\Delta x\Delta y\Delta z)}{\partial t} = (\rho u)\Delta y\Delta z - \left[\rho u + \frac{\partial(\rho u)}{\partial x}\Delta x\right]\Delta y\Delta z + (\rho v)\Delta z\Delta z - \left[\rho v + \frac{\partial(\rho v)}{\partial y}\Delta y\right]\Delta x\Delta z + \\ + (\rho w)\Delta x\Delta y - \left[\rho w + \frac{\partial(\rho w)}{\partial z}\Delta z\right]\Delta y\Delta x + + O(\Delta x, \Delta x\Delta y\Delta z)$$

Cancelling terms and dividing by constant and nonzero value it is obtained:

$$\textbf{(A1.9)}\quad \frac{\partial\rho}{\partial t} + \frac{\partial(\rho u)}{\partial x} + \frac{\partial(\rho v)}{\partial y} + \frac{\partial(\rho w)}{\partial z} = 0\,.$$

This equation represents the partial differential form of the continuity equation.

In this particular case it is assumed magnitudes do not vary along z (two-dimensionality). Assuming also that the fluid is incompressible, ρ is constant. Eq. (A1.9) turnes into more compact view

$$\textbf{(A1.10)}\quad \frac{\partial u}{\partial x} + \frac{\partial v}{\partial y} = 0\,.$$

This equation illustrates the concept of mass conservation for the particular case.

The momentum equation

In order to derive the momentum equation in addition to the fluid flow illustration in Figure A1.1 the forces along the surfaces have to be shown.

According to the Newton's second law of motion the sum of forces acting on the fluid element equals the product of its mass and acceleration of the element. By definition the acceleration is the substantial derivative of velocity component u

$$\textbf{(A1.11)}\quad a_x = \frac{Du}{Dt}\,,$$

where a_x is acceleration along x coordinate direction

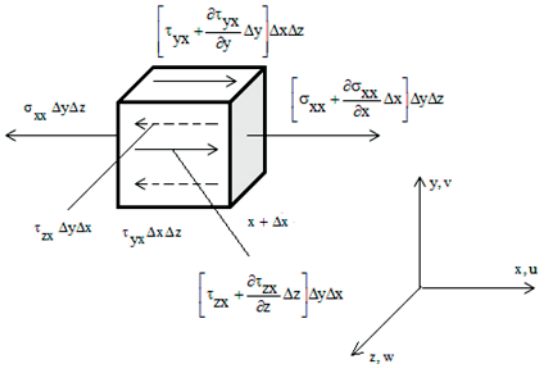

Figure A1.2. Illustration of forces acting on the infinitively small control volume of a fluid for the velocity component u.

Since the mass of the fluid element is $\rho\Delta x\Delta y\Delta z$ the rate of change of momentum in x coordinate direction is $\rho\frac{Du}{Dt}\Delta x\Delta y\Delta z$.

The sum of forces acting on the fluid element includes body forces and surface forces, which may deform the volume element. The body forces greatly depend on the type of interaction and are incorporated by introducing them as additional source terms in addition to the surface forces. The surface forces for the velocity component u contain the normal stresses σ_{xx} and tangential stresses τ_{yx} and τ_{zx}, acting on the surfaces of the fluid element and forming a matrix of tensors. Normal stresses act on a unit area surface, which is normal to the specified by index axis of the Cartesian coordinate system, causing extension or contraction of the fluid element. The off-diagonal elements of the matrix, the tangential stresses, act tangentially to the surfaces of the fluid element and cause its deformation by shear, or make the fluid element rotate, giving rise to the vorticity in the flow.

In the similar manner as the continuity equation bases on the conservation law the momentum equation can be derived.

The net force in the normal x coordinate directions is

(A1.12) $$\left[\sigma_{xx}+\frac{\partial\sigma_{xx}}{\partial x}\Delta x\right]\Delta y\Delta z-\sigma_{xx}\Delta y\Delta z+O(\Delta x,\Delta y\Delta z)\,,$$

the net tangential forces along the x coordinate direction are

(A1.13) $$\left[\tau_{yx} + \frac{\partial \tau_{yx}}{\partial y}\Delta y\right]\Delta x\Delta z - \tau_{yx}\Delta x\Delta z + O(\Delta y, \Delta x\Delta z)$$

and

(A1.14) $$\left[\tau_{zx} + \frac{\partial \tau_{zx}}{\partial z}\Delta z\right]\Delta y\Delta x - \tau_{zx}\Delta y\Delta x + O(\Delta z, \Delta y\Delta x)\,.$$

By adding together Eqs. (A1.12)–(A1.14) and dividing by$\Delta x\Delta y\Delta z$ the total net force per unit volume in x coordinate direction is obtained:

(A1.15) $$\frac{\partial \sigma_{xx}}{\partial x} + \frac{\partial \tau_{yx}}{\partial y} + \frac{\partial \tau_{zx}}{\partial z}\,.$$

Furthermore, the total net surface forces per unit volume in y and z coordinate directions are

(A1.16) $$\frac{\partial \tau_{xy}}{\partial x} + \frac{\partial \sigma_{yy}}{\partial y} + \frac{\partial \tau_{zy}}{\partial z}$$

and

(A1.17) $$\frac{\partial \tau_{xz}}{\partial x} + \frac{\partial \tau_{yz}}{\partial y} + \frac{\partial \sigma_{zz}}{\partial z}\,.$$

Now the Newton's second law can be represented by the body forces (bf) and surface forces

(A1.18) $$\rho\frac{Du}{Dt} = \frac{\partial \sigma_{xx}}{\partial x} + \frac{\partial \tau_{yx}}{\partial y} + \frac{\partial \tau_{zx}}{\partial z} + \sum F_x^{bf}\,,$$

(A1.19) $$\rho\frac{Dv}{Dt} = \frac{\partial \tau_{xy}}{\partial x} + \frac{\partial \sigma_{yy}}{\partial y} + \frac{\partial \tau_{zy}}{\partial z} + \sum F_y^{bf}$$

and

(A1.20) $$\rho\frac{Dv}{Dt} = \frac{\partial \tau_{xz}}{\partial x} + \frac{\partial \tau_{yz}}{\partial y} + \frac{\partial \sigma_{zz}}{\partial z} + \sum F_z^{bf}\,.$$

Assuming that the fluid is Newtonian (namely, the viscosity is independent of the shear stress) and isotropic (the mechanical properties of the fluid are the same along any directions), the normal stresses can be represented through the terms of static pressure and normal viscous stress components: τ_{xx}, τ_{yy} and τ_{zz}. These stresses act perpendicularly to the indexed surface of the control volume

(A1.21) $$\sigma_{xx} = -p + \tau_{xx},$$

(A1.22) $$\sigma_{yy} = -p + \tau_{yy}$$

and

(A1.23) $$\sigma_{zz} = -p + \tau_{zz}.$$

The first component of the sum is the isotropic pressure part, which always presents in the fluid element, and the second component is the viscous or friction part, existing only when the fluid is moving with a velocity gradient along the direction of movement.

A model of the viscous stresses allows expressing of viscous stresses as functions of local deformation rate. By the definition for the Newtonian liquid the shear stress is proportional to the velocity gradient. (Zikanov 2010) According to the Newton's law of viscosity the normal and tangential viscous stresses can be represented by the following equations:

(A1.24) $$\tau_{xx} = 2\mu\frac{\partial u}{\partial x} + \lambda\left[\frac{\partial u}{\partial x} + \frac{\partial v}{\partial y} + \frac{\partial w}{\partial z}\right],$$

(A1.25) $$\tau_{yy} = 2\mu\frac{\partial v}{\partial y} + \lambda\left[\frac{\partial u}{\partial x} + \frac{\partial v}{\partial y} + \frac{\partial w}{\partial z}\right],$$

(A1.26) $$\tau_{zz} = 2\mu\frac{\partial w}{\partial z} + \lambda\left[\frac{\partial u}{\partial x} + \frac{\partial v}{\partial y} + \frac{\partial w}{\partial z}\right],$$

(A1.27) $$\tau_{xy} = \tau_{yx} = \mu\left(\frac{\partial v}{\partial x} + \frac{\partial u}{\partial y}\right),$$

(A1.28) $$\tau_{xz} = \tau_{zx} = \mu\left(\frac{\partial w}{\partial x} + \frac{\partial u}{\partial z}\right),$$

(A1.29) $$\tau_{zy} = \tau_{yz} = \mu\left(\frac{\partial v}{\partial z} + \frac{\partial w}{\partial y}\right).$$

The dynamic viscosity μ relates stresses to the linear deformation, while the second viscosity coefficient λ relates the stresses to the volumetric deformation. It is assumed that for compressible fluids $\lambda = -\frac{2}{3}\mu$. (Tu et al. 2013: 395–400, Buresti 2012: 99–105)

The final forms of the momentum conservation equation, is given by the Navier-Stokes equations:

(A1.30) $$\rho\frac{Du}{Dt} = -\frac{\partial p}{\partial x} + \frac{\partial}{\partial x}\left[2\mu\frac{\partial u}{\partial x} + \lambda\left(\frac{\partial u}{\partial x} + \frac{\partial v}{\partial y} + \frac{\partial w}{\partial z}\right)\right] + \frac{\partial}{\partial y}\left[\mu\left(\frac{\partial u}{\partial y} + \frac{\partial v}{\partial x}\right)\right] + \frac{\partial}{\partial z}\left[\mu\left(\frac{\partial u}{\partial z} + \frac{\partial w}{\partial x}\right)\right] + \sum F_x^{bf},$$

(A1.31) $$\rho\frac{Dv}{Dt} = -\frac{\partial p}{\partial y} + \frac{\partial}{\partial y}\left[2\mu\frac{\partial v}{\partial y} + \lambda\left(\frac{\partial u}{\partial x} + \frac{\partial v}{\partial y} + \frac{\partial w}{\partial z}\right)\right] + \frac{\partial}{\partial x}\left[\mu\left(\frac{\partial v}{\partial x} + \frac{\partial u}{\partial y}\right)\right] + \frac{\partial}{\partial z}\left[\mu\left(\frac{\partial v}{\partial z} + \frac{\partial w}{\partial y}\right)\right] + \sum F_y^{bf},$$

(A1.32) $$\rho\frac{Dw}{Dt} = -\frac{\partial p}{\partial z} + \frac{\partial}{\partial z}\left[2\mu\frac{\partial w}{\partial z} + \lambda\left(\frac{\partial u}{\partial x} + \frac{\partial v}{\partial y} + \frac{\partial w}{\partial z}\right)\right] + \frac{\partial}{\partial y}\left[\mu\left(\frac{\partial v}{\partial z} + \frac{\partial w}{\partial y}\right)\right] + \frac{\partial}{\partial x}\left[\mu\left(\frac{\partial w}{\partial x} + \frac{\partial u}{\partial z}\right)\right] + \sum F_z^{bf}.$$

The Navier-Stokes equation is widely known and certain for the field of fluid dynamics. The interested reader is referred to (Tu et al. 2013), (Zikanov 2010) and (Buresti 2012).

Turbulence models

Irregularity, time-dependence and three-dimensionality are the keywords to define turbulence. It is usually identified as containing mean component (or some form of spatial or temporal averaging) and fluctuations

(A1.33) $$u = \bar{u} + u'$$

The fluctuation patterns in space and time are not random, but follow the rules set by energy and momentum balance equations, boundary and initial conditions. However, it is worth mentioning that in practice it is impossible to

compute an analytical solution of these equations. Because even if inlet boundary conditions describe a laminar flow then all small obstacles, roughness of all surfaces have to be taken into account in the time-dependent model. This approach may lead to more realistic fluctuating velocity, but is computationally very expensive. Practical CFD analysis usually treats the turbulent fluctuations as chaotic (Zikanov 2010).

Flow structures within a turbulent flow have a broad range of time and length scales. It is reflected in the concept of energy cascades. Their characteristic velocity and length are of the same scale as velocity and length scale of the mean flow. The velocity gradient in the mean flow is the source of shear and linear strain and rotation of the fluid. It causes the stretch of the large eddies. This process is called vortex stretching and the turbulence is maintained through this stretching work done by the mean flow on the large eddies. The large flow structures, eddies and vortices, are unstable and constantly generate smaller eddies. These smaller eddies are likewise unstable and turn into smaller eddies. The process of kinetic energy transfer from large to smaller eddies thus takes place. Finally, the kinetic energy of the smallest (Kolmogorov scale) structures under strong velocity gradient dissipates into heat by viscous friction.

The quantitative relations between the length and time scales of the turbulence structures are described by the Kolmogorov turbulent scales. These equations allow estimating the ranges of scales of the flow and are strictly valid for the homogeneous isotropic turbulence and qualitatively correct for general case:

(A1.34) $$\frac{\eta}{L} = \mathrm{Re}^{-3/4}$$

and

(A1.35) $$\frac{\tau}{T} = \mathrm{Re}^{-1/2}$$

where Re is Reynolds number for the flow and η, τ and L, T are length and time scale of smallest and largest turbulence eddies respectively.

The large eddies depend on the mean flow characteristics and their turbulent scales are high enough for the inertia forces to dominate over viscous forces. Hence, the large eddies obtain anisotropic characteristics. The smallest eddies

have much smaller turbulent scales in comparison to viscosity, thus making the flow isotropic, eliminating the directionality of the flow structure.

There are two groups of methodologies of numerical analysis of turbulence: full scale turbulence simulation and turbulence modelling. In the frame of full scale turbulence simulations the full range of turbulence structures is realized. This group includes direct numerical simulation (DNS) and large eddy simulation (LES) methods. The implementation of numerical methods in this group requires consideration of all significant turbulent structures, which means that the computational domain has to accommodate the smallest and the largest turbulent eddy. Thus the DNS and LES are computationally expensive to use and provide accurate results. In this research neither of these methods is used, however.

In turbulence modelling the flow is represented as a sum of mean flow and fluctuations, according to Eq. (A1.33), for the velocity formulation. This approach is called Reynolds-averaged Navier-Stokes method (RANS). For the turbulent model to be useful in general-purpose CFD application it must be robust and simple with wide range of applicability. Engineers are usually interested in obtaining sufficient information about turbulent processes and avoiding modelling of each and every eddy in the flow. For this category of CFD users averaged properties of the flow, namely mean velocities, mean pressures, mean stresses, provide satisfactory results. However, in some cases this method may result in large error introduced by the averaging of the flow characteristics, especially near walls and in multiphase flows.

Eq. (A1.33) replaces the velocity term in the formulation of continuity equation Eq. (A1.9) and momentum conservation equation Eq. (A1.32). Considering incompressible and two-dimensional flow the Reynolds-averaged Navier-Stokes equations are

(A1.36)
$$\frac{\partial \bar{u}}{\partial x}+\frac{\partial \bar{v}}{\partial y}=0\,,$$

(A1.37)
$$\frac{\partial \bar{u}}{\partial t}+\frac{\partial\left(\overline{uu}\right)}{\partial x}+\frac{\partial\left(\overline{uv}\right)}{\partial y}=-\frac{1}{\rho}\frac{\partial \bar{p}}{\partial x}+\frac{\partial}{\partial x}\left(\nu\frac{\partial \bar{u}}{\partial x}\right)+\frac{\partial}{\partial y}\left(\nu\frac{\partial \bar{u}}{\partial y}\right)+\frac{\partial}{\partial x}\left(\nu\frac{\partial \bar{u}}{\partial x}\right)+\frac{\partial}{\partial y}\left(\nu\frac{\partial \bar{v}}{\partial x}\right)$$
$$-\left(\frac{\partial\left(\overline{u'u'}\right)}{\partial x}+\frac{\partial\left(\overline{u'v'}\right)}{\partial y}\right)$$

and

$$\frac{\partial \bar{v}}{\partial t}+\frac{\partial\left(\overline{\bar{u}\bar{v}}\right)}{\partial x}+\frac{\partial\left(\overline{\bar{v}\bar{v}}\right)}{\partial y}=-\frac{1}{\rho}\frac{\partial \bar{p}}{\partial y}+\frac{\partial}{\partial x}\left(v\frac{\partial \bar{v}}{\partial x}\right)+\frac{\partial}{\partial y}\left(v\frac{\partial \bar{v}}{\partial y}\right)+\frac{\partial}{\partial x}\left(v\frac{\partial \bar{u}}{\partial y}\right)+\frac{\partial}{\partial y}\left(v\frac{\partial \bar{v}}{\partial y}\right)$$

(A1.38)

$$-\left(\frac{\partial\left(\overline{u'v'}\right)}{\partial x}+\frac{\partial\left(\overline{v'v'}\right)}{\partial y}\right)$$

The components with fluctuating terms are additional unknowns called *Reynolds stresses*. There are two known approaches to solve this problem. The second-moment closure model, or Reynolds stress model, defines the Reynolds stresses directly by solving a transport equation for each stress component. Another approach is called eddy-viscosity and it states that extra transport terms can be related to the mean flow properties: the Boussinesq approximation assumes that the Reynolds stresses are proportional to the mean rates of deformation

(A1.39)

$$-\rho\overline{u'u'}=2\mu_T\frac{\partial \bar{u}}{\partial x}-\frac{2\rho k}{3},$$

(A1.40)

$$-\rho\overline{v'v'}=2\mu_T\frac{\partial \bar{v}}{\partial y}-\frac{2\rho k}{3}$$

and

(A1.41)

$$-\rho\overline{u'v'}=2\mu_T\frac{\partial \bar{u}}{\partial x}-\left(\frac{\partial \bar{v}}{\partial x}+\frac{\partial \bar{u}}{\partial y}\right),$$

where μ_T is turbulent viscosity, k is turbulent kinetic energy per unit mass.

It is generalised, however, that the motion of turbulent eddies depends on the mean velocity gradient in the same way as molecular transport is governed by the gradients of the full velocity field. Hence, local equilibrium is assumed, which means that the local production and dissipation of turbulence are balanced and the stress tensor is a function of only local turbulent conditions. The eddy-viscosity model is expected to give poor results when applied to modelling of turbulence for flows where the local equilibrium is not observed, for instance, when memory effects of the flow history are to be taken into account. However, the validation by the DNS results shows that the Boussinesq approximation can be applied with an acceptable error for simple parallel shear flows, but not for

flows with more complex structure. (Wilcox 1994) The eddy-viscosity method is quite popular and widely used due to the simplicity and good correlation of results with experimental data if the turbulent viscosity is properly defined.

k-ε and k-ω turbulence models

The local turbulent viscosity is defined through the local turbulent kinetic energy k and turbulent energy dissipation rate ε

(A1.42) $$\mu_T = \frac{C_\mu \rho k^2}{\varepsilon}, \nu_T = \frac{\mu_T}{\rho},$$

(A1.43) $$k = \frac{1}{2}\left(\overline{u'u'} + \overline{v'v'} + \overline{w'w'}\right)$$

and

(A1.44) $$\varepsilon = \nu_T \overline{\left(\frac{\partial u_i'}{\partial x_j}\right)\left(\frac{\partial u_i'}{\partial x_j}\right)}; i, j = 1,2,3,$$

where ν_T is kinematic viscosity and C_μ is turbulent constant.

Dissipation is the rate at which turbulent kinetic energy is transformed into thermal internal energy. It represents the work done by the strain rate of the fluctuating component against the fluctuating viscous stresses. The terms k and ε can be incorporated into the system of Eqs. (A1.36)–(A1.38) by means of their transport equations. The production and destruction of turbulent kinetic energy are closely related and the dissipation rate ε is usually large where the production of kinetic energy k is large.

The standard k-ε model is two-equation model, and it is the most widely used and validated turbulence model. It found its applicability in predicting thin shear layers, boundary layers and free stream flows. However, the model fails to correctly describe swirling flows and flows with large, rapid extra strains. In addition, the assumption of the isotropic character of eddy viscosity causes errors in modelling of flows driven by anisotropic normal Reynolds stresses, as occurs near walls.

The second by popularity two-equation model is k-ω model. In this model the ε-equation is replaced by the equation $\omega = \frac{\varepsilon}{k}$. The term ω is the specific

dissipation rate of the turbulent kinetic energy. As it is pointed out by Wilcox (Wilcox 1994), while the smallest eddies actually dissipate the turbulent kinetic energy into heat, the rate of dissipation is the rate at which the turbulent energy is transferred to the smallest eddies from large eddies. (Wilcox 1994)

The k-ω model shows very good results when the flow is modelled with turbulent fluctuations adjacent to the wall. The viscous effect becomes prominent in this region and special attention has to be paid to the resolution of the viscous sub-layer. Furthermore, the k-ω model performs excellent in modelling of the flow with adverse pressure gradient. However, the model is more sensitive to the free-stream value of ω than k-ε model. (Tu et al. 2013) The more advanced model, which is called k-ω shear stress transport (k-ω SST), incorporates advantages of k-ε model in modelling of free-stream flow and k-ω in modelling of values in boundary layer flows close to wall. Depending on the distance from the wall either k-ω or k-ε model is applied to model turbulence processes.

Concluding, the assumptions of two-equation turbulence models are as given:

(i) The eddy-viscosity model and Boussinesq approximation assume that the Reynolds stresses are proportional to the mean flow rates. However, there is no theory beyond the analogy between the motion of molecules and motion of turbulent eddies. The eddy-viscosity model is widely applied in CFD due to its simplicity and good results with a properly defined turbulent viscosity term.

(ii) Another assumption of the eddy-viscosity model is local equilibrium, which supposes balanced local production and dissipation of turbulent kinetic energy.

(iii) The closure of the turbulent kinetic energy equation applies the approximation coefficients, which have been calibrated against comprehensive data for a wide range of turbulent flows with simple geometry, however.

(iv) The standard k-ε model assumes eddy viscosity to be isotropic. Secondary flows, driven by the anisotropic Reynolds stresses cannot be predicted.

The simulation of wind turbines, and Savonius turbines particularly, demands very accurate modelling of the flow near the turbine surface, since the torque and eventually the power coefficient are one of the important characteristics of the turbine performance. Moreover, the flow around a Savonius turbine may include flow reattachments and high pressure gradient. For these reasons the k-ω models

and second-moment closure models are preferable to use in numerical models of Savonius turbine.

Near-wall region modelling

When modelling wind turbine blades most of the monitoring parameters are integrated along the blade surface, such as: drag and lift forces, torque coefficient. In fact, the torque coefficient of the rotor is defined by the drag and lift coefficients or by the pressure and shear forces acting on the surface of the blades. Hence, in order to correctly predict these two components it is necessary to correctly model the pressure field and the surface shear stress. This, in turn, requires correct treatment and prediction of boundary layers and flow separation.

In the light of turbulence model application the next important step is the choice of a near-wall model to accurately model boundary layer around the turbine blade surface. The boundary layer is a region near the wall where the viscous forces are of the same order as the inertial forces, this region is characterised with small Re. The wall function determines how the boundary layer is modelled at the blade surface. The distance over which the viscous forces have an effect is termed the boundary layer thickness. The thickness is a function of the ratio between the inertial and viscous forces, in other words Re. As Re increases the thickness decreases.

The turbulent flow near a flat wall can be divided into three regions: viscous sub-layer, buffer layer and log-law region. At the wall the velocity of the fluid is zero, so-called “no-slip” condition. Within the boundary layer the fluid flow shifts from the free stream velocity to zero velocity at the wall. (Tu et al. 2013)

The viscous sub-layer possesses the next characteristics:

(i) Within the viscous sub-layer above the wall surface the velocity of the flow is linearly dependent on the distance from the wall, where the viscous forces dominate.

(ii) This layer is also called the laminar sublayer. It is assumed, that the shear stresses are approximately constant and equivalent to the wall shear stress.

(iii) Due to the laminar flow the velocity component normal to the surface is much smaller than the velocity parallel to the surface.

(iv) The gradients of the flow across the viscous sub-layer are much greater than the gradients in the flow direction.

(v) The boundary layer thickness δ extends from the surface to the level where the velocity reaches 99% of the free-stream velocity.

The viscous sub-layer is followed by the buffer layer, where the laminar flow starts transition to turbulent.

The buffer layer is followed by the log-law region, where the flow is fully turbulent and the average flow velocity is related to the log of the distance to the wall. The free-stream region complements the list of flow regions. The viscous and buffer layers are very thin: relatively the thickness of the log-law region covers hundred times the thickness of the viscous and buffer layers together. Figure A1.3 illustrates the fully turbulent fluid velocity profile from the smooth wall up to the free-stream region.

These regions can be distinguished also with the use of fluid flow variables:

(i) Distance to the wall y,

(ii) The wall shear stress τ_W,

(iii) The friction velocity $u_\tau = \left(\frac{\tau_w}{\rho}\right)^{0.5}$,

(iv) Dimensionless wall distance $y^+ = \frac{yu_\tau}{\nu}$, and

(v) Dimensionless velocity $U^+ = \frac{U}{u_\tau}$.

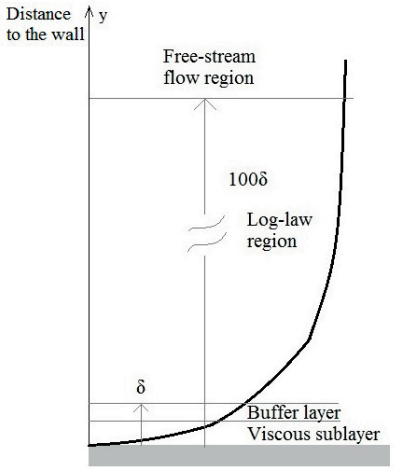

Figure A1.3. The fully turbulent fluid velocity profile for the domain with smooth wall.

The layers of the turbulent flow can be represented as function of the dimensionless distance to the wall $U^+ = f\left(y^+\right)$. Figure A1.4 illustrates this relation.

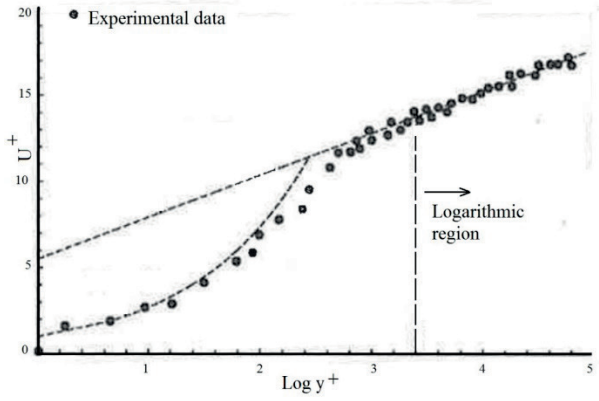

Figure A1.4. Dimensionless velocity profile as a function of the dimensionless wall distance in comparison with the experimental data (adapted from (Tu et al. 2013)).

Based on this representation the boundary layers are defined as given:

(i) The viscous sublayer lies within the $y^+ < 5$. The dimensionless velocity is $U^+ = y^+$,

(ii) The log-law region $30 < y^+ < 500$ and $U^+ = \frac{\ln(E \cdot y^+)}{k}$, where E is an empirical constant which depends on the roughness of the wall.

The fluid flow profiles adopted above are based on two-dimensional attached flow configuration with the following assumptions:

(i) The flow is attached to the wall,

(ii) The flow has small pressure gradients and

(iii)The condition of the local equilibrium of turbulence is fulfilled.

The RANS models are capable of computing the flow field in all of these regimes. For some flow models, where the viscous and buffer layers are thin, it is advantageous to use an approximation in these regions. It is also accepted if no parameters of interest are to be measured in the vicinity of the wall. In these cases the standard wall function can be applied.

The wall function ignores the flow field within the viscous and buffer layers and assigns the computed non-zero fluid velocity at the wall. The experimental boundary layer profile can be used to calculate the wall shear stress τ_w. The dimensionless wall distance value is obtained with the use of a set of correlations:

$$\textbf{(A1.45)}\ y^* = \frac{1}{\mu}\rho C_\mu^{1/4} k_p^{1/2} y_p \Rightarrow \left\{ \begin{array}{l} y^* \geq 11.2 \rightarrow U^* = \frac{1}{\kappa}\ln(Ey^*) \\ y^* < 11.2 \rightarrow U^* = y^* \end{array} \right\} \Rightarrow \tau_w = \frac{\rho U_p C_\mu^{1/4} k_p^{1/2}}{U^*},$$

where index p refers to the centre of the cell adjacent to the wall, and κ is Von Karman constant.

The main goal of the application of the wall function is to take the effect of the boundary layer into account correctly without the necessity to generate the very fine mesh all the way to the wall, which allows calculating of the flow profile within the layer explicitly. Therefore, the first grid point should not be inside the viscous sublayer, and typically it is recommended to keep values of y^+ in the range between 20 and 30 for high Re numbers.

A disadvantage of the standard wall function is the application of empirical correlations. However, if the discussed universal near-wall behaviour may not be realized everywhere in the flow, the wall function concept may lead to significant

errors. The alternative way is to fully resolve the flow up to the wall. This approach is called two-layer zonal model or low Re number turbulent models (LRN). This model is used for low Re flows and flows with complex near-wall phenomena. The model regions are distinguished with the use of turbulent Reynolds number based on the distance to the wall: $\mathrm{Re}_y = \frac{\rho\sqrt{k}y}{\mu}$. In the regions outside the zones affected by the viscosity the regular turbulent models are used. The turbulent kinetic energy equation is solved only in the regions with the viscous effects, while ε is computed using a correlation for a turbulent length scale.

However, it should be noted that the accuracy of the solution comes with a cost. This method demands large computational resources because the flow within the boundary layer is resolved with additional grid points involved. For this, the first grid cell adjacent to the wall must have y^+ value close to unity

(A1.46) $y^+ = 1.$

As long as the viscous sublayer lies within the region with the $y^+ < 5$, this range of y^+ values is acceptable as well. Table A1.1 compares the main pros and cons of the two approaches.

Table A1.1. Advantages and disadvantages of the approaches of modelling of the near-wall region.

Model	Strength	Weakness
Standard wall function	(i) Robust (ii) Economical (iii) Reasonably accurate for the appropriate fluid flow modelling	(i) Uses empirical correlations (ii) Poor performance for low-Re effects and non-equilibrium flows
Two-layer zonal model	(i) Explicitly calculates the flow in the boundary layer (ii) Applicable to model the non-equilibrium flows	(i) Requires finer mesh resolution, hence larger computational resources

The flow around a Savonius rotor is characterised by high pressure gradients and even flow reattachments. Under such circumstances, the flow must be resolved down to the wall. In this study in the model of Ansys Fluent it is achieved with the use of the low Reynolds number turbulence model (LRN). The computational cost of such a model increases considerably due to additional grid nodal points involved. The LRN model intends to resolve the viscous sublayer and hence the

first mesh cell and generally a mesh within the viscous sublayer has to be defined in accordance to this condition. A more detailed analysis and application is shown in the mesh generation chapter.

Temporal and spatial discretization

The obtained partial differential equations can be solved analytically for some simple cases with a number of flow field assumptions. However, if the analytical solution is unavailable the equations have to be solved numerically. The process of obtaining the computational solution includes the conversion of partial differential equations and application of boundary or initial conditions into a system of discrete algebraic equations. This is called the discretization stage. Discretization can be described as replacement of an exact solution of PDEs in a continuum domain by an approximate numerical solution in a discrete domain. The final solution represents a finite set of numerical values. It should be mentioned that spatial and temporal discretization exist. Since the temporal discretization bases on the finite difference method in this section the spatial discretization is termed as discretization for the sake of simplicity. However, the finite difference method can be used to illustrate the principle of discretization and one of the error sources in numerical solution.

Discretization techniques

The starting point of the discretization procedure is defining the numerical grid. In finite difference particularly the grid must be locally structured, so that each grid node may be considered as the origin of a local coordinate system. Figure A1.5 illustrates the two-dimensional Cartesian grids with uniform distribution of nodes. In some cases the distribution can be not uniform, for instance when the flow field gradient is larger in y coordinate direction then Δy can be smaller than Δx.

In Figure A1.5, indices *i* and *j* indicate the grid lines and the relative location of grid nodes is identified with corresponding indices. The difference between the real flow function and numerical solution is that the values of the flow variables are provided only at the discrete points of the domain.

The Taylor series expansion is used to represent the partial differential equations in the finite difference form. If θ is flow field variable then the Taylor series expansion applied around point (i, j) gives:

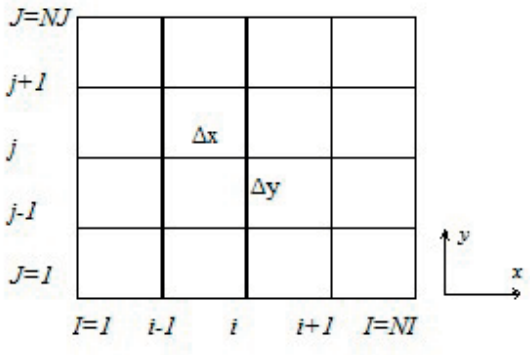

Figure A1.5. Two-dimensional Cartesian grid with uniform distribution of nodes for finite-difference method.

(A1.47) $$\theta_{i+1,j} = \theta_{i,j} + \left(\frac{\partial\theta}{\partial x}\right)_{i,j}\Delta x + \left(\frac{\partial^2\theta}{\partial x^2}\right)_{i,j}\cdot\frac{\Delta x^2}{2!} + \ldots + \left(\frac{\partial^n\theta}{\partial x^n}\right)_{i,j}\cdot\frac{\Delta x^n}{n!}.$$

Similarly the variable at point (i−1, j) is expressed:

(A1.48) $$\theta_{i-1,j} = \theta_{i,j} - \left(\frac{\partial\theta}{\partial x}\right)_{i,j}\Delta x + \left(\frac{\partial^2\theta}{\partial x^2}\right)_{i,j}\cdot\frac{\Delta x^2}{2} + \ldots + (-1)^n\left(\frac{\partial^n\theta}{\partial x^n}\right)_{i,j}\cdot\frac{\Delta x^n}{n!}.$$

According to the Taylor series definition Eq. (A1.47) and Eq. (A1.48) are mathematically exact Eqs. for the variables $\theta_{i+1,j}$ and $\theta_{i-1,j}$ if either the number of terms is infinite or the step $\Delta x \to 0$. The subtraction of the two equations gives the approximation of the first-order derivative of θ

(A1.49) $$\frac{\partial\theta}{\partial x} = \frac{\theta_{i+1,j} - \theta_{i-1,j}}{2\Delta x} + O\left(\Delta x^2\right).$$

Eq. (A1.49) is the second-order accurate since the truncation error is of an order of $(\Delta x)^2$. The central difference approximation applies equal weight to the values of variable from both sides of the point (i, j). The first-order difference schemes take into account the value from one side of the point (i, j). As a result the forward and backword difference schemes are first-order accurate and less accurate than the central difference

(A1.50) $$\frac{\partial\theta}{\partial x}=\frac{\theta_{i+1,j}-\theta_{i,j}}{\Delta x}+O(\Delta x),$$

(A1.51) $$\frac{\partial\theta}{\partial x}=\frac{\theta_{i,j}-\theta_{i-1,j}}{\Delta x}+O(\Delta x).$$

The term $O(\Delta x^2)$ is the truncation error of the finite-difference approximation. It defines the accuracy of approximation and the rate at which the error decreases as the step of discretisation Δx decreases. It contains the rest of the series and thus shows the difference between Eqs. (A1.47), (A1.48) and Eq. (A1.49). Although the value of truncation error cannot be estimated without knowing the exact function $\theta(x)$, it is a characteristic of the accuracy of the finite difference scheme. If the truncation error vanishes with $\Delta x \to 0$ the scheme is considered consistent.

However, it has to be taken into account that not only the step size matters but also the behaviour of the function. The strong gradient of the approximated function in the vicinity of the grid point (i, j) even with the consistent discretisation scheme and small Δx can cause significant error. This issue is discussed later in this chapter in the section devoted to the mesh convergence.

The second-order derivative is obtained by summation of Eq. (A1.47) and Eq. (A1.48)

(A1.52) $$\frac{\partial^2\theta}{\partial x^2}=\frac{\theta_{i+1,j}-2\theta_{i,j}+\theta_{i-1,j}}{\Delta x^2}+O\left(\Delta x^2\right).$$

Similar equations can be formulated with respect to y and z coordinate direction. The temporal discretization follows the forward difference pattern

(A1.53) $$\frac{\partial\theta}{\partial t}=\frac{\theta_{i,j}^{n+1}-\theta_{i,j}^{n}}{\Delta t}+O(\Delta t).$$

In this study two discretization methods are used: finite element (Comsol Multiphysics®4.3a) and finite volume (Ansys Fluent®15.0). The finite element and the finite volume methods have similarities. The main difference of these two approaches from the finite difference method is the discretization technique. Instead of discretization of a partial differential equation the conservation law in the integral form is used. A control volume is bounded by the surface areas of the element, which are used for the discretization of the first- and second-order derivatives of the flow filed property θ. The surface areas in the direction normal

to the control volume surfaces are projected on the Cartesian coordinate system. According to the balance equations the projected areas are positive if the direction of the outward normal vector from the volume surface coincides with the coordinate positive direction. Gauss divergence theorem is then applied.

One of the important advantages of the finite volume method is flexibility in the type of mesh which can be used. As this method appeals to the control volumes but not the grid intersection points it is capable of accommodating any type of grid. A combination of triangles and quadrilaterals in two-dimensional case opens wider opportunities in resolving complex geometries.

The finite element method has the same advantage. The important difference is that with the finite element method the governing equations have to be first multiplied by the so-called shape function before they are integrated along the entire computational domain. One of the ways to obtain the shape function is to assume a linear distribution of the values between the corners of the element.

The finite element method has not found such extensive use as finite volume method in CFD applications. Generally, it demands more computational resources and computer power than finite volume method. Table A1.2 shows some details about the models and time needed for simulations. Definitely this is not a parametric study of the discretization method or any other parameters listed in the table, since all of them vary. However, these conditions are to be considered as necessary to fulfil in order to obtain the solution by each program. From the engineering point of view Ansys Fluent®15.0 is able to perform more complicated tasks with less computational resources used.

Table A1.2. Data on the computational resources needed to implement numerical models of Comsol Multiphysics®4.3a and Ansys Fluent®15.0.

	Comsol Multiphysics®4.3a	**Ansys Fluent®15.0**
Re	62 000	160 000–490 000
Rotor diameter (m)	0.24	1
Mesh elements	380 000	250 000
Computational domain(m^2)	2.4x3.2	14x9
Turbulence model	k-ε, standard wall function	k-ω SST, LRN
Simulation time, days	≈12	≈4
PC used for this work	2duo CPU 3.16GHz 6Gb RAM	2duo CPU 3.16GHz 6Gb RAM

Appendix 2. Interaction of HAWTs with radars

The rated power and physical dimensions of HAWTs are continuously increasing. Therefore, with the development of HAWT technology, future turbines up to 20 MW are expected to have rotor diameter up to 250 m and hub height of more than 150 m (Sieros et al. 2008). With the typical rotor diameters (from 40 m to 126 m) and rotational frequencies (from 1.2 rad/s to 3.6 rad/s), blade tip velocities can exceed 77 m/s or 150 Knots, which is comparable with a slow aircraft (Ohs et al. 2010).

A typical HAWT for radar interference studies is the Vestas V82 turbine with 40 m The wind turbine interference with radar depends on several parameters, such as a tower height, a rotor diameter and a rotational frequency. Because of its distinct parts, a HAWT is divided into the following components: the tower, blades and the nacelle. In the subsequent sections, each component of a HAWT is briefly analysed in order to introduce the interaction between radars and HAWTs and a Savonius turbine as well.

Tower RCS

A HAWT tower is usually manufactured from either concrete or, more often, from rolled steel. The large physical size of a turbine tower is the reason that it contributes to about 75 % of the total turbine RCS. (Pinto et al. 2010)

Both a HAWT tower and the whole Savonius rotor can be considered as consistent of a number of cylinders. Then the complex target scattering method can be applied to each of these sections. (Knott et al. 2004) The integration of the results along the tower height gives the tower RCS. According to this method the RCS of the cylinder $\sigma_{cylinder}$ is proportional to its height L and radius R

$$\sigma_{cylinder} = \frac{2\pi R}{\lambda} L^2, \quad \text{(A2.1)}$$

where λ (m) is the wave length of the incoming signal. An increase in diameter of a HAWT blade entails an increase in height of the tower, or a rotor height and diameter in case of VAWTs. Based on Eq. (A2.1) this increase causes an increase in the RCS of wind turbines of both types.

Blade RCS

The blades of a HAWT contribute to the total turbine RCS. Due to the asymmetry of the blades plane of rotation the angle of incidence of the incoming signal has to be taken into account. Two turbine positions were investigated by Pinto et al.

(2010): blades rotating in parallel or perpendicularly to the plane of the radar signal propagation. The contribution to the total turbine RCS by three blades is about 15%. It has been reported that the turbine RCS is nearly independent of the blade rotation angle when the blades rotate towards and away from the signal direction of propagation. As the blades rotate, the main shape of the turbine does not change considerably to affect the RCS. (Pinto et al. 2010)

If the direction of propagation of radar signals is in parallel with the long axis of a HAWT hub, RCS changes considerably depending upon a blade position. The RCS fluctuates from the average by approximately a 2%. (Pinto et al. 2010)

Nacelle RCS

The The nacelle of a HAWT contains mechanical and electrical equipment for power generation and is able to rotate by 360^{0}, allowing the turbine to face the wind and hence operate with maximum efficiency. The physical size of the nacelle and relative orientation to the radar signal are the primary parameters which influence on the turbine RCS. This contribution is estimated to be near 10% of the total turbine RCS (Pinto et al. 2010). The nacelle rotates slowly, that is why the radar considers the nacelle as a virtually stationary object (U.S. department of defence 2006).

The Doppler effect

The Doppler Effect represents a change in the phase between consecutive pulses, emitted by radar and reflected by moving target.

A Doppler radar uses the Doppler Effect to detect moving targets and to obtain data on its velocity. The basic principle of a Doppler radar is the comparison of two successively received signals reflected by a target. The transmitted and received signals reflected by a stationary object are nearly identical, since it reflects the waves at the same phase. On the other hand, the successive signals from a moving target vary in phase at the receiving point. Therefore, the difference between the signal phases, which is the Doppler frequency, is nonzero.

The moving parts of a wind turbine can cause visible Doppler Effect to radar. For this reason, the movement of the blades should be taken into account.

The biggest contribution to the total Doppler frequency of a turbine is made by turbine blades. Each part of the blade has its own rotational frequency depending on the distance from the rotating centre. The rotating blades produce continuous spectrum of the Doppler frequency in the range of the Doppler limits that air surveillance radars are able to detect. The Doppler frequency as a function of the

blade position in time is characterized by a nearly constant value near zero and frequency peaks, which correspond to the specific blade position. In the reported study the blades rotated towards and away from the signal direction of propagation. The highest Doppler frequency is observed when one of the blades is orthogonal to the radar signal. The nacelle and the section of the blade closely located to the hub add this near zero value to the total Doppler frequency. The tip parts of a blade, having highest rotating frequency, create the peaks of the Doppler frequency function. (Lok et al. 2011)

Appendix 3. Scheme of the CFD iterative procedure and application of Ansys Fluent®15.0 and Comsol Multiphysics®4.3a within CSC environment

Before an iterative procedure of a solver can be initialized a numerical model must be built. A number of aspects of this process, which are important to be familiar with, are described in the Chapter 2 and Appendix 1. Among them are spatial and temporal discretization and a choice of a turbulence model. After the model is built the solver initiates the iterative process according to the scheme on Figure A3.1.

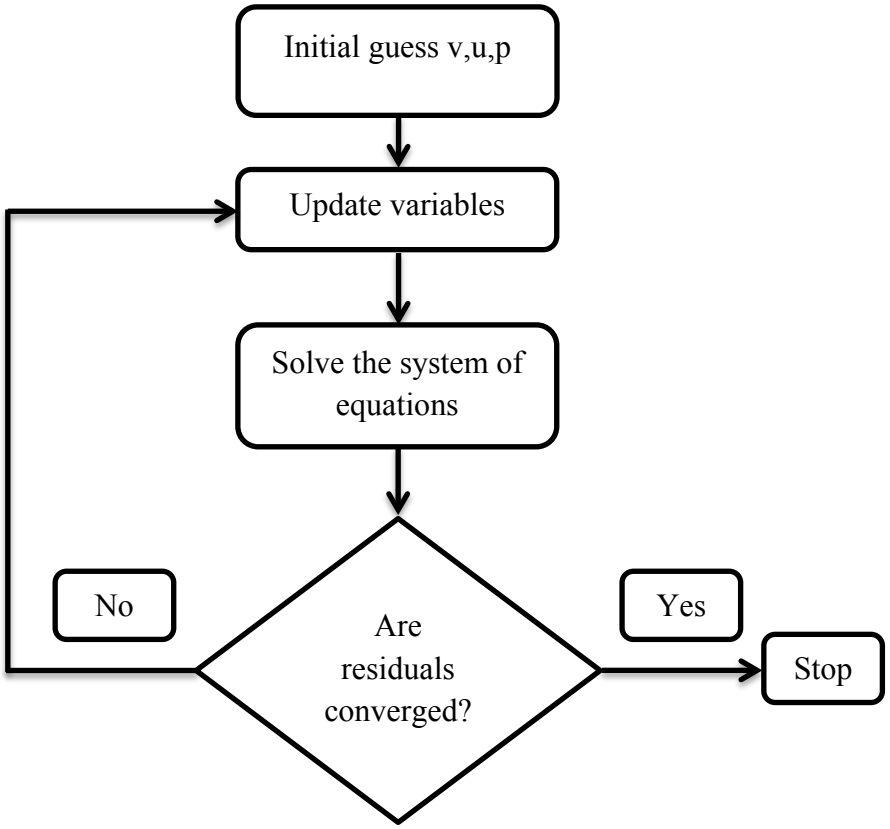

Figure A3.1. Scheme of the iterative procedure of the solver.

Further in this section some aspects of work within the CSC environment are described. Access to a personal page and uploaded files is available at the scientist's user interface (SUI).

Within a file directory user can create folders and upload working files, such as Comsol model files (.mph) or Fluent working files (.cas). The files should be

stored at the working directory "$WRKDIR", but not at the home directory "$HOME". The reason is the available space of these directories.

SSH Console

There are two ways to start Comsol Multiphysics®4.3a model files. One way is to launch SSH console under the SUI services.

The title of the remote host should be provided by the CSC. In order to open Comsol Multiphysics®4.3a the next command are to be executed within the launched console: "cd $WRKDIR module load Comsol/Comsol4.3a".

After the window with the Comsol Multiphysics®4.3a is opened the user can open the prepared model file (.mph) or create a new file. However, it is more convenient and faster to create the file on PC, upload to the $WRKDIR and open it within the launched program. After the model file is executed resulting files can be saved at the same directory and then downloaded to the PC for further use. The same approach can be used in order to launch Ansys Fluent®15.0. The Java script is to be up to date if the user works with SSH console.

NoMashine interface

Details on the NoMachine interface and connections can be found at the official CSC webpage. Within the NoMachine remote desktop right click provides available hosts.

Further, after the host is chosen the same commands as in SSH console are used.

Script.sh

Another way to launch Ansys Fluent®15.0 is to create a script.sh file using the Batch Job Script Wizard under the SUI services. As it is seen from the specification the script.sh file requests the "journalfile_par". It is the .txt file, which can be created in the file directory: right click → create new file → edit this file. Otherwise a file can be created at a PC and uploaded to the file directory. In the .txt file the next information must be provided: execution method (parallel/partition/auto/use-case-file-method yes), the exact title of the .cas file (file/read-case FFF-8.1-10-00180.cas.gz), type of initialization (solve/initialize/hyb-initialization), number of iterations (solve/dual-time-iterate 4000 exit yes).

After these files are created the script.sh file can be submitted for batch job as shown in Figure A3.2. Depending on the requested computing time and number of nodes scheduler allocates the submitted job in the queue. The larger the needed computational resources the longer is the awaiting time. The illustrated here simple file was executed almost immediately.

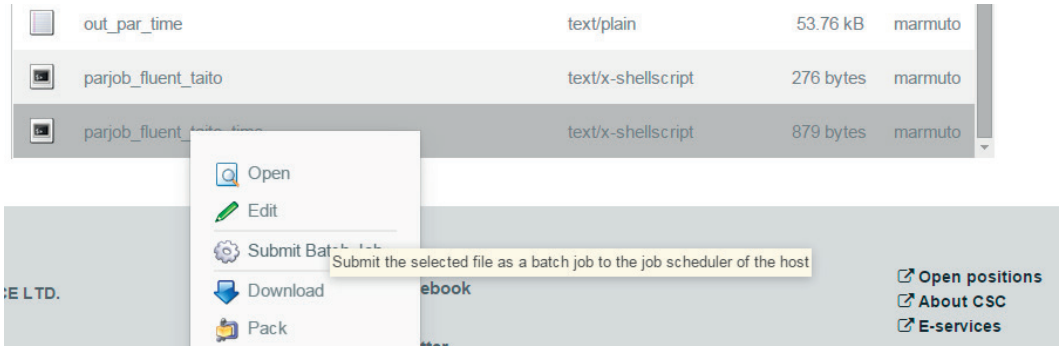

Figure A3.2. Submitting the script.sh file as a batch job to the job scheduler of the host.

After all iterations are performed the files with error message and output data are created. In the output file the process of the file execution is reported. The same message is shown to the user within the GUI window when the file is executed at a PC. The process can be followed through the output text file.

In the working file .cas the output parameter is the moment coefficient along a rotor surface at each time step. During a simulation process a file is created with the values of the moment coefficient as a function of flow time.

Appendix 4. An overview of the patents related to Savonius wind turbine

Table A4.1 contains information on the published patents on the devices, which improve the various aspects of a Savonius wind turbine operation. (WIPO 2015) Among the more than three hundreds patents connected to the Savonius wind turbine operation and applications these patents are chosen according to the next criteria:

(i) The patented solution reveals a brand new idea of a rotor modification. Either a new blade shape or configurations of blades are proposed. Slight variations of the existing configurations are not reported;

(ii) Patent description and documentation are clear and validated by the provided discussion or test results;

(iii) Patented modification focuses on the improvement of the aerodynamic efficiency of Savonius rotor.

(iv) Devices which improve any parameters of Savonius wind turbine operation and eliminate advantages of other parameters are not reported.

Table A4.1. Data on patents related to Savonius wind turbine operation.

Inventor	Modification and achievement	Patent number Language Date
Guignard, S.	Rotor has straight blades of various shapes. Tips of the blades are equipped with flexible extensions to redirect the flow and increase the torque value. It is expected to double of the rotor aerodynamic efficiency.	(WO/2015/150697) French 08.10.2015
Lagov, P. Drenin, A.	The central shaft embeds helical Savonius rotor and Darrieus rotor. The surface of Savonus rotor is covered with the photoelectric cells. The power from the photoelectric cells is used to start the rotor under the low wind speed conditions	(WO/2015/088370) English, French 18.06.2015
Hench, S. Fralick, C.	Blades have semi-circular or hemispherical shape and are formed of a collapsible material such as fabric. End plates are made from rigid materials. Reduced cost, weight. Portability	(US09051918) English 09.06.2015
Kim, J-W.	A number of dimples on the convex side of the rotor blades are added to cause separated flow retardation and hence reduce the pressure drag force on the returning blade. Negative torque from the convex side of the returning blade can be reduced	(US20150110627) English 23.04.2015
Swamidass, P.	Application of blades, which are able to tilt or swivel by the flow, when the blade is in the returning position. The power coefficient increases since the resistance component is eliminated	(US20140140812) English 22.05.2014
Lim, H-c. Kim, Y-h.	Rotor blades are made from the elastic units and are supported by a number of pivot columns. Pivot panels of the advancing blade are open and panels of the returning blade are closed. The rotor torque is expected to increase	(WO/2013/108953) English, French, Korean 25.07.2013
Wunderlich, B., Thevenin, D., Mohamed, M.	Optimization of the obstacle location in front of the rotor blades. The obstacles tend to redirect the inlet flow from the returning blade towards the advancing blade and focus the flow on the advancing blade. The deflector can rotate to follow the changes in wind direction. The power output of Savonius rotor increases.	(DE102011100630) German 08.11.2012
Schul, K.D.	Each rotor blade is composed from two semi-circular surfaces of different diameters. The form diffusor, which in the advancing position create positive torque, direct and accelerate the flow towards the concave side of the returning blade. Thus the total torque increases.	(EP2449256) German 09.05.2012
Jiefu, Z., Yipeng, D., Guang, H., Xiaowen, S., Hongbin, H.	The curvature of each blade of three-bladed Savonius rotor decreases from the rotor centre. The root of each blade is provided with a number of overflow holes. Due to the blade shape the positive torque increases and the resistance of the returning blade decreases due to the holes in the root part of the blades.	(CN102094750) Chinese 15.06.2011

Appendix 5. Details on the flow field around conventional and modified Savonius rotor

In this section the data on the flow velocity around the conventional and modified Savonius rotor is represented. The Figures A5.1–A5.13 are obtained using the numerical model, which is verified in Section 3.2.

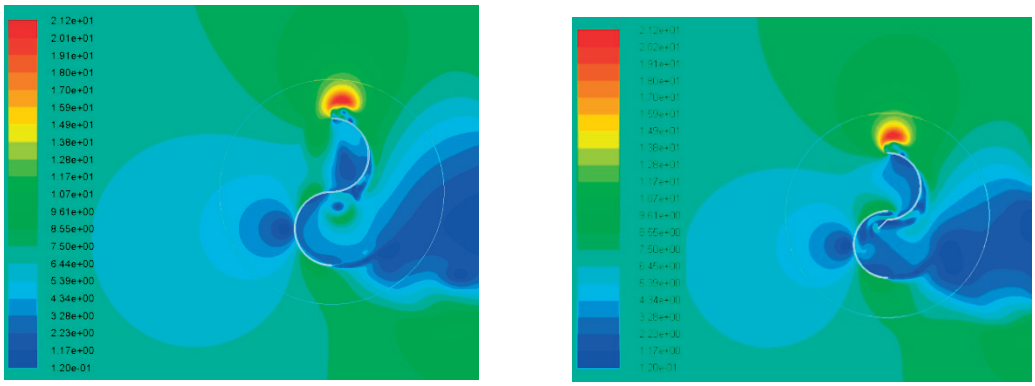

(a) (b)

Figure A5.1. Contour of the flow velocity around conventional rotor (a) and modified rotor (b) at rotor angle 0°.

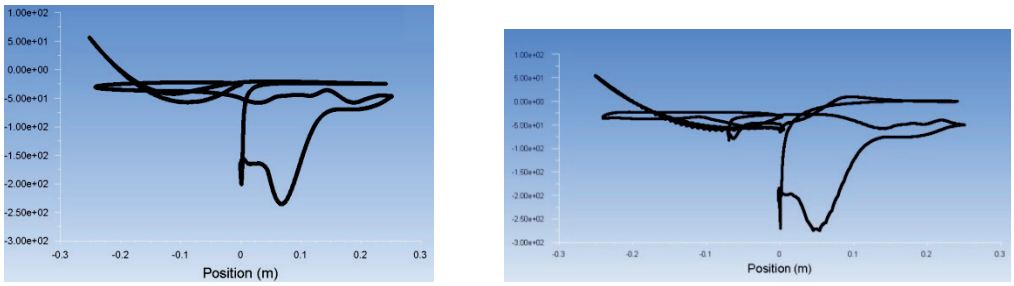

(a) (b)

Figure A5.2. Pressure distribution along the blade surfaces at rotor angle 0°: conventional rotor (a) and modified rotor (b).

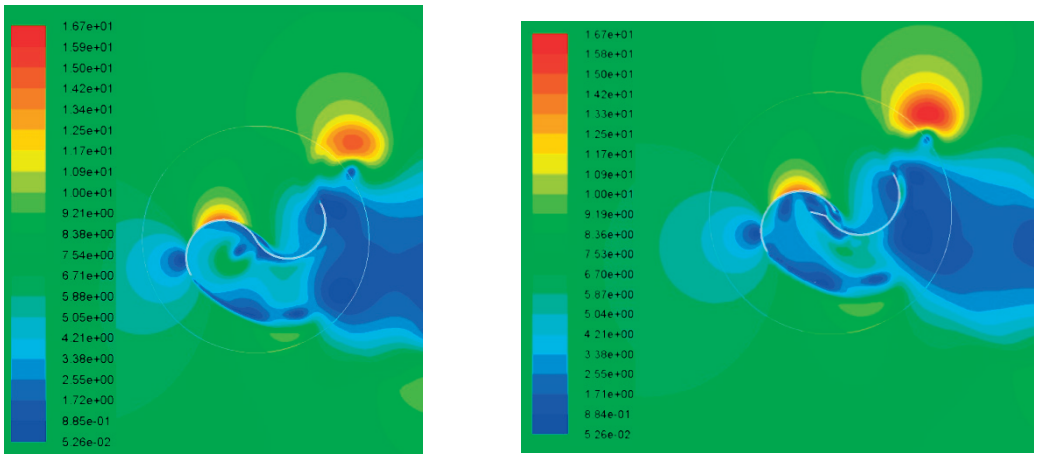

(a) (b)

Figure A5.3. Contour of the flow velocity around conventional rotor (a) and modified rotor (b) at rotor angle 60°.

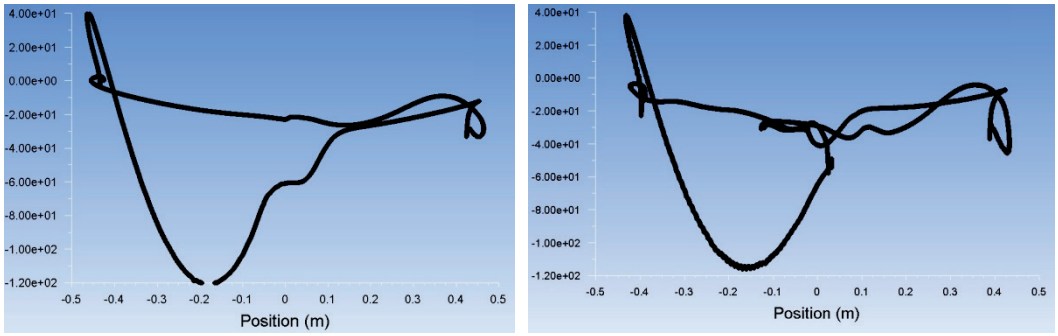

(a) (b)

Figure A5.4. Pressure distribution along the blade surfaces at rotor angle 60°: conventional rotor (a) and modified rotor (b).

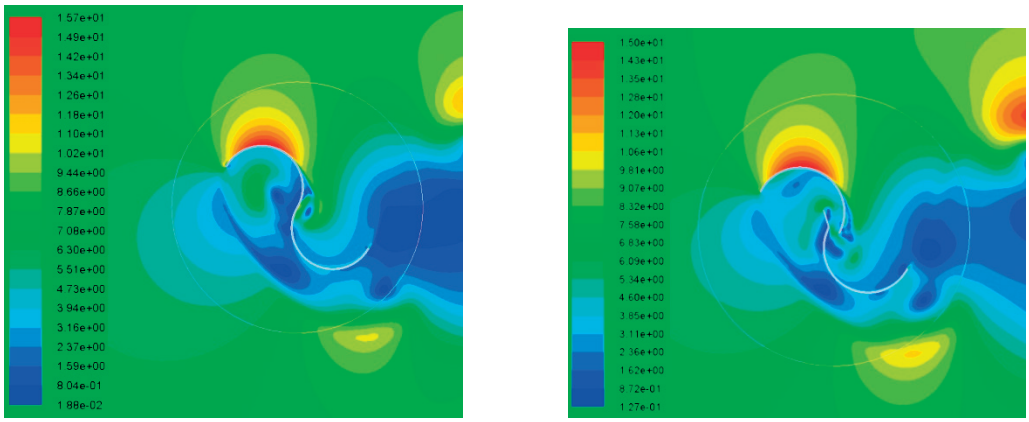

(a) (b)

Figure A5.5. Contour of the flow velocity around conventional rotor (a) and modified rotor (b) at rotor angle 120°.

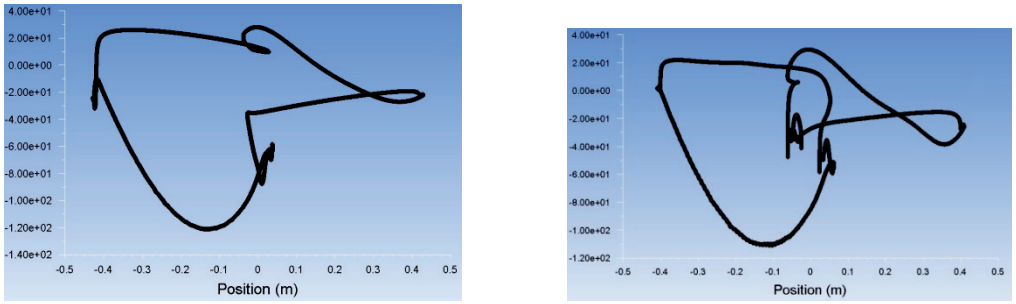

(a) (b)

Figure A5.6. Pressure distribution along the blade surfaces at rotor angle 120°: conventional rotor (a) and modified rotor (b).

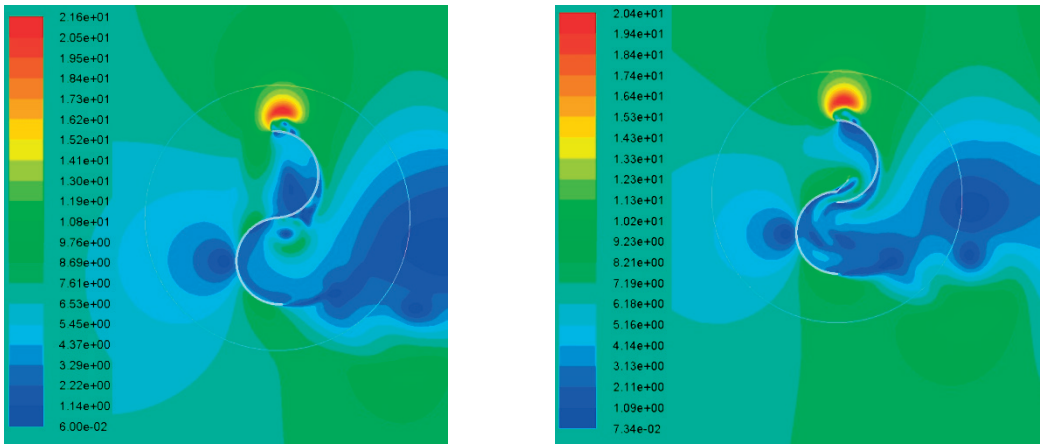

(a) (b)

Figure A5.7. Contour of the flow velocity around conventional rotor (a) and modified rotor (b) at rotor angle 180°.

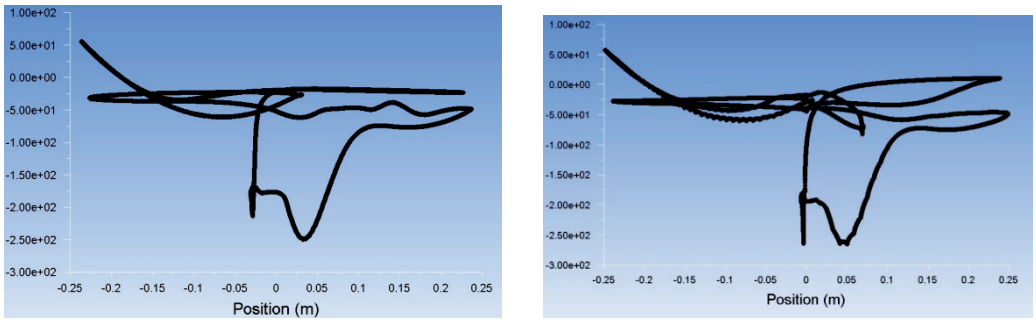

(a) (b)

Figure A5.8. Pressure distribution along the blade surfaces at rotor angle 180°: conventional rotor (a) and modified rotor (b).

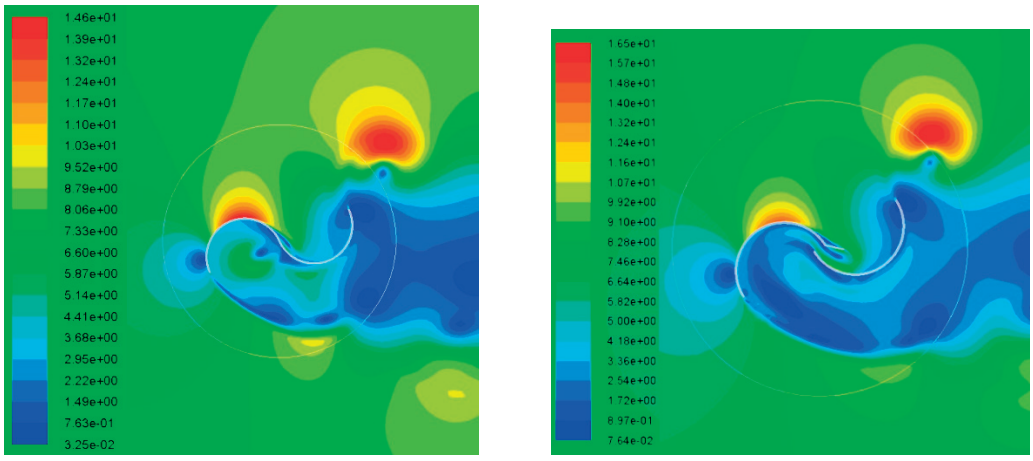

(a) (b)

Figure A5.9. Contour of the flow velocity around conventional rotor (a) and modified rotor (b) at rotor angle 240°.

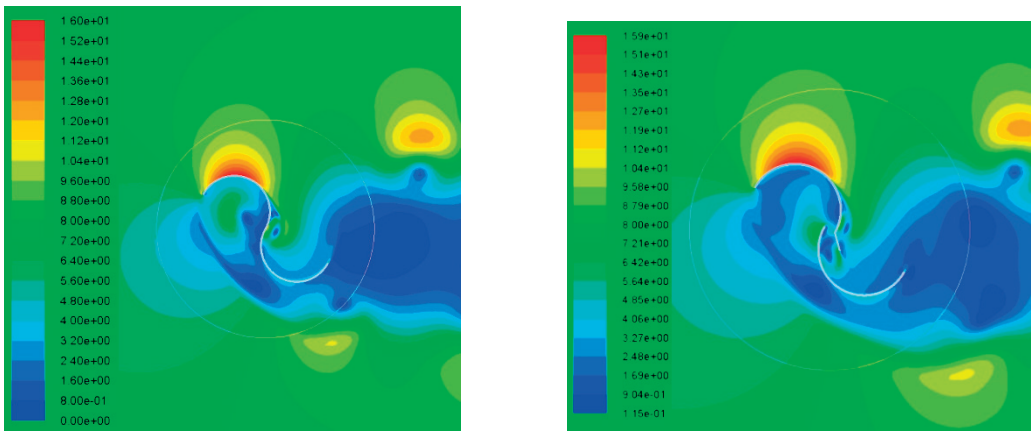

(a) (b)

Figure A5.10. Contour of the flow velocity around conventional rotor (a) and modified rotor (b) at rotor angle 300°.

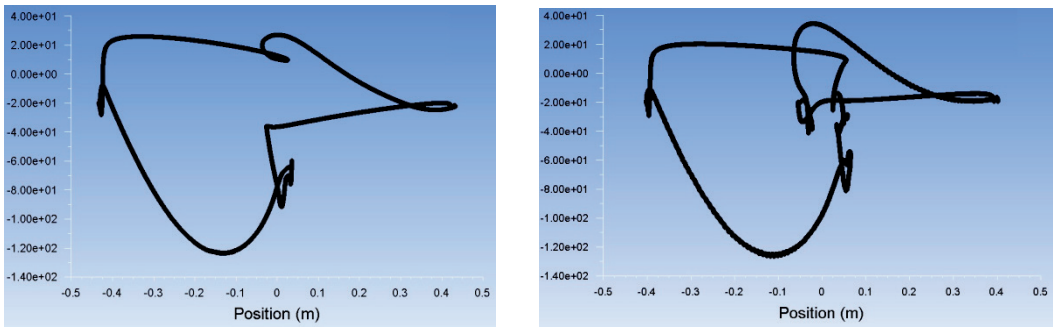

(a) (b)

Figure A5.11. Pressure distribution along the blade surfaces at rotor angle 300°: conventional rotor (a) and modified rotor (b).

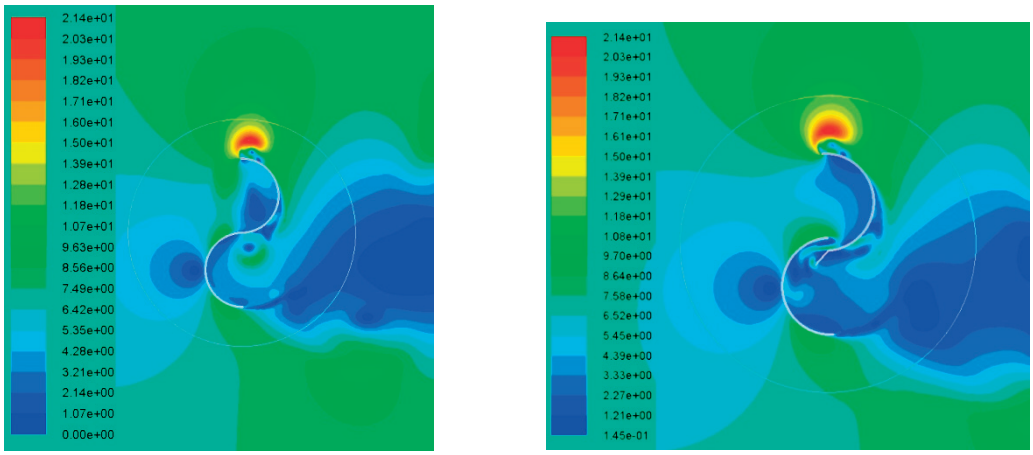

(a) (b)

Figure A5.12. Contour of the flow velocity around conventional rotor (a) and modified rotor (b) at rotor angle 360°.

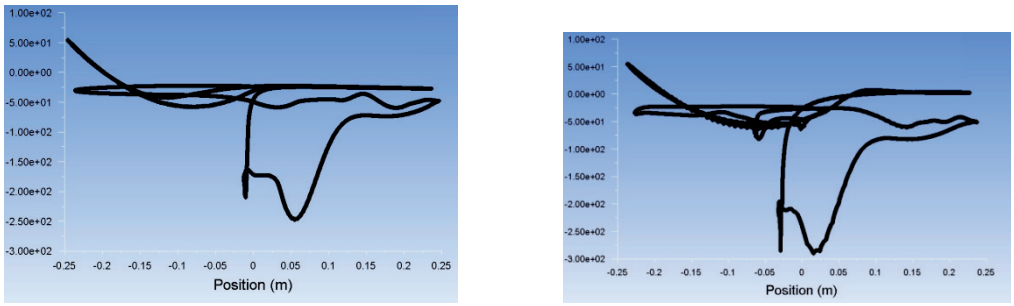

(a) (b)

Figure A5.13. Pressure distribution along the blade surfaces at rotor angle 360°: conventional rotor (a) and modified rotor (b).